

# **Flow of healthy and sickle red blood cells in microcirculatory conditions: clustering process and self-margination phenomenon**

**Dissertation**

**im Rahmen eines Cotutelle-Verfahrens zur Erlangung des Grades  
des Doktors der Naturwissenschaften  
der Naturwissenschaftlich-Technischen Fakultät  
der Universität des Saarlandes**

**Thèse**

**dans le cadre d'une cotutelle pour obtenir le grade de  
Docteur de l'Université de Montpellier  
Spécialité: Physique**

**von/présentée par**

**Viviana Andrea Clavería Pizarro**

**Saarbrücken/Montpellier**

**2017**

Tag des Kolloquiums: 26.06.2017

Dekan: Prof. Dr. Guido Kickelbick

Mitglieder des Prüfungsausschusses:

Vorsitzender: Prof. Dr. Albrecht Ott

Berichterstatter: Prof. Dr. Christian Wagner

Berichterstatter: Prof. Dr. Thomas Franke

Akademischer Mitarbeiter: Dr. Andreas Tschöpe

Weiteres Mitglied: Dr. Manouk Abkarian

Weiteres Mitglied: Dr. Simon Mendez

Weiteres Mitglied: Dr. Franck Nicoud

Weiteres Mitglied: Dr. Giovanna Tomaiuolo

# EIDESSTATTLICHE VERSICHERUNG

Hiermit versichere ich an Eides statt, dass ich die vorliegende Arbeit selbstständig und ohne Benutzung anderer als der angegebenen Hilfsmittel angefertigt habe. Die aus anderen Quellen direkt oder indirekt übernommenen Daten und Konzepte sind unter Angabe der Quelle gekennzeichnet. Die Arbeit wurde bisher weder im In- noch im Ausland in gleicher oder ähnlicher Form in einem Verfahren zur Erlangung eines akademischen Grades vorgelegt.

Saarbrücken, den 18.04.2017

Viviana Clavería Pizarro



## ACKNOWLEDGEMENT

First, I would like to express my utmost gratitude to my both supervisors Dr. Christian Wagner and Dr. Manouk Abkarian for the professional and personal guidance, support, comprehension and advices along the way. They have been the core and an essential support on the development of all this research and also, in my own personal development. There is not words to express how much I appreciate all what I have learnt from you.

I would also like to deeply thank Prof. Philippe Connes with whom we collaborate and who provided us with the sickle samples, and was always available for very nice scientific discussions. With him we highly enjoyed to perform new experiments and carry out interesting projects together. Your high and contagious enthusiasm makes the development of our collaboration full of nice moments. I would also like to thanks Céline Renoux and Dr. Philippe Joly from the Hospital GH Edouard Herriot in Lyon for their kindness and availability in the needed moments.

Thanks to the group in the Université Joseph Fourier, Grenoble and specially to Dr. Gwennou Coupier for the very nice scientific discussions, feedbacks and comments on the first part of the project developed in Saarbrücken. His scientific support enriched my research with new perspectives.

I would also like to deeply thank Dr. Stephan Gekle for his invitation to the University of Bayreuth and to start a nice collaboration with us, and as well to Achim Guckenberger who performed and is performing all the simulations for the phase diagram project. Also thanks very much for the nice shared moments. Special thanks to Alexander Kihm to continue working on this project.

My gratitude to whom received me and made me feel part of the Lab and Saarbrücken: Matthias Brust. I will never forget your help, nice lunches, Friday dinners and your family. I'm very happy to continue being your friend! Thanks Othmane Aouane for the nice 2D simulations. Also, I would like to thank you for picking me up my first day in Germany (of course a rainy day) and let the opportunity to build a nice friendship among us around nice coffee cups. Thanks to Daniel Flormann for his help on the pictures on this Thesis, for helping me with measurements on the Rheometer, the nice scientific discussions and as well for his release of energy that push me to give more of myself and inspire my way. Thanks to Christian Ruloff for his always nice disposition and fundamental help in the Lab and ideas/supporting to improve my experimental setup and data analysis. Thank you as well to teach me how to use, calibrate and align the Optical Tweezers of our Lab. Thanks to Thomas John for his help in coding and nice disposition for discussion in the moments I needed it. I also would like to thank my colleagues and friends along the way with whom I shared more than one nice scientific and/or personal conversation or with whom I share just and simply a very

nice relaxing moment: Javad Najafi, Daiki Matsunaga, Revaz Chachanidze, Zakaria Boujja, Greta Simionato, Alexander Kihm, Asena Abay, Lee Kisung, François Yaya, Andreas Schneider, Levke Ort, Sebastian Himbert, Andreas Christ, Emmanuel Terriac, Luiza Stankevics, Ettore Bernardi, Selda Sonusen and many others. Thanks as well to Franziska Lautenschläger for her help when I needed it as well as Lars Kästner, Jean Baptiste Fleury and Laura Hertz.

Thanks very much to Elke Huschens and Karin Kretsch for all the fundamental administrative and technical support.

In France, it is a must for me to thank Luca Lanotte. Our conversations and scientific discussions made the time in Montpellier full of great moments and new knowledge. Moreover, his supporting was fundamental to overcome critical stages during the development of my PhD and this Thesis writing. Thanks to be always there. Loïc Dumas and Magalie Manaargadoo-Catin: thanks for your patience and nice mood during the lab shearing. Special thanks to Loïc who shared with me more than one protocol for the experiments that I performed. Thanks to the people at the CBS who were always organizing nice events and made the environment serious and friendly at the same time.

Thanks to Geneviève Carriere and Bernadette Lacan for all the fundamental administrative support in France.

I also would like to thank to Dr. Simon Mendez for nice simulations in the project that we started to work and the nice shared moments. Thanks to Jean-Marc Fromental for his technical support and help in the use of the Rheometer at the UM and Dr. Christophe Blanc for his help, supporting and nice disposition on the management of the PolScope in the same institution.

Special and additional thanks to Daniel Flormann, Andreas Christ, François Yaya, Luca Lanotte and Revaz Chachanidze for help me with the french and german translations of the abstract, introduction and summaries of this Thesis.

Samuel Gutiérrez, Sebastian Órdenes, Shu Huin, Andrés Varas, Cristian Soto, Denisse Quinteros, Cristian Ayala, María Ignacia Fierro, Yahaira Arana, Tania Silva, Ximena Pizarro, Jessica Pizarro, Álvaro Clavería, Tomás Muñoz, Felipe Gatica, Camila Canto, Daniel Clavería, Guillermo Guerra, Javiera Cuenca, Gonzalo Uson, Salvador Tamayo: millones de gracias por la ayuda con la detección de glóbulos rojos! La presencia y ayuda chilena durante mi período de tesis me infló el corazón infinitamente.

Thank to my family: mother, father and sisters who contributed all the time to keep me going. Special thanks to my mother and father whom with their love, built and build everyday a new strand in my heart making it warmer and stronger. I love you very much!

Camila Canto and Killén Clavería: thanks to both of you to make the time in France affordable, funny, familiar and interesting for Ayeray and for me. You, dear cousins, will be always in our memories. I also dedicate special thanks to Catalina Uson and Pablo Ortega, whom with effort and good heart, went to France to be with our lovely Ayeray. Thanks as well to Margarita Vergara and Gonzalo Uson S. to be always present and support us as a family.

Special thank goes to my husband and daughter for the unconditional support, love and understanding. We almost started here to be a family and I can't express how proud I am of you Gonzalo to have been strong, keep me going, succeed in your own projects and cook so well. You are not only a wonderful partner, but also a great father. And her, my friendly Ayeray, she has been a smart and funny partner in all the way. Thanks for existing darling!

Finally, I acknowledge the support of the German Science Foundation research initiative SFB1027, the support of the Region Languedoc-Roussillon, the labex NUMEV (convention ANR-10-LABX-20) and the Franco-German University for the opportunity to be part of the cotutelle program between Saarland University and the University of Montpellier.



---

## ABSTRACT ( ENGLISH )

I experimentally characterized the clustering formation of healthy and sickle red blood cells (RBCs) flowing through straight micro-capillaries. The effect of aggregation was also investigated. I found that cluster formation under physiological conditions is most likely caused by a combination of hydrodynamic and macromolecule-induced interactions. Macromolecule-induced interactions are not fully overcome by shear stresses within the physiological range, and they contribute to cluster stability. Moreover, I found that a pronounced bimodal distribution of the cell-to-cell distances in the hydrodynamic clusters is produced.

Additionally, I investigated experimentally the collective behavior of oxygenated sickle RBCs and their distribution along cylindrical micro-capillaries with diameters comparable to a human venule or arteriole. I have shown that there is a heterogeneous distribution of RBCs according to their density: low-density cells tend to stay closer to the center of the channel, while most dense cells (also more rigid) self-margined under defined conditions. Aggregation seems to inhibit self-margination depending on the aggregative factor and patient: dextran allows self-margination in some patients and inhibits it in others. Plasma inhibits self-margination of cells in all cases, highlighting the importance of the plasma proteins and adhesive molecules in the aggregation phenomena.

## RÉSUMÉ ( FRANÇAIS )

J'ai caractérisé expérimentalement la formation de clusters au cours du passage de globules rouges (GRs) sains et drépanocytaires dans microcapillaires droites. L'effet de l'agrégation a été également étudié. J'ai montré que la formation des clusters dans des conditions physiologiques est due à la combinaison des interactions hydrodynamiques et des celles causées par les macromolécules du plasma. En effet, les interactions macromoléculaires ne sont pas complètement atténuées sous contraintes de cisaillement physiologiques et au contraire ils contribuent à la stabilité des clusters. En outre, j'ai découvert la présence d'une distribution bimodale en ce qui concerne les distances entre les cellules constituant les clusters hydrodynamiques.

En plus, j'ai étudié expérimentalement le comportement collectif des globules rouges drépanocytaires oxygénés et leur distribution radiale le long de microcapillaires cylindriques avec un diamètre comparable à ces des veinules et des artérioles humaines. J'ai trouvé que les GRs montrent une distribution hétérogène en fonction de leur densité: les cellules plus légères ont tendance à rester près du centre du canal, alors que la plupart des cellules denses (et aussi plus rigides) auto-marginent sous des conditions définies.

L'agrégation semble d'inhiber l'auto-margination en fonction des patients et en particuliers des facteurs d'agrégation: le dextrane, par exemple, favorise l'auto-margination dans certains patients et il la diminue dans des autres. Le plasma montre de contraster l'auto-margination des GRs dans tous les sujets, en soulignant l'importance des protéines et des molécules adhésives du plasma dans les phénomènes d'agrégation. Finalement, j'ai observé que l'auto-margination se manifeste naturellement au cours de l'écoulement de globules rouges drépanocytaires.

## KURZZUSAMMENFASSUNG (DEUTSCH)

Ich habe experimentell das Aggregationsverhalten gesunder und sichelförmiger roter Blutzellen während des Flusses durch Mikrokapillaren charakterisiert. Der Aggregationseffekt wurde ebenfalls untersucht. Ich habe festgestellt, dass die Aggregation unter physiologischen Bedingungen sehr wahrscheinlich durch eine Kombination aus hydrodynamischen und durch Makromoleküle induzierten Interaktionen verursacht wird. Letztere werden in physiologischen Bereichen nicht vollständig durch Scherspannungen beeinflusst überwunden und tragen zur Stabilisierung von Aggregaten bei. Außerdem habe ich gezeigt, dass der Zell-Zell Abstand in hydrodynamischen Aggregaten ausgeprägt bimodal verteilt ist.

Zusätzlich habe ich das kollektive Verhalten von sauerstoffreichen sichelförmigen roten Blutzellen und deren Verteilung in zylindrischen Mikrokapillaren mit Durchmessern, die denen von humanen Venulen oder Arteriolen entsprechen, experimentell untersucht. Ich habe gezeigt, dass rote Blutkörperchen abhängig von ihrer Dichte, heterogen verteilt sind: Zellen geringerer Dichte neigen dazu sich näher an der Mitte des Kanals zu befinden, während die meisten Zellen größerer Dichte (die auch höhere Steifigkeit haben) unter definierten Bedingungen zur Kanalwand migrieren. Aggregation scheint Selbst-Margination abhängig vom Aggregationsfaktor und Patienten zu hemmen: Dextran führt bei einigen Patienten zur Selbst-Margination, während es diese bei anderen hemmt. Plasma hemmt die Selbst-Margination in allen Experimenten, was die Bedeutung der Plasmaproteine und Plasmaklebemoleküle für Aggregationsphänomene verdeutlicht.

# Contents

<b>List of Figures</b>	<b>13</b>
<b>List of Tables</b>	<b>19</b>
<b>1 Introduction</b>	<b>1</b>
<b>2 Background</b>	<b>7</b>
2.1 Circulatory system . . . . .	7
2.2 What is blood? . . . . .	8
2.3 Red blood cells . . . . .	9
2.4 Red blood cell aggregation . . . . .	13
2.5 Blood flow in microcirculation . . . . .	16
2.5.1 Boundary integral method . . . . .	17
2.5.2 Margination . . . . .	18
2.5.3 RBC shape in confined flow . . . . .	20
2.5.4 Clustering of red blood cells . . . . .	21
2.6 Sickle cell anemia . . . . .	22
2.6.1 Overview . . . . .	22
2.6.2 Vaso-occlusion . . . . .	28
<b>3 General materials and methods</b>	<b>33</b>
3.1 RBC and microfluidics preparation . . . . .	33
3.1.1 Blood separation and suspending media . . . . .	33
3.1.2 Percoll continuous density separation . . . . .	34
3.1.3 PKH 26 and 67 . . . . .	35
3.1.4 PDMS chips . . . . .	36
3.1.5 Glass capillaries . . . . .	37
3.2 Main devices . . . . .	38
3.3 Stop flow technique . . . . .	39
3.4 Image analysis . . . . .	40
3.4.1 Clustering of red blood cells . . . . .	40
3.4.2 Self-margination in sickle cell anemia . . . . .	43
<b>4 Cluster of cells in microcapillary flow</b>	<b>49</b>
4.1 Introduction . . . . .	49
4.2 Materials and experimental methods . . . . .	49

4.3	Results and discussions . . . . .	52
4.3.1	Healthy red blood cells . . . . .	52
4.3.2	Numerical simulations . . . . .	63
4.3.3	Sickle red blood cells . . . . .	65
4.3.4	Materials and experimental methods . . . . .	65
4.3.5	Results and discussions . . . . .	65
4.4	Conclusion . . . . .	72
<b>5</b>	<b>Self-margination of sickle cells</b>	<b>75</b>
5.1	Introduction . . . . .	75
5.1.1	Aggregation and Self-margination in sickle cell anemia . . . . .	75
5.1.2	Cell-free layer, CFL . . . . .	76
5.2	Materials and experimental methods . . . . .	76
5.3	Results and discussions . . . . .	77
5.3.1	Patients blood's composition . . . . .	77
5.3.2	Solutions . . . . .	77
5.3.3	Hematocrit . . . . .	78
5.3.4	Velocity profile and CFL . . . . .	78
5.3.5	Bands distribution . . . . .	84
5.4	Conclusion . . . . .	93
<b>6</b>	<b>General conclusion</b>	<b>101</b>
<b>7</b>	<b>List of publications</b>	<b>107</b>
	<b>Bibliography</b>	<b>109</b>

# List of Figures

1	Sketch of the cardiovascular system. The different vessels types are shown	8
2	Main blood components are represented flowing through a blood vessel: red blood cells, white cells, platelets and plasma proteins [1]. . . . .	9
3	Typical shapes of human RBCs: (a) discocyte, (b) stomatocyte and (c) echinocyte [1]. . . . .	10
4	Representation of a hemoglobin protein and the arrangement of its two $\alpha$ chains, two $\beta$ chains and four Heme groups. . . . .	11
5	Schematic drawing of RBC's lipid bilayer membrane, its components and the spectrin network/cytoskeleton attached to it intracellular face [1]. .	11
6	Scheme of four modes of deformation of a RBC's bilipid membrane. . .	12
7	a) and b) are fluorescence images of the cell membrane taken under a confocal microscope and c) bright field image. a) shows RBCs in buffer solution, b) rouleaux of RBCs in 8 mg/ml of fibrinogen and c) rouleaux of cells suspended in 20 mg/ml of dextran 70 kDa. Image modified with permission from [1]. . . . .	14
8	(a) Depletion of large spheres induced by surrounding smaller spheres. The depletion layer is shown in blue and the forbidden area in black. (b) Depletion of RBCs due to surrounding macromolecules [1]. . . . .	14
9	Bridging theory where (a) specific binding and (b) unspecific binding of macromolecules between two RBCs are formed [1]. . . . .	15
10	Different stages of the bridging-depletion proposal on (a) RBCs. In (b) is shown macromolecules adsorbed by RBCs and thus, inducing aggregation. Increasing the concentration of macromolecules should decrease the interaction energy between cells due to bridging until the cells do not attract anymore as is shown in (c) and then, start to induce aggregation due to depletion (d) [1]. . . . .	16
11	Representation of the CFL and margination of a) white cells and b) platelets due to migration of red blood cells to the center of blood vessels.	18
12	2D images of the typical RBC shapes observed flowing through micro-capillaries: parachute (left) and slipper (right). . . . .	20
13	Sequence of images of a reconstructed 3D slipper-like a) and crois-sant b) RBCs flowing through a high confined microchannel. The 3D reconstructions were made by A. Christ from AG Wagner. . . . .	21
14	Snapshot of the typical RBC cluster configurations of type $n$ , which contain $n$ cells for an imposed $\Delta P = 100$ mbar [2]. . . . .	22

15	Sequence of images of a reconstructed 3D cluster formed by 2 RBCs flowing through a high confined microchannel. The 3D reconstructions were made by A. Christ from AG Wagner. . . . .	22
16	Hemoglobin types before and after birth. Types of cells and organs in which the gene is expressed is shown [3]. . . . .	23
17	a) Sketch of free HbS inside a sRBCs forming rope-like fibers of about 21 nm in diameter [4]. The rope-like fibers can be noticed in the zoomed image of the upper panel in b), of a deoxygenated sRBCs presented in the panel at the bottom. Images in b) were taken using a scanning electron microscope (SEM) by G. Simionato from AG Wagner. . . . .	24
18	Images of oxygenated sRBCs a) of a patient submitted to a deoxygenation (up to 1% of oxygen partial pressure) b) and reoxygenation c). The reversibility of the HbS polymerization can be noticed from the sequence of images from a) to c). However, in a) and c) some irreversible sRBCs are present (elongated and far from discocyte shapes). The images were taken using a scanning electron microscope (SEM) by G. Simionato from AG Wagner. . . . .	24
19	Shear modulus $G_S$ (here named $\mu$ ) normalized by the healthy shear modulus of $0.32 \text{ g/cm}^3$ as a function of the intracellular concentration of hemoglobin MCHC. Empty circles are the values of healthy cells while triangles are the measured values of oxygenated sRBC [5]. . . . .	25
20	Scenario of the chain of events leading to VO. (1) Free HbS triggers an inflammatory response in the blood vessels. (2) The inflammatory response leads to leukocyte and platelet recruitment on endothelial cells. (3) free HbS molecules can bind to nitric oxide (NO) in the plasma, reducing its bioavailability and producing oxydative damage. (4) HbS-NO binding results in an imbalance of vasoconstrictor proteins leading a strong vasoconstriction event (5) producing VO. . . . .	30
21	Scenario of VO: (1) increased recruitment of white blood cells due to infections and/or pro-inflammatory state and their (2) interaction with sRBCs increasing its transient time, leading to hypoxia and sRBC sickling. . . . .	31
22	Sketch of blood separated in different components after centrifugation. From top to bottom: plasma, buffy coat, and the RBCs pellet [1]. . . . .	34
23	left: 2 ml of 50% of hematocrit in PBS deposited at the very top of the percoll layers of different densities (separated by dashed lines). Right: falcon after centrifugation with different well defined bands of cells located in between the layers of different densities. . . . .	35
24	Relative fluorescence intensity curves of PKH26 a) and 67 b) fluorescence cell linkers are presented. The maximum and the minimum wavelenght of excitation and emission and their values are specified by a line on the curves. . . . .	36
25	Sketch and photograph of the PDMS-based microfluidic device. . . . .	37

26	Left: sketch of the glass capillaries dimensions and right, photograph of a glass capillaries-based microfluidic chip. . . . .	38
27	Experimental setup for the flow stop technique. . . . .	39
28	In the image is shown how the upper border of the channel is manually marked. . . . .	40
29	Sustracting background of each image. . . . .	40
30	Image showing the number of cells inside each object estimated automatically by the program. At the same time, the program is asking for a manual correction of the number of cells estimated. . . . .	41
31	From left to right: length $D$ of a cell, distance $d$ between two consecutive cells, cluster length $L$ and surface-to-surface intercellular distance $I$ over the axial line of consecutive cells belonging to the same cluster. . . . .	42
32	The spanwise position of a cell $d_C$ is sketched. $d_C = \frac{w}{2} - \frac{h}{2}$ , where $w$ is the width of the channel and $h$ is the hight of the cell. . . . .	42
33	Representative images of adhering and hydrodynamic clusters are presented.	43
34	Representative images of doublet-shape classification. . . . .	43
35	Example of a sequence of images of the same cell. First row (from top to bottom) are images of the focus and defocus of the cell while moving back and forward on a sequence of images. The image nr. 5 is the "in focus" image of the cell. In the second row is shown the location of the cell position (yellow dot), located at the center of the cell. . . . .	44
36	The first column show the images of a channel and the second column sketch the cylindrical section of it. The longitudinal middle-plane of the channel is shown in a), and the channel bottom in b). The $(h,y)$ and radial position $r$ of the cells are shown in c). . . . .	45
37	Transversal projection of the position of the $n_L$ cells detected in the channel (red dots). The cell-free layer (CFL) position (limit of the core where the cells flow) is located at $R - \delta$ , where $R$ is the tube radius and $\delta$ the CFL thickness. . . . .	46
38	The standard deviation of the row intensity values in b) are obtained from the histogram of the row intensity values in a). Distances from the channel borders and peaks of the standard deviation were considered as a value of the CFL for a given experimental conditions. . . . .	46
39	Example of the velocity profile obtained by PIV over two consecutive images. Black arrows represent the direction and magnitud of the velocity.	47
40	Parabolic approximation (red continuous line) of the instantaneous velocity profiles obtained from Fig.39. As reference, dash lines have been plot: red indicates the value of the maximum velocity and purple the position of the CFL. . . . .	47
41	Semi-annulus area $A$ of the transversal cross section of the channel. . .	48

42	Experimental setup. Images of the flowing cells are taken using a 60x, NA = 1.4 oil immersion objective. a) With the help of a motorized x–y stage, different positions are observed along the microchannels (see Fig.43 for details). A high-precision pressure device is connected to an external 1.5 ml reservoir that contained the sample. b) Through a polyethylene tube, the external reservoir is connected to the internal reservoir of the microfluidic device to inject the cells into the channels at different pressure drops. c) An image of the field of view of the microchannels on the computer is presented. . . . .	50
43	Four different positions were observed along the channels with the help of a motorized x–y stage (see Fig.42). Each position cover a field of view of 0.25 mm in width and is located at 0 mm, 1 mm, 2 mm, and 10 mm from the entrance of the channels that are called Positions 0, 1, 2 and 10, respectively. . . . .	51
44	Snapshot of the typical RBC cluster configurations of type $n$ , which contain $n$ cells for an imposed $\Delta P = 100$ mbar [2]. . . . .	53
45	Probability density of the cell center to channel axis distance for $\Delta P = 20, 50, 100$ and $1000$ mbar in BS. . . . .	54
46	Cumulative occurrence probability of different cluster types $n$ per solution at four different distances from the entrance along the channel for $\Delta P = 50, 100$ and $1000$ mbar. Type 1 indicates single cells. . . . .	55
47	( $\Delta P = 100$ mbar) a) Median value $\tilde{l}$ of the cluster length $L$ distribution by cluster type $n$ . The error bars are the positions of the first and third quartil. b) Median value of the surface-to-surface intercellular distance $I$ over the axial line per cluster type $n$ . The error bars represent the positions of the first and third quartil. Straight lines indicate linear fits. . . . .	57
48	Percentage of the hydrodynamic and adhering cluster type $n = 2$ occurrence per cluster length in BS+Dex70 (left) and BS+Dex150 (right) solutions flowing at a pressure drop of $\Delta P = 100$ mbar. . . . .	59
49	Photographs of the typical cluster configuration as a function of the pressure drop and solution for the median value $\tilde{l}$ of the cluster type $n = 2$ length distribution presented in table 9. . . . .	59
50	Probability density of the characteristic cluster length $L$ of the cluster type $n = 2$ for BS, BS+Dex70 and BS+Dex150 solutions. The photographs are representative snapshots of the most frequent cluster configurations with the cluster length position indicated by the arrows between the photographs and the graph lines. . . . .	61
51	Probability density of the cluster length distributions for the pure hydrodynamic clusters type $n = 2$ in the macromolecule solutions BS+Dex70 (left) and BS+Dex150 (right). . . . .	62
52	Percentage of the different shapes of clusters of type $n = 2$ (see Fig.49) per cluster length (BS solution). . . . .	63
53	Numerically obtained stationary shapes of cluster type $n = 2$ at different maximum centerline flow velocities for different solutions. . . . .	64

54	Probability density of the cell-center to channel-axis distance for $\Delta P = 50, 100, \text{ and } 1000 \text{ mbar}$ in BS (first row) and BS+Dex70 (second row).	66
55	Comparison of the cumulative occurrence probability between healthy RBCs (Healthy) and sRBCs (Sickle) of different cluster types $n$ in BS solution (top) at four different distances from the entrance along the channel for $\Delta P = 50, 100 \text{ and } 1000 \text{ mbar}$ and BS+Dex70 solution (bottom). Type 1 indicates single cells. . . . .	68
56	Eccentricity of a population of healthy RBCs compared to the eccentricity of a population of oxygenated sRBCs. Representative images of cells are presented. A higher heterogeneity is observed for sRBCs, where the presence of irreversible sRBC cells as well as constant sickling, deviate the shape from the discocyte shape observed for healthy RBCs. . . . .	69
57	Probability density of the characteristic cluster length $L$ of the cluster type $n = 2$ for BS (left) and BS+Dex70 (right) solutions for the three different pressure drop $\Delta P = 50, 100 \text{ and } 1000 \text{ mbar}$ . . . . .	70
58	Example images of clusters type $n = 2$ with a cluster length, $L$ , around $4.5 \mu\text{m}$ . . . . .	70
59	Percentage of the different shapes of clusters of type $n = 2$ per cluster length at 50, 100 and 1000 mbar in BS solution from left to right. . . . .	71
60	Example images of clusters type $n = 2$ classified as others. . . . .	71
61	Plot of the band volume fraction of each sRBC band. Patients 1 and 2 show a bimodal distribution of bands. Patient 3 has an additional increment of band III while Patient 4 has a high population of reticulocytes and band III, and low population of band II and IV, contrary to all the rest of the patients. . . . .	78
62	Representative images of sRBCs flowing at different pressure drops in BS. It is possible to notice the increasing of the CFL thickness when pressure drop increases. . . . .	79
63	Velocity profile of low (black straight line) and high (red straight line) $H_t$ for BS at different pressure drops. The error zone is given by the standard deviation of the fitting from all data. Light blue dash line is the Poiseuille velocity profile of a Newtonian fluid with the same viscosity than the suspending media. . . . .	80
64	CFL thickness, $\delta$ , versus mean shear rate, $\bar{\gamma}$ , for BS, BS+Dex70 and Plasma solutions. . . . .	82
65	Distribution of cells belonging to the a) band II and b) band IV flowing in BS at low $H_t$ for each pressure drop. . . . .	84
66	Distribution of cells belonging to the a) band II and b) band IV flowing in BS at low $H_t$ is presented for each pressure drop for patient 1. . . . .	86
67	Average cell distribution over all pressure drops of band II and IV flowing in BS at low $H_t$ for patient 1. . . . .	86
68	Distribution of cells belonging to the a) band II and b) band IV flowing in BS at high $H_t$ is presented for each pressure drop for patient 1. . . . .	87

69	Average cell distribution over all pressure drops of band II and IV flowing in BS at high $H_t$ for patient 1. . . . .	87
70	Average cell distribution over all pressure drops of band II and IV flowing in BS at low (first row) high (second row) $H_t$ for patient 2, 3 and 4. . .	88
71	Average cell distribution of band II and IV of cells flowing in BS over all pressure drops at low and high $H_t$ . Results per patient is presented. . .	89
72	Distribution of cells per pressure drop of band II and IV of patient 1 flowing in BS+Dex70 solution. Results for low (left column) and high (right column) $H_t$ are presented. . . . .	90
73	Comparison of the average distribution curves of band II and IV between BS and BS+Dex70 solutions for patients 1, 2 and 3 from top to bottom. Results for low (left column) and high (right column) $H_t$ are presented.	91
74	Distribution of cells per pressure drop of band II and IV of patient 1 flowing in autologous Plasma. Results for low (left column) and high (right column) $H_t$ are presented. . . . .	92
75	Comparison of the average distribution curves of band II and IV between BS and Plasma solutions for patients 1 and 2 (top to bottom). Results for low (left column) and high (right column) $H_t$ are presented. . . . .	93

# List of Tables

1	Vessel types and their diameter, mean flow velocity and wall shear rate [6].	8
2	Typical elastic moduli values of RBC's membrane [7]. . . . .	13
3	Values of the elongation index (EI) and mean corpuscular hemoglobin concentration (MCHC) for healthy RBCs (AA) and sRBCs in SCA. $n$ indicates the number of donors for each case [8]. . . . .	26
4	Potential mechanisms in sRBC adhesion to endothelium [9]. Sulfated glycolipids are exposed in the sRBCs membrane. Adhesive molecules on sRBCs can be activated by stress on the surface of the reticulocytes (CD36, $\alpha_V\beta_3$ ) or on sRBC membrane by signal transduction (IAP and ICAM-4). Some of the molecules need adhesive bridging proteins to bind into the endothelial receptors while others can bind directly to the endothelial receptors. . . . .	27
5	Values of the aggregation half time $t_{1/2}$ , minimum shear rate $\gamma_{min}$ to disperse preformed sRBC aggregates, and fibrinogen concentration for healthy RBCs (AA) and sRBCs in SCA. $n$ indicates the number of donors for each case [8]. . . . .	28
6	Maximum flow velocity per solution calculated from Eq.(12) for the pressure drops used in this experiment in our rectangular cross-sectional channels. . . . .	51
7	Average RBCs velocity per pressure drop and suspending media obtained by image analysis for each solution. . . . .	52
8	Capillary number $Ca_S$ and $Ca_B$ for each pressure drop and solution. . .	53
9	Median value $\tilde{l}$ of the cluster type $n = 2, 3$ and $4$ length distribution for each pressure drop per solution. $q_i^-$ and $q_i^+$ are the first and 3rd quartil of the length distribution per cluster type. . . . .	58
10	Characteristic lengths of the hydrodynamic cluster type $n = 2$ . The length distributions are fitted with a double-peak function composed of two bi-gaussian distribution of center $L_i$ , and left and right standard deviation $w_i^-$ and $w_i^+$ . . . . .	62
11	Average sRBCs velocity per pressure drop and suspending media obtained by image analysis for each solution. . . . .	65
12	Band volume fraction of each sRBC band, and HbS and HbF content of each patient is presented. . . . .	77
13	Summary of the suspending media used for the experiments for each patient. . . . .	78

---

14	Average hematocrit per patient obtained by suspending media. Low $H_t$ values are presented at the top, and high $H_t$ values are presented at the bottom of the table. . . . .	79
15	From left to right: tube hematocrit, $H_t$ , pressure drop, $\Delta P$ , mean shear rate, $\bar{\gamma}$ , maximum center-line velocity of the cell core, $v_{max}$ , and the maximum center-line velocity of the newtonian fluid, $v_N$ , whose viscosity is the one of the suspending media. The values were averaged over all patient for each solution. . . . .	81
16	$a$ and $b$ of the fitting $\delta = a\bar{\gamma}^b$ on the CFL thickness data points in Fig.64.	82

# 1

## Introduction

### Introduction (english)

Within small blood vessels, called capillaries, the higher exchange of substances between the vessels and the tissue occurs. Capillaries are densely interconnected and together with arteriols and venules constitute most of the area of the circulatory system. This subsystem is called microcirculation.

Blood contains a high volume fraction of red blood cells that strongly influence its flow properties. Without any external stress, mature red blood cells (RBCs) normally take the shape of biconcave disk. Their interiors are filled with a concentrated hemoglobin solution, that is an incompressible viscous fluid. They are surrounded by a viscoelastic membrane consisting of a lipid bilayer, and a network of proteins, called cytoskeleton, attached to the inner side of their membrane. The diameter of a single cell at rest is bigger than some capillaries in the human body. Therefore, RBCs have to strongly deform to travel through them. Nonetheless, they flow through the capillaries easily as a result of their high deformability. A more complex scenario happens in the case of some diseases such sickle cell anemia (SCA), in which the deformability of the cells is lower than that of healthy cells.

SCA affects over 50 million people worldwide and has become one of the most common inherited disorders in European countries. It is a molecular disease caused by a mutation in the hemoglobin, leading to its polymerization under hypoxia (low level of oxygen), having harmful effects on the RBC membrane, shape, density and inner viscosity. In general terms, RBC deformability is reduced and hemolysis (destruction of the RBC that leads to the release of its contents) happens frequently. These facts lead to a vaso-occlusive events, anemia and general inflammatory state of the circulatory system.

Different and complex vaso-occlusive scenarios have been proposed, but no extensive description on the dynamics of such events are available. Additionally, no prognostic factors are currently available clinically and few pharmacological treatments exist. Therefore, there is clearly a need for better understanding of the disease pathophysiology to be able to screen the most at-risk population and to improve their clinical management. Nevertheless, it is known that vaso-occlusive events occur mainly in microcirculation and so, we put effort into investigating the behavior of sickle RBCs (sRBCs) *in vitro* flowing through channels mimicking microcirculatory conditions.

In the presence of some macromolecules like fibrinogen (naturally present in blood plasma), RBCs aggregate in a so-called rouleaux formation. Aggregation of RBCs is a reversible process and as a consequence blood behaves as a shear-thinning fluid decreasing its viscosity when shear rate increases (rheofluidification). The aggregates seem not to be relevant for the flow of cells at the capillary level where wall shear rate has higher values compared to the wall shear rate in bigger vessels. However, contrary to what had been thought previously, it has been shown that aggregates are robust structures in highly confined capillaries (tube diameter less than RBC diameter). In capillaries with slightly less confinement (allowing the cells to couple to the flow, but not to squeeze on the tubes), RBCs flow usually in single file and well-organized clusters tend to form. The physical origin of this cluster formation can be a long-ranged hydrodynamic interaction between the cells. But, can both hydrodynamic clusters and macromolecule-induced aggregates coexist when the cells flow through microcapillaries? Are both cases relevant? Is there any difference in case of the flow of sRBCs compared with the flow of healthy RBCs? This study looks into both mechanisms and concludes that both are relevant.

Another interesting but still not fully understood phenomenon in microcirculation is margination. Stiffer cells like white blood cells or platelets travel towards the vessel walls in blood flow through a process called margination. This is a consequence of the migration of the relatively more deformable RBCs to the center of vessels. Knowing that sRBCs have high rigidity variations in their population raises the question if the margination phenomenon affects the collective behavior of sRBCs (or, do sRBCs self-marginate)? Does aggregation have a role in this behavior?. In the second part of this thesis, it is shown that sRBCs self-marginate. However, this tendency depends on each patient, and on the presence and nature of aggregants in the suspending media. It has been addressed interesting aspects on sRBCs behavior in flow and has been shown that sRBCs, under defined conditions self-marginate.

In the second chapter of this thesis, and introduction to the microcirculatory system, blood flow and in particular the behavior of healthy and sRBCs under different conditions is presented. The third chapter is dedicated to the description of the materials and methods used to perform the experiments. In the fourth and the fifth chapters, the results of the clustering process on healthy RBCs and sRBCs, and the results of the self-margination of sRBCs are presented. Subsequently, the list of publications in scientific journals are summarized. Finally, the conclusion and perspectives are presented.

## **Introduction (français)**

L'échange de substances (surtout l'oxygène) entre le système vasculaire et les tissus a lieu essentiellement dans de petits vaisseaux, les capillaires. Les capillaires sont densément interconnectés et, avec les artérioles et les veinules, constituent en termes de surface, la majorité du système circulatoire. Ce sous-système est appelé la « microcircu-

lation ».

Le sang contient une fraction volumique de globules rouges très élevée, qui influence fortement ses propriétés sous écoulement. Quand aucune force externe est appliquée, les globules rouges (GRs) matures présentent une forme de disque biconcave. Ils sont entourés par une membrane viscoélastique constituée d'une bicouche lipidique et d'un réseau de protéines, le cytosquelette, attaché à sa surface interne. A l'intérieur de cette membrane est contenue une solution concentrée d'hémoglobine, le cytosol, qui a les caractéristiques d'un fluide visqueux incompressible. Le diamètre d'un GR au repos est plus grand que celui de nombreux capillaires dans le corps humain. Toutefois, les GRs doivent subir une importante déformation pour se déplacer à l'intérieur de ceux-ci. Le scénario devient plus complexe en cas de pathologies comme la drépanocytose (DR), à cause de laquelle la déformabilité des cellules est visiblement diminuée par rapport aux cellules saines.

La DR affecte plus de 50 millions de personnes dans le monde entier et elle est devenue une des maladies héréditaires les plus communes dans les pays européens. Il s'agit d'une pathologie moléculaire qui cause des mutations de l'hémoglobine. Les conséquences principales de cette altération sont la polymérisation de l'hémoglobine sous des conditions d'hypoxie (bas niveau d'oxygène), et des effets nuisibles sur la membrane, la densité, la viscosité interne et donc sur la forme des GRs. Globalement, en plus de la diminution de déformabilité déjà mentionnée, les cellules sont sujettes à de fréquentes hémolyses (destruction des GRs qui mène au rejet de ce qu'ils contiennent). Ces phénomènes conduisent à des événements d'occlusion vasculaire, et des états inflammatoires et anémiques du système circulatoire.

Des scénarii complexes et différents ont été proposés pour expliquer la vaso-occlusion mais une description approfondie des dynamiques qui caractérisent ces événements est encore manquante. En plus, actuellement, le pronostic des occlusions n'est pas possible cliniquement et très peu de traitements pharmacologiques existent. Par conséquent, il est absolument nécessaire de faire la lumière sur la pathophysiologie de la drépanocytose afin de protéger les populations les plus exposées et d'améliorer leur gestion clinique. Puisque les occlusions vasculaires se produisent surtout dans la microcirculation, notre objectif est d'investiguer *in vitro* le comportement des GRs drépanocytaires (GRDs) sous écoulement, dans des canaux mimant les conditions microvasculaires.

En présence de certaines macromolécules, comme par exemple le fibrinogène (présent dans le plasma sanguin en conditions physiologiques), les GRs ont tendance à s'agréger sous forme de rouleaux. L'agrégation des GRs est un phénomène réversible et par conséquent, le sang se fluidifie diminuant ainsi sa viscosité lorsque le taux de cisaillement croît (rhéofluidification). En conséquence, les agrégats de GRs ne semblent pas jouer un rôle dans l'écoulement des cellules au niveau capillaire, où les taux de cisaillement aux parois sont très élevés par rapport aux vaisseaux sanguins de plus grande taille. Cependant, contrairement à ce que nous pourrions penser, il a été montré que les

agrégats forment des structures robustes dans les capillaires très confinés (diamètre du tube inférieur à celui des globules). Dans des capillaires légèrement moins confinés, où les cellules épousent la forme de l'écoulement sans pour autant être complètement écrasées par les parois du tube, les GRs s'écoulent d'habitude en file unique et des « clusters » organisés se forment. L'explication physique à l'origine de la formation de ces « clusters » est possiblement l'interaction hydrodynamique à longue distance entre cellules. En revanche, est-ce que les « clusters hydrodynamiques » et les agrégats engendrés par les macromolécules peuvent coexister lors de l'écoulement dans les microcapillaires? Les deux cas de figure sont-ils pertinents? Ya-t-il une différence d'écoulement pour les GRDs en comparaison avec des GRs sains? Cette étude montre l'importance de ces deux mécanismes et vérifie que les deux sont pertinents.

Un autre phénomène important mais peu connu, en ce qui concerne la microcirculation, est la « margination ». Les cellules plus rigides, comme les globules blancs ou les plaquettes, se déplacent dans la direction des parois vasculaires, dans l'écoulement sanguin, par un processus appelé margination. La conséquence est que les GRs relativement plus déformables ont tendance à se concentrer dans le voisinage du centre du canal. Sachant que les GRDs ont des grandes variations de rigidité selon les populations, nous pouvons nous demander si le phénomène de margination affecte le comportement collectif des GRDs (ou si les GRD subissent une automargination). Quel rôle joue l'agrégation sur ce comportement? Dans la deuxième partie de la thèse, nous avons montré que les GRDs, sous certaines conditions, subissent une automargination. Toutefois, cette tendance varie en fonction des patients, de la nature et de la présence de facteurs d'agrégation dans le milieu de suspension.

Dans le deuxième chapitre de cette thèse, une introduction au système microcirculatoire, à l'écoulement du sang et notamment, au comportement de GRs sains et drépanocytaires sous différentes conditions est présentée. Le troisième chapitre est consacré à la description des matériels et méthodes utilisés pour les expériences. Dans les chapitres 4 et 5, les résultats obtenus sur le « clustering » de globules sains et de GRDs, ainsi que ceux concernant « l'automargination » des GRDs sont décrits. La liste des publications scientifiques est ensuite résumée. Enfin, la conclusion et les perspectives sont présentées.

## **Einführung (deutsch)**

Innerhalb kleiner Gefäße, genannt Kapillaren, tritt ein Austausch von Substanzen zwischen Gefäßen und Gewebe auf. Kapillaren sind dicht vernetzt und machen zusammen mit Arteriolen und Venolen den größten Teil der Oberfläche des Kreislaufsystems aus. Dieses Untersystem wird Mikrozirkulation genannt.

Blut enthält zu einen großen Volumenanteil rote Blutzellen, welche die Flusseigenschaften stark beeinflussen. Ohne externe Spannung nehmen voll entwickelte rote Blutzellen im Normalfall die Form einer bikonkaven Scheibe an. Deren Innenräume sind mit

einer konzentrierten Hämoglobinlösung, die eine incompressible viskose Flüssigkeit ist, gefüllt. Sie sind von einer viskoelastischen Membran, die aus einer Lipiddoppelschicht und einem Netzwerk von Proteinen, genannt Zytoskelett, das mit der Innenseite der Membran verbunden ist, umschlossen. Der Durchmesser einer einzelnen Zelle in Ruhe ist größer als einige Kapillaren im menschlichen Körper. Daher müssen sich RBCs stark deformieren, um diese passieren zu können. Nichtsdestotrotz fließen sie dank ihrer hohen Deformierbarkeit mit Leichtigkeit durch die Kapillaren. Ein komplexeres Szenario findet im Fall einiger Krankheiten, wie z.B. der Sichelzellenanämie (SZA), bei denen die Deformierbarkeit der Zellen geringer ist als die gesunder Zellen, statt.

SZA beeinflusst über 50 Millionen Menschen weltweit und ist eine der meist verbreiteten Erbkrankheiten in europäischen Ländern geworden. Es handelt sich um eine Krankheit, die durch eine Mutation im Hämoglobin verursacht wird, die zu einer Polymerisation unter hypoxischen (geringes Level an Sauerstoff) Bedingungen führt und eine schädliche Wirkung auf die Membran, die Form, die Dichte und die innere Viskosität von rote Blutzellen hat. Allgemein wird die Deformierbarkeit von rote Blutzellen reduziert und es kommt häufig zur Hämolyse (Zerstörung der rote Blutzelle, was zur Freisetzung der Inhalte führt). Die Umstände führen zu vaso-okklusiven Vorkommnissen, Anämie und generellen Entzündungszuständen des Kreislaufsystems.

Verschiedene und komplexe vaso-okklusive Szenarien wurden vorgeschlagen, aber keine umfangreiche Beschreibung der Dynamik solcher Vorkommnisse ist verfügbar. Zusätzlich sind zur Zeit keine Prognosefaktoren von klinischer Seite verfügbar und es existieren wenige pharmakologische Behandlungen. Daher besteht offensichtlich eine Notwendigkeit des besseren pathophysiologischen Verständnisses dieser Krankheit, um Hochrisikogruppen systematisch untersuchen zu können und um deren klinisches Management zu verbessern. Nichtsdestotrotz ist bekannt, dass vaso-okklusive Vorkommnisse hauptsächlich in der Mikrozirkulation auftreten. Daher unternahmen wir Bemühungen bezüglich der Untersuchung des Verhaltens von sichelförmigen rote Blutzellen *in vitro*, die durch Kanäle fließen und somit die mikrozirkulatorischen Bedingungen nachahmen.

In Anwesenheit mancher Makromoleküle, wie z.B. Fibrinogen (von Natur aus im Blutplasma vorkommend), aggregieren rote Blutzellen zu sogenannten Rouleaux-Formationen. Die Aggregation von rote Blutzellen ist ein reversibler Prozess, was zur Folge hat, dass sich Blut wie eine scherverdünnende Flüssigkeit verhält, d.h. die Viskosität sinkt mit steigender Scherrate. Aggregate scheinen für den Fluss von Zellen auf Kapillarniveau, bei dem die Wandscherrate höhere Werte im Vergleich zur Wandscherrate in größeren Gefäßen aufweist, nicht relevant zu sein. Allerdings wurde im Kontrast zu vorherigen Vermutungen gezeigt, dass Aggregate robuste Strukturen in sehr engen Kapillaren (Rohrdurchmesser geringer als Durchmesser einer rote Blutzelle) bilden. In wenig größeren Kapillaren (die Zellen können an den Fluss koppeln, aber drücken nicht gegen die Gefäßwände) fließen rote Blutzellen normalerweise in Reihen hintereinander her und tendieren zur Formierung klar geordneter Aggregate. Der physikalische Ursprung dieser Aggregate kann eine langreichweitige hydrodynamische Interaktion zwischen den Zellen

sein. Aber können sowohl hydrodynamische Aggregate als auch Makromolekül-induzierte Aggregate während dem Fluss der Zellen durch Mikrokapillaren koexistieren? Sind beide Fälle relevant? Gibt es einen Unterschied im Fall des Flusses von sichelförmigen rote Blutzellen verglichen mit dem Fluss gesunder rote Blutzellen? Diese Studie beschäftigt sich mit beiden Mechanismen und folgert, dass beide relevant sind.

Ein anderes interessantes, aber bisher noch nicht vollständig verstandenes, Phänomen in der Mikrozirkulation ist die Margination. Steifere Zellen, wie weiße Blutzellen oder Blutplättchen, tendieren im Blutfluss zu den Gefäßwänden zu migrieren, was Margination genannt wird. Hierbei handelt es sich um eine Konsequenz der Migration von vergleichsweise stärker deformierbaren rote Blutzellen zum Mittelpunkt der Gefäße. Basierend auf dem Fakt, dass Populationen von sichelförmigen rote Blutzellen große Variationen in ihrer Steifigkeit aufweisen, kann die Frage gestellt werden ob das Marginations-Phänomen das kollektive Verhalten von sichelförmigen rote Blutzellen beeinflusst (oder können sichelförmigen rote Blutzellen selbst-migrieren)? Spielt Aggregation für diesen Prozess eine Rolle? Im zweiten Teil dieser Arbeit wird gezeigt, dass sichelförmigen rote Blutzellen selbst-migrieren. Aber diese Tendenz hängt von jedem Patienten und der Anwesenheiten und Natur von Aggreganden in den suspendierenden Medien ab. Es wurde sich mit interessanten Aspekten des Fließverhaltens von sRBCs bewasst und es wurde gezeigt, dass sichelförmigen rote Blutzellen unter definierten Bedingungen selbst-migrieren.

Im zweiten Kapitel dieser Arbeit und in der Einführung des Mikrozirkulationssystems wird der Blutfluss und speziell das Verhalten gesunder und sichelförmigen rote Blutzellen unter verschiedenen Bedingungen präsentiert. Das dritte Kapitel widmet sich der Beschreibung der genutzten Materialien und Methoden, mit denen die Experimente durchgeführt wurden. Im vierten und fünften Kapitel werden die Resultate des Aggregationsprozesses bei gesunden rote Blutzellen und sichelförmigen rote Blutzellen sowie die Resultate der Selbst-Margination von sichelförmigen rote Blutzellen präsentiert. Im Anschluss wird die Liste der Publikationen in wissenschaftlichen Journalen zusammengefasst. Am Ende werden die Zusammenfassung und der Ausblick präsentiert.

# 2 Chapter 2

---

## Background

### Background (english)

This chapter is dedicated to introducing the microcirculatory system, blood flow and in particular the behavior of red blood cells. This information will be useful in understanding the scientific context of my experiments and the main results.

### Prérequis (français)

Ce chapitre comporte une introduction au système microcirculatoire, l'écoulement sanguin et en particulier, le comportement des globules rouges. Ces informations seront capitales dans la compréhension du contexte scientifique dans lequel mes expériences ont été réalisées et les principaux résultats.

### Hintergrund (deutsch)

Dieses Kapitel ist dem mikrozirkulatorischen System, dem Blutfluss und besonders dem Verhalten von roten Blutzellen gewidmet. Diese Informationen sind dem wissenschaftlichen Verständnis meiner Experimente und der wesentlichen Resultate zweckdienlich.

## 2.1 Circulatory system

In order to provide nutrients and oxygen to the cells in our body and to help them to remove gaseous wastes, fight against diseases, and stabilize their temperature and pH, different organs are connected through a network of vessels. Different components circulate in this network, constantly pumped by the heart through contraction and relaxation cycles. The full set of circulating components is called blood. Blood vessels are grouped into arterial and venous types depending on if they flow away from the heart (arterial) or they return to the heart (venous). The biggest vessels are connected to the heart, decreasing in size as they are spread out into the tissues (see Fig.1) with diameters ranging from 4 cm to 2  $\mu\text{m}$  [10]. See Table 1 for more references values for the diameter of different vessel types. The typical distance between bifurcations is hundreds of microns to a few millimeters [11].

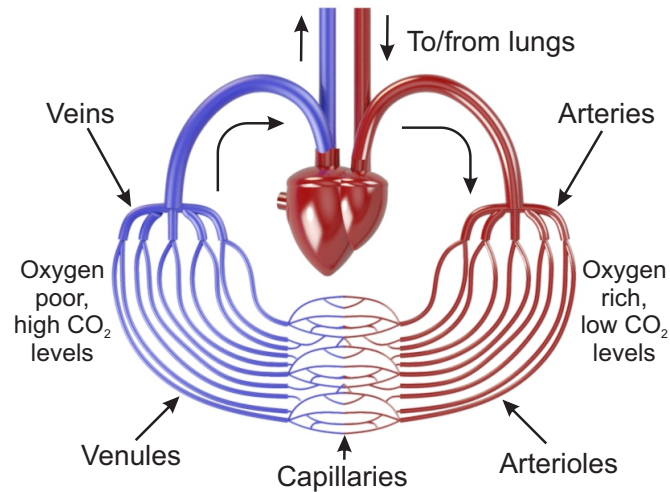


**Fig. 1:** Sketch of the cardiovascular system. The different vessels types are shown

In the smaller vessels, called capillaries, a higher exchange of substances with the tissues occurs. The capillaries are densely interconnected and together with arterioles and venules constitute most of the area of the circulatory system. This subsystem is usually called microcirculation.

vessel type	diameter (mm)	mean flow velocity (mm s <sup>-1</sup> )	wall shear rate (s <sup>-1</sup> )
aorta	16–32	600	150–300
artery	2–6	150–500	200–2000
arteriole	0.04	5	1000
capillary	0.005–0.01	0.5–1	400–1600
post-capillary venule	0.02	2	800
venule	0.1	5	400
vein	5–10	150–200	120–320
vena cava	20	100	40–60

**Tab. 1:** Vessel types and their diameter, mean flow velocity and wall shear rate [6].

## 2.2 What is blood?

In average, 5 L of blood circulate through the vessels in an adult human. It is composed, 55% of a liquid solution called plasma and 45% of red blood cells (RBCs), white cells, and platelets, together called blood cells. The number of RBCs per unit volume is about  $5 \times 10^6 \text{ mm}^{-3}$ , followed by platelets ( $250\text{--}500 \times 10^3 \text{ mm}^{-3}$ ) and white cells ( $4\text{--}11 \times 10^3 \text{ mm}^{-3}$ ). Blood plasma consists of 93% water and the remaining 7% of substances such as mineral ions, nutrients, glucose, amino acids, fatty acids, hormones and proteins [12]. Fig.2 presents a sketch of the blood and its main constituents flowing

through a blood vessel. The fraction of RBCs in blood is called hematocrit. In narrow tubes, the volume fraction of RBCs is called tube hematocrit,  $H_t$ .  $H_t$  decreases as the diameter of the tube in which the blood is flowing decreases. This is known as Fahraeus effect [13].

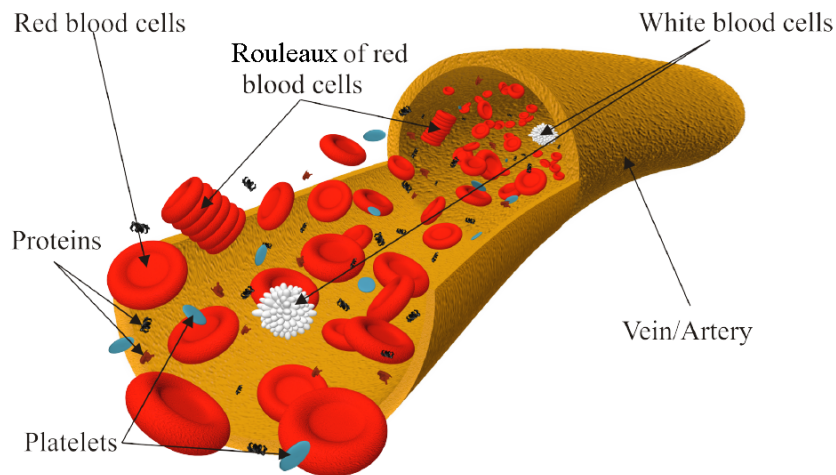


**Fig. 2:** Main blood components are represented flowing through a blood vessel: red blood cells, white cells, platelets and plasma proteins [1].

## 2.3 Red blood cells

RBCs are the result of a cascade of transformations of stem cells during erythropoiesis in the bone marrow. In the last stage, the nucleus is released and the cytoplasmic components are transformed into a solution of hemoglobin proteins. In this state, RBCs are called reticulocytes and are discharged into the circulatory system [14–16] where, after 2-3 days of circulation, they mature into the known discocyte shape. Other types of shapes of RBC beside discocytes can be found in blood in a healthy person. The most frequent are the so called stomatocytes whose percentage is normally below 3%. Another frequent shape observed mainly *in vitro* is called echinocyte and can be provoked in the vicinity of a charged surface like glass (cp. Fig. 3) [17, 18].

Some work has been done to predict these shapes based on the bilayer-couple hypothesis, where the mechanics of the fluid and elastic components of the cell (membrane and cytoskeleton, respectively) at equilibrium are used to model the material and to predict the transformation from discocyte to stomatocyte and from discocyte to echinocyte [17, 18].

At rest, mature discocyte RBCs are biconcave discs with a diameter of 7.5 to 8.7  $\mu\text{m}$ , a thickness of 1.7 to 2.2  $\mu\text{m}$ , an average surface area of 135  $\mu\text{m}^2$  and a mean volume of 94 fL [19–21]. The reduced volume (volume of the cell normalized by the volume of a sphere with the same RBC average surface area) is around 0.6. Of course these values

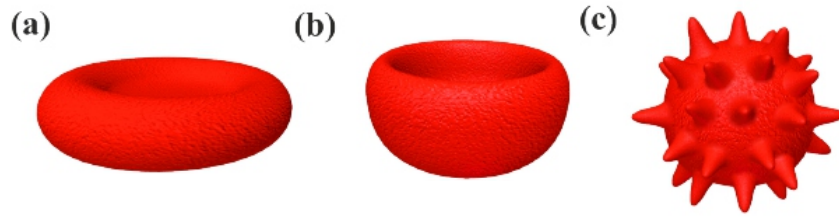


**Fig. 3:** Typical shapes of human RBCs: (a) discocyte, (b) stomatocyte and (c) echinocyte [1].

have a natural variability and can vary within the RBC population of a individual and from one individual to another.

However, during the approximately 120 day lifespan of a RBC in the circulatory system, after which it will be removed from the circulation by the spleen [22], RBCs lose surface area and about 30% of their volume. The hemoglobin concentration increases by 14%, indicating that more water than hemoglobin is lost [23, 24]. As a consequence, older cells have an average volume of  $78 \mu\text{m}^3$  and surface area of about  $117 \mu\text{m}^2$ , compared to  $98 \mu\text{m}^3$  and  $148 \mu\text{m}^2$  in volume and surface area respectively in young cells. The reduced volume therefore increases over time from 0.58 to 0.64.

The typical viscosity of the inner RBC's solution is about  $\eta_{in} = 5 \text{ mPas}$  at  $37^\circ\text{C}$ , a value that also changes with the age of the cells (due to, as mentioned, changes in hemoglobin and water concentration). Hemoglobin is formed by 4 chains: two  $\alpha$  and two non- $\alpha$  (called  $\beta$ ,  $\gamma$  or  $\delta$ ), each containing a heme group with an iron in its ionic form at the center (ferrous iron,  $\text{Fe}^{2+}$ ) where the oxygen is attached to (see Fig.(4)). In healthy adult subjects, the most common human hemoglobin tetramer is the hemoglobin A (HbA) formed by two  $\alpha$  and two  $\beta$  chains. Less common but still existing in healthy adults is the tetramer formed by two  $\alpha$  and two  $\delta$  chains, variant of hemoglobin A called hemoglobin A2 (HbA2). A third tetramer found in adults is the hemoglobin F (HbF) formed by two  $\alpha$  and two  $\gamma$  chains.

The oxidative properties of the hemes are essential but toxic [25] if they are released outside their hosting place. The RBCs not only protect an organism against the toxicity of hemoglobin, but also have the property to locally tune the hemoglobin's affinity for oxygen by a response to external chemical agents present in plasma. The concentration of hemoglobin inside each RBC is limited to approximately 35 g per 100 ml due to its finite solubility limiting the amount of oxygen that can be transported by each cell.

A RBC's membrane is composed by a lipid bilayer with a thickness of about 4–5 nm, interrupted by transversal and superficial proteins. It has an inner-side (intracellular region) attached spectrin network of proteins called cytoskeleton (see Fig.5) and outer-side (extracellular region) attachment of peptidoglycans. Together, the outer-side membrane proteins and peptidoglycans are called glycocalyx [26].

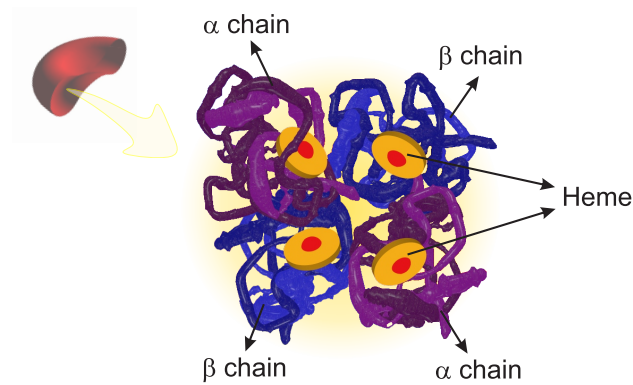


**Fig. 4:** Representation of a hemoglobin protein and the arrangement of its two  $\alpha$  chains, two  $\beta$  chains and four Heme groups.

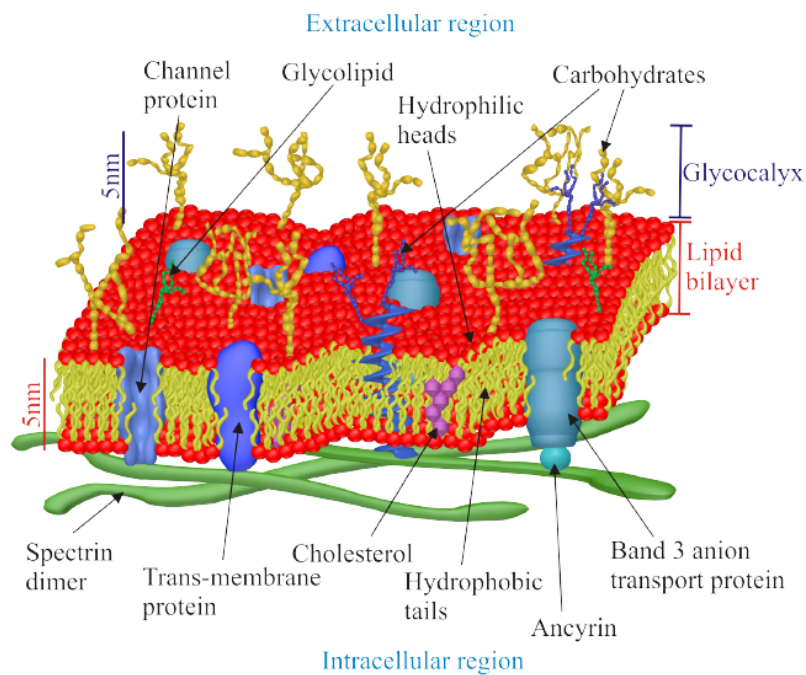


**Fig. 5:** Schematic drawing of RBC's lipid bilayer membrane, its components and the spectrin network/cytoskeleton attached to it intracellular face [1].

The membrane regulates the passage of molecules while the cytoskeleton maintains the membrane cohesion, and thus the mechanical stability and integrity of the cell, by external mechanical stresses under which the shape of the cell can change and deform. RBC deformation can also occur without changes in the global shape of the cell but due to movement of the bilipid membrane (for example). The bilipid membrane can be

considered as an incompressible 2D viscous liquid [27] or by the relative movement of one membrane leaflet with respect to the other, that can also induce viscous dissipation [28]. The shear resistance produced by the RBC's membrane can only originate from the inner-attached cytoskeleton.

In general terms, two independent modes of deformation are necessary to describe the elastic state of the RBC, considering that local and global changes on the membrane are small: the simple shear at constant surface area and the out-of-plane bending [29]. The elastic moduli which relate to the RBC's deformation induced by tangential tension forces  $T_{ij}$  and bending moments  $M_{ij}$  are the stretching modulus  $K$ , the shear modulus  $G_S$  and the bending modulus  $K_B$ . 2D viscous moduli are associated with the rate of deformation of each modulus:  $\mu_a$  and  $\mu_S$  are the extensional and shear viscosity respectively and  $\mu_B$  is the viscosity associated with the rate of change of the RBC's curvature [30]. Fig.6 shows a sketch of the RBC's membrane deformations and the elastic and viscous moduli associated with them. Table 2 shows the typical values of each elastic modulus.

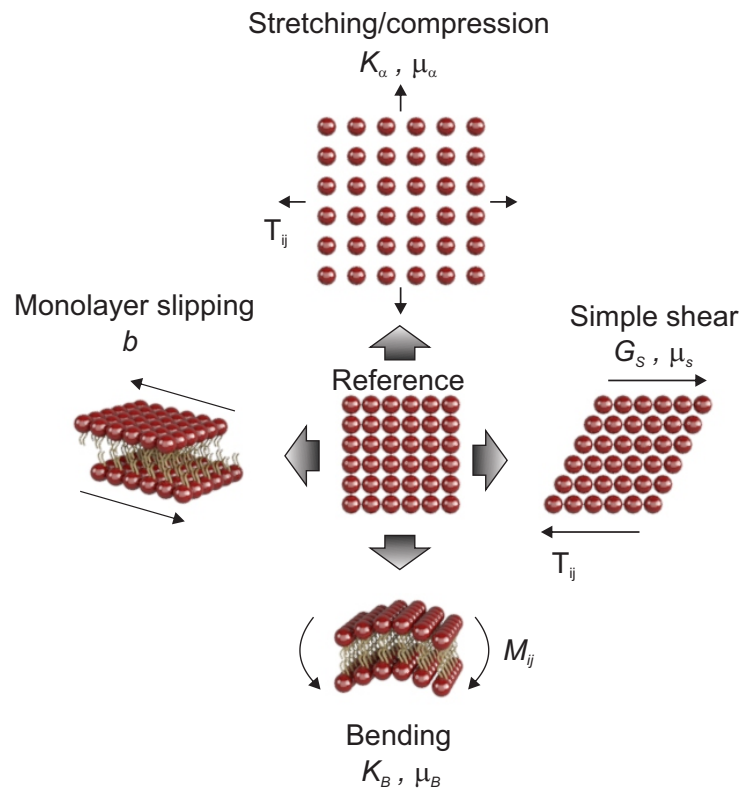


**Fig. 6:** Scheme of four modes of deformation of a RBC's bilipid membrane.

Another important factor that determines RBC deformability is the contrast between the inner viscosity of cell and the viscosity of its suspending media.

In summary, RBCs are highly deformable bodies, able to squeeze through small capillaries,

Modulus	Average value	Units
$G_S$	$5.5 \pm 3.3$	$\mu\text{N m}^{-1}$
$K_\alpha$	$399 \pm 110$	$\text{mN m}^{-1}$
$K_B$	$28.75 \pm 22.5$	in units of $k_B T = 4 \times 10^{-21} \text{ J}$

**Tab. 2:** Typical elastic moduli values of RBC's membrane [7].

enabling circulation throughout our body.

Vesicles can mimic several aspects of the behavior of RBCs. They are closed phospholipid bilayer membranes, encapsulating an inner fluid and suspended in an outer fluid, with the corresponding dynamic viscosities  $\eta_{in}$  and  $\eta_{out}$ . Their membrane exhibits three kinds of strain: stretching, tilting and bending. In general, the curvature is the only strain governing the shape of non-spherical vesicles [31]. The total elastic bending energy can therefore be written in the most simplified form as the addition of two contributions, the mean and the Gaussian curvatures

$$E_c = \frac{\kappa}{2} \oint (c_1 + c_2 - c_0)^2 dA + \kappa_G \oint c_1 c_2 dA \quad (1)$$

where  $c_1 = 1/R_1$  and  $c_2 = 1/R_2$  are the principal curvatures,  $c_0$  is the spontaneous curvature,  $dA$  is the area element, and  $\kappa$  and  $\kappa_G$  are the bending and the Gaussian curvature moduli. In our two-dimensional model, the Gaussian curvature is an irrelevant constant owing to the property  $\oint c ds = \oint \frac{d\theta}{ds} ds = 2\pi$ , where  $ds$  is the arc length and  $d\theta$  is the corresponding tangential angle. By considering only symmetrical membranes – same composition of phospholipids – the spontaneous curvature term can be disregarded (i.e.  $c_0 = 0$ ). The incompressibility and in-extensibility of the membrane are fulfilled by the use of a Lagrange Multiplier  $\zeta$ . The subsequent total energy is expressed as

$$E_c = \frac{\kappa}{2} \oint c^2 ds + \oint \zeta ds \quad (2)$$

The two-dimensional membrane force is then obtained by calculating the functional derivative of eq.2:

$$\mathbf{f}_{struct \rightarrow fluid} = -\frac{\delta E_c}{\delta \mathbf{X}} = \kappa \left[ \frac{\partial^2 c}{\partial s^2} + \frac{c^3}{2} \right] \mathbf{n} - c\zeta \mathbf{n} + \frac{\partial \zeta}{\partial s} \mathbf{t} \quad (3)$$

where  $\mathbf{n}$  and  $\mathbf{t}$  are namely the normal and the tangent unit vectors at a position vector  $\mathbf{X}$  belonging to the membrane.

## 2.4 Red blood cell aggregation

A wide variety of high-molecular-weight proteins are dispersed in the blood plasma fulfilling many physiological functions. The most important mechanical impact is their effect on blood rheology. The protein fibrinogen is the main component responsible for the

aggregation of RBCs into three-dimensional complex structures called *rouleaux*, [6, 32] similar to stack of coins.

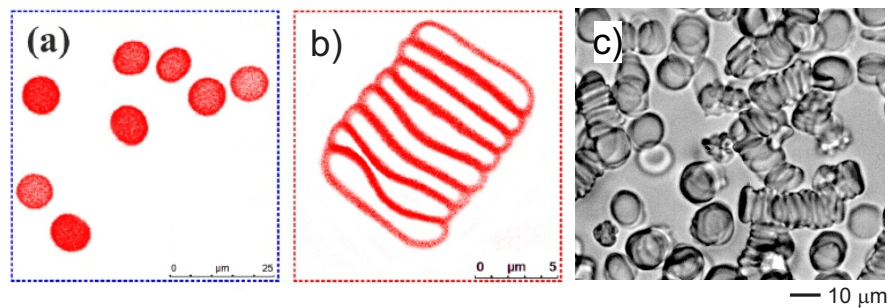


**Fig. 7:** a) and b) are fluorescence images of the cell membrane taken under a confocal microscope and c) bright field image. a) shows RBCs in buffer solution, b) rouleaux of RBCs in 8 mg/ml of fibrinogen and c) rouleaux of cells suspended in 20 mg/ml of dextran 70 kDa. Image modified with permission from [1].

The origin of the mechanism of aggregation is still not clear. In the early 1950's, Asakura and Oosawa introduced the depletion theory to explain the interaction force between two large spherical particles due to smaller particles (macromolecules) flowing around them [33]. The exclusion of macromolecules from the area between the large spheres induces an osmotic pressure acting as an attractive force leading to aggregation as shown in Fig.8. This model was adapted for RBCs, resulting in a theoretical model that includes the effect of the polymer concentration, the polymer physiochemical properties on depletion layer thickness, and the polymer penetration depth into the RBC glycocalyx [34].

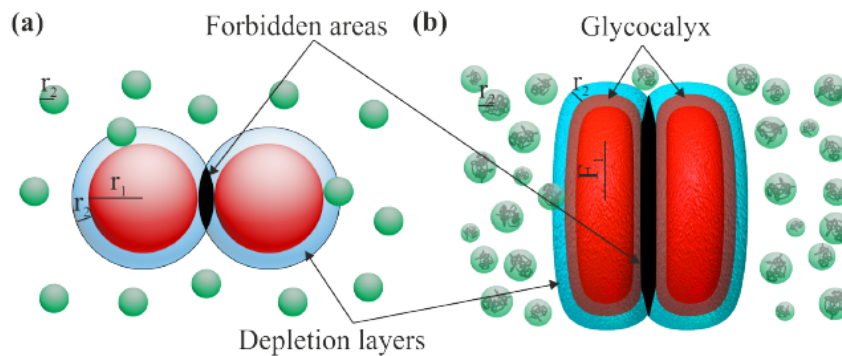


**Fig. 8:** (a) Depletion of large spheres induced by surrounding smaller spheres. The depletion layer is shown in blue and the forbidden area in black. (b) Depletion of RBCs due to surrounding macromolecules [1].

The theoretical predictions were in good agreement with the small amount of available

experimental data concerning the quantification of RBCs adhesion energy via micropipette aspiration [35] and a recent single cell force spectroscopy approach used to measure the adhesion energy between two RBCs in the presence of macromolecules Dextran [36].

Numerically, an approach based on a Lennard-Jones potential has been used to simulate the role of macromolecules on the flow of RBCs in micro-circulation [2, 37]:

$$\phi(r) = 4\epsilon \left[ \left( \frac{\sigma}{r} \right)^{12} - \left( \frac{\sigma}{r} \right)^6 \right] \quad (4)$$

The weak depletion attraction and the strong electrostatic repulsive forces at large and short distances are the negative derivative of the intercellular interaction potential

$$\mathbf{f}^\phi(\mathbf{X}) = - \int_{\Sigma_{j \neq i} \partial\Omega_j} \frac{\partial\phi(r)}{\partial r} \frac{\mathbf{r}}{r} ds(\mathbf{Y}) \quad (5)$$

where  $\epsilon$  and  $\sigma$  denote the surface energy and the zero force length distance.  $\mathbf{r} = \mathbf{X} - \mathbf{Y}$ ,  $r = \|\mathbf{X} - \mathbf{Y}\|$ , and  $\mathbf{X}$  and  $\mathbf{Y}$  are two position vectors belonging to the  $i$ -th and  $j$ -th membrane ( $\partial\Omega$ ), respectively. The well-depth is the equivalent of the surface energy. A second model to explain aggregation between RBCs is the bridging theory, which assumes that the RBC membrane adsorbs surrounding macromolecules and forms bridges with the neighbouring RBCs, leading to the formation of an aggregation if the adhesion forces exceed that of the disaggregating forces [38, 39]. The nature of the adsorption could be specific or unspecific binding. In the first case, macromolecules and proteins can bind through specific points. In the second case, several points in the macromolecules can bind different proteins on the membrane as represented in Fig.9. However, the maximum strength between the cells due to bridging could occur when the cells are covered by 50% of macromolecules. Lower and higher concentration of macromolecules should produce a weaker interaction between the cells.

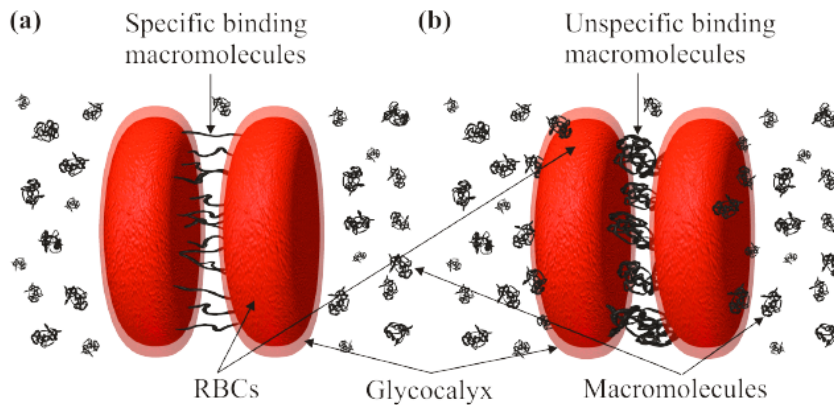


**Fig. 9:** Bridging theory where (a) specific binding and (b) unspecific binding of macromolecules between two RBCs are formed [1].

A third possible explanation could be the bridging-depletion phenomena in which depletion occurs due to the fact that a RBC is covered by macromolecules to the extent that bridging can no longer occur (see Fig.10). This proposal is inspired by the research performed by Fanatoni et al. [40] where depletion and bridging can co-exist in a colloidal system of spheres with small and larger diameters.

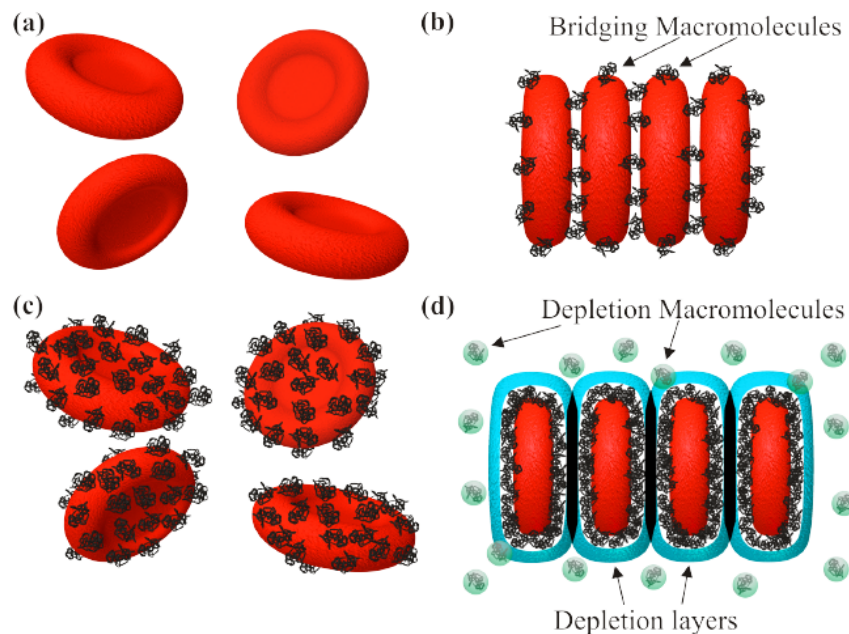


**Fig. 10:** Different stages of the bridging-depletion proposal on (a) RBCs. In (b) is shown macromolecules adsorbed by RBCs and thus, inducing aggregation. Increasing the concentration of macromolecules should decrease the interaction energy between cells due to bridging until the cells do not attract anymore as is shown in (c) and then, start to induce aggregation due to depletion (d) [1].

## 2.5 Blood flow in microcirculation

RBC deformability and RBC aggregation properties are key regulators of blood flow structure in both macro- and microcirculation. Nonsymmetry of deformable and rigid particles is a sufficient condition to break spatial and temporal symmetries of Stokes flow and induce particle migration away from walls and across the streamlines in low Reynolds number flows. Examples of such migrations are noticeable in liquid drops [41–43] and lipid vesicles [44–46]. The deformation of RBCs at high enough wall shear rate, induces a force which pushes the cells away from vessel walls; the subsequent cell migration towards the center of the vessel form a cell-free layer (CFL) [11, 47] that contributes to the decrease of blood viscosity which occurs with the decrease of tube radius. This phenomenon relating the viscosity and tube radius is known as the Fahraeus and Lindqvist effect [48]. However, the collisions of cells counteracts this migration,

when two deformable cells collide, the cells experience an irreversible cross-stream displacement, causing an overall decreased CFL in comparison to flows of more diluted particles [32, 49–51]. Over time, collisions lead to a diffusive behavior called shear-induced diffusion.

To understand this behavior, one has to understand how a particle disturbs the flow around it, the effect of the presence of a wall close to the particle, and the effect of the collisions between particles when there is more than one particle involved.

### 2.5.1 Boundary integral method

The equation of motion of the disturbed flow in the suspending media around deformable particles can be solved through a reformulation of the Stokes equations into a boundary integral representation [52] and coupled with the deformed object as RBCs or vesicles. The specific Green's functions satisfying the no-slip boundary at the two boundaries are calculated using the images method and a Fourier transform [53, 54]. The velocity along the membrane is expressed as

$$\begin{aligned} \mathbf{v}(\mathbf{X}_0) = & \frac{2}{1+\lambda} \mathbf{v}^\infty(\mathbf{X}_0) + \\ & \frac{1}{2\pi\eta_{out}(1+\lambda)} \int_{\Sigma_i \partial\Omega_i} \mathbf{G}(\mathbf{X}, \mathbf{X}_0) [\mathbf{f}_{struct \rightarrow fluid}(\mathbf{X}) + \mathbf{f}^\phi(\mathbf{X})] ds(\mathbf{X}) \\ & + \frac{(1-\lambda)}{2\pi(1+\lambda)} \int_{\Sigma_i \partial\Omega_i} \mathbf{v}(\mathbf{X}) \cdot \mathbf{T}(\mathbf{X}, \mathbf{X}_0) \cdot \mathbf{n}(\mathbf{X}) ds(\mathbf{X}) \quad (6) \end{aligned}$$

where  $\mathbf{v}^\infty$  is the velocity of the imposed Poiseuille flow in the absence of particles,  $\mathbf{G}$  and  $\mathbf{T}$  are the Green's function for two parallel walls and its associated stress tensor, and  $\lambda$  is the viscosity contrast between the inner and outer fluids, namely  $\eta_{in}$  and  $\eta_{out}$ . The position of the nodes is then advected in time using an Eulerian explicit scheme. This model has been developed in the Laboratoire Interdisciplinaire de Physique (LIPhy) in Grenoble and used by our group to study the flow of single cells and clusters in the micro-circulation [37, 55] by considering 2D vesicles, and to investigate the rheological properties of blood [56].

An increase in both RBC deformability and aggregation has been shown to emphasize cell axial migration, extending the width of the CFL and decreasing the apparent bulk viscosity of blood [57]. Since aggregation is a reversible process with shear rate (at high shear rates aggregates are destroyed and cells separate from one another), blood under physiological conditions behaves as a shear-thinning fluid [58]. A rich dynamics in RBCs occurs when the shear rate increases: RBCs successively tumble, roll, deform into rolling stomatocytes and finally adopt highly deformed polylobed shapes [59].

In terms of dynamics of RBCs, and as already mentioned in previous sections, the simple shear at constant surface area and the out-of-plane bending of the membrane tend to resist deformations by external stresses exerted on the cells. A way to compare the contribution of each of these components in RBC deformation in flow is through the capillary number  $Ca$  where  $Ca_S$ , the capillary number due to shear elasticity and  $Ca_B$ , the capillary number for bending resistance, are defined as

$$\begin{aligned} Ca_S &= \frac{\eta_{out}\bar{v}}{G_S} \\ Ca_B &= \frac{\eta_{out}\bar{v}a^2}{K_B} \end{aligned} \quad (7)$$

where  $\eta_{out}$  is the viscosity of the media,  $G_S$  the shear modulus,  $K_B$  the bending modulus,  $\bar{v}$  the average RBC velocity and  $a$  a characteristic length of the system, that can be taken as the cell radius.

## 2.5.2 Margination

RBC axial migration influences the placement of the other circulating cells as white cells and platelets, with respect to the vascular wall [60–64], a phenomenon known as margination (see Fig.11). Margination of white cells and platelets has a physiological importance as cells need to be near the vessel walls to deal with inflammation and hemostasis [63, 64]. In recent years, microfluidic experiments have taken advantage of this behavior to separate white cells from RBCs [65–69] and platelets [70, 71].

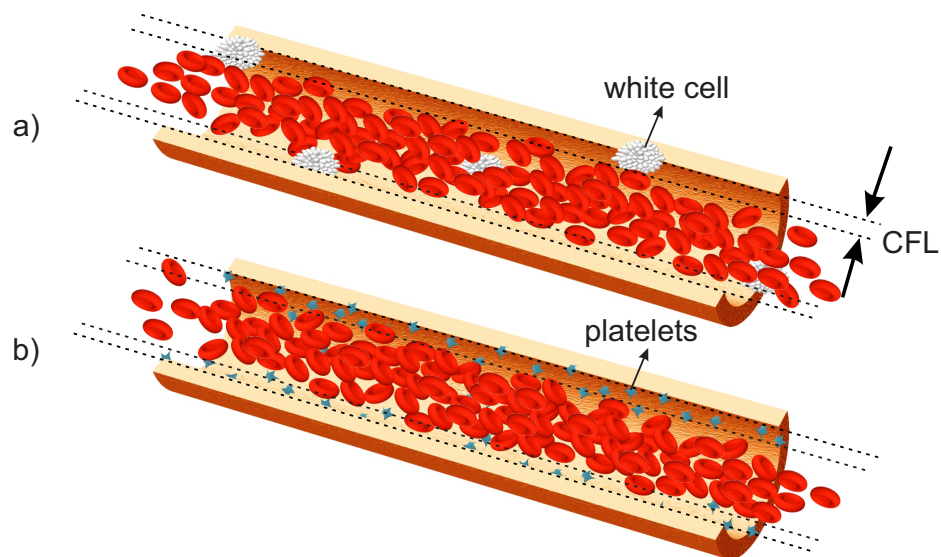


**Fig. 11:** Representation of the CFL and margination of a) white cells and b) platelets due to migration of red blood cells to the center of blood vessels.

Both *in vivo* and *in vitro* experiments have focused on margination phenomena depending

on hematocrit level, shear rate, channel width and RBC aggregation. However, it is interesting to notice that the main physical differences between platelets, white and red cells are their size, shape and rigidity: spherical white cells are larger than discocyte RBCs and RBCs are larger than the disk-like platelets. Platelets and white cells are stiffer than RBCs. Still, the question is: which is the main factor influencing the margination phenomenon? This remains an open question that will not be addressed in this study.

In white blood cells experiments, margination has been found to be more sensitive to shear rate than to hematocrit level. In fact, margination is mitigated at increasing shear rates [64] and channel width [65, 69, 72]. On the contrary, RBC aggregation seems to enhance margination when shear rate decreases [73]. In simulations, it has been shown that margination of white blood cells increases when their deformability decreases [67].

In platelet experiments, contrary to white cells, the concentration of platelets near the wall increases when hematocrit increases [74] as well as when shear rate increases [75]. In simulations the role of deformability of RBCs has been explored in platelet margination. Results indicate that increasing the rigidity of RBCs decreases the rate of platelet margination [76], and decreasing the viscosity ratio between RBCs and the external medium leads to an increase in margination rate [77], highlighting again the role of deformability of RBCs in the margination process.

The experiments and simulations mentioned above do not separate the role of size, shape and rigidity. The most comprehensive studies that separate these parameters consider a binary suspension of elastic capsules that does not capture all aspects of red blood cell properties and dynamics. Nevertheless, these studies proposed a model that can separate the effect of shape, size and deformability in order to explain segregation (margination and demargination) phenomena in shear flow, isolating the effect of non constant shear rate in margination. These studies also consider capsules to be neutrally buoyant, i.e., with the same density as their suspending media taking into account the fact that the inner capsule fluid and the suspending media viscosities are the same.

The main results of such studies as a simplified drift-diffusion theory, developed to understand and predict the segregation of multicomponent suspensions of deformable particles. The theory requires an input of migration, drift and diffusion coefficients [78], which should be obtained via experiment or numerical simulation.

The proposed model takes into account the two key processes already discussed: wall-induced migration that push the capsules to the center of the channel and hydrodynamic pair-collisions (shear-induced), which homogenize the capsules distribution and could be due to homogeneous (same particle type) or heterogeneous (different particle type) collisions [79–82].

### Role of shape in margination

In terms of shape, hypothetical spherical platelets marginate more than discocytes with the same volume [77]. There are also examples of microorganisms in flow, such as bacteria, where different shapes enable different functions [83]. In drug delivery, shape seems to be an important design parameter for controlling biological responses as blood circulation and phagocytosis [84, 85].

### Role of size and rigidity in margination

In terms of rigidity, when there is a combination of stiff and flexible particles a heterogeneous collision causes stiffer particles to have a larger cross-stream displacement than flexible particles. In homogeneous collisions, cross-stream displacement is in between the two previous limits. In heterogeneous suspensions where stiff particles are the dilute component, they tend to concentrate in the near-wall region. This phenomenon can aid the separation of malaria-infected cells from healthy ones [86] since malaria-infected cells are stiffer [87] than healthy RBCs.

### 2.5.3 RBC shape in confined flow

When RBCs flow in tube with diameters above but close to  $10\ \mu\text{m}$ , the typical shapes observed are slipper-like (see a) in Fig.13) and centered parachute as is shown in Fig.12. It is suggested that these shapes could increase the area exposed to gas exchange and thus have a functional significance. While these shapes were first observed in 1963 and 1969 [88, 89], several studies have since showed the existence of both for different experimental conditions [90–94], although all these studies considered 2D images. Recent 3D reconstruction of single RBCs flowing through confined channels showed that a third shape named *croissant* can be considered (see b) in Fig.13). This shape is typically called parachute in 2D images. As mentioned, RBC can pass through capillaries as small as  $3\ \mu\text{m}$ .

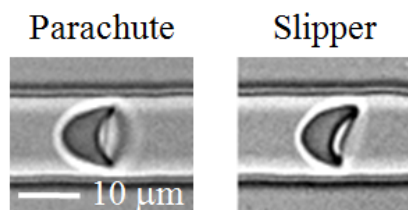


**Fig. 12:** 2D images of the typical RBC shapes observed flowing through microcapillaries: parachute (left) and slipper (right).

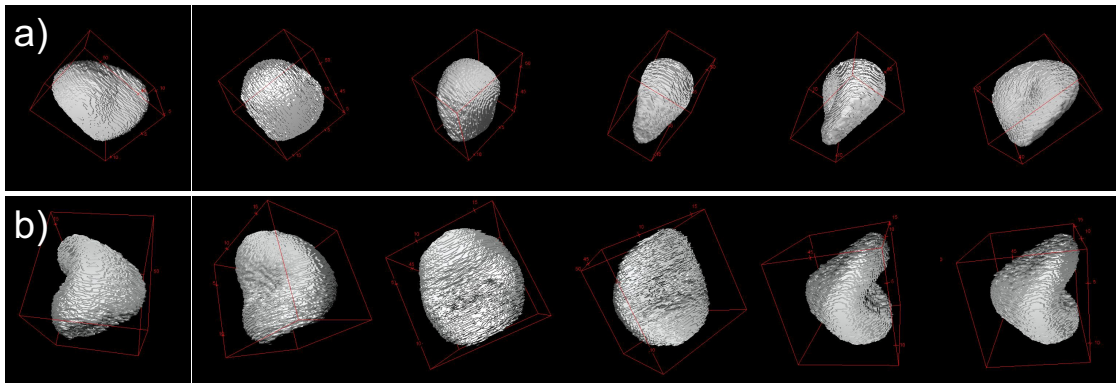


**Fig. 13:** Sequence of images of a reconstructed 3D slipper-like a) and croissant b) RBCs flowing through a high confined microchannel. The 3D reconstructions were made by A. Christ from AG Wagner.

### 2.5.4 Clustering of red blood cells

For hard-sphere colloidal systems, it has recently been shown that both bridging and depletion can simultaneously affect the process of crystallization and self-assembly in flow [95, 96]. However, there is quantitative disagreement between numerical predictions and experiments on the kinetics of phase transitions, and it is predicted that hydrodynamic interactions must be considered to resolve this discrepancy [97]. There is some knowledge of the mechanisms of hydrodynamic interaction in a confined flow of hard spheres [98] and spherical droplet suspensions [99] where even phonon-like excitations can be observed. However, much less is known about the case of soft deformable objects. Recent detailed numerical predictions show that soft objects should have a much stronger tendency to form clusters and display richer dynamics than hard systems [100]. RBCs can be considered as model objects to study the flow of soft objects in confinement [7], where the physical parameters, such as deformability or chemical interaction potentials, are as important as the surrounding hydrodynamics. A recent review on the behaviour of blood in micro-capillaries *in vitro* was given by Guido et al. [101].

In general terms, observations *in vivo* and *in vitro* show that RBCs tend to form well-organized clusters (see Fig.14) [2, 90, 102] in the microcapillary network even if tube hematocrit  $H_t$  is as low as 1% [2, 37, 103]. Parachute and slipper-like shapes may be present in the same cluster, and in the case of clusters formed by two RBCs (see Fig.15), a hydrodynamical distance, dependent of capillary number, is reported [2]. The physical origin of cluster formation can be explained by either long-range hydrodynamic interaction [102, 104–107] or a short-range aggregation mechanism [37], which causes *rouleaux* formation by the plasma macromolecules [6]. The existence of *rouleaux* and their relative contribution in cluster formation have been also explored in this study [2]. Numerical simulations in spherical particles [108] have shown that, at a distance of the order of the particle size, streamlines are disturbed near spherical particles due to the presence of the wall. In such a case, the trajectories of two particles can overlap,

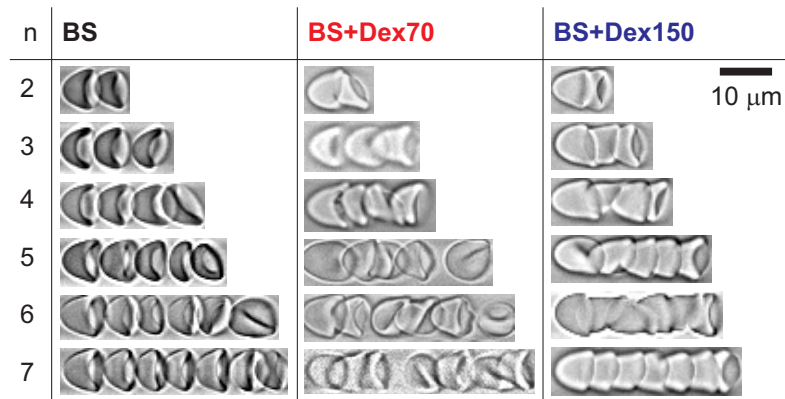


**Fig. 14:** Snapshot of the typical RBC cluster configurations of type  $n$ , which contain  $n$  cells for an imposed  $\Delta P = 100$  mbar [2].

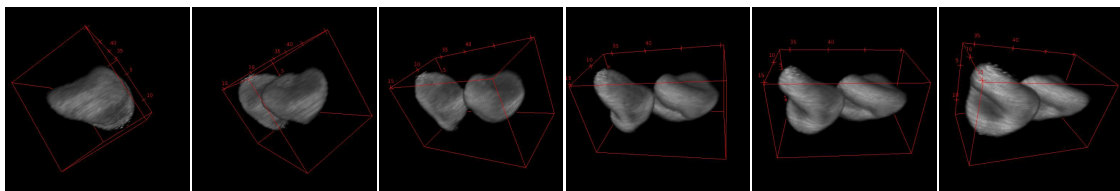


**Fig. 15:** Sequence of images of a reconstructed 3D cluster formed by 2 RBCs flowing through a high confined microchannel. The 3D reconstructions were made by A. Christ from AG Wagner.

causing particle interaction. The interaction should be short-range and decay with the square of the distance.

## 2.6 Sick cell anemia

### 2.6.1 Overview

Sickle cell anemia (SCA) is a genetic and hereditary disease affecting 50 million people around the world, ranked as the fourth priority by the World Health Organization. It is produced by an alteration or mutation of the hemoglobin structure which makes it less soluble: a single nucleotide mutation in the  $\beta$ -globin gene results in the substitution of glutamic acid by valine at the sixth position of this  $\beta$  chain. In this state, the hemoglobin is called hemoglobin S or HbS.

Sickle cells occur when a person inherits an abnormal copy of the hemoglobin gene from each parent. A person with a single abnormal copy (heterozygous for HbS) usually does not have symptoms and is said to have sickle-cell trait. Homozygosity for HbS or SS, though is not the only form of sickle cell disease, is the most common (about 70%).

Interestingly, sickle cell anemia confers a genetic advantage against plasmodium falciparum, one of the most virulent forms of malaria, mainly by inhibiting the growth of the parasite or inducing the recognition of infected RBCs by the immune system [109–112].

As is shown in Fig.16, during the human fetal stage, the predominant hemoglobin tetramer after HbA is HbF. Shortly before birth and after birth, the rate of  $\gamma$  chains drops rapidly in favor of  $\beta$  chains. Therefore, the first phenotypic signs of sickle cell disease do not appear before  $\gamma$  genes are substituted and thus, sickle cell patients with HbF persistence consequently have consequence lower clinical severity.

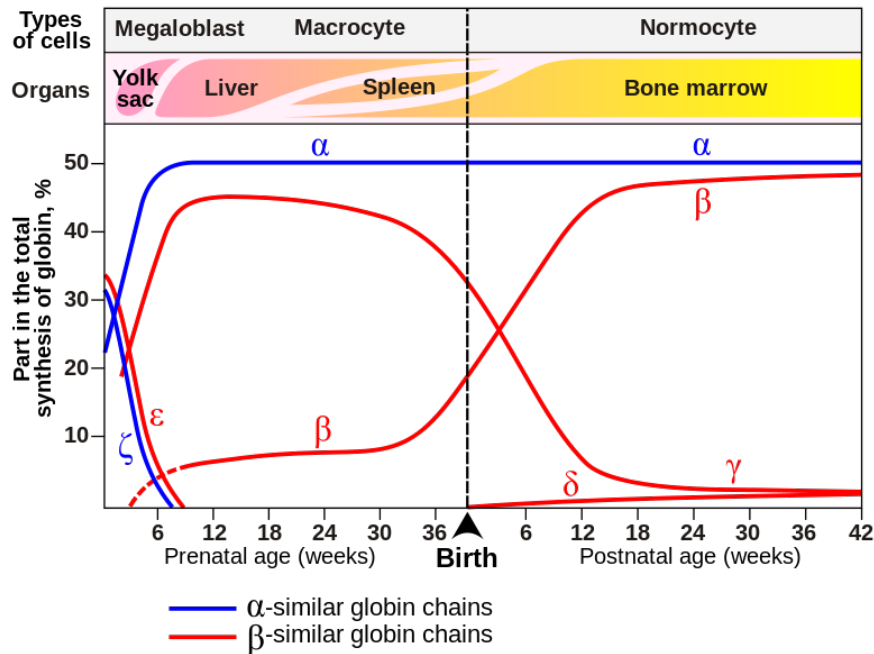


**Fig. 16:** Hemoglobin types before and after birth. Types of cells and organs in which the gene is expressed is shown [3].

### HbS Polymerization

In the absence of oxygen, the hydrophobic valine causes HbS to agglomerate and form rope-like fibers or polymers [113] as is sketched in Fig.17.

This phenomenon is reversible, because in the presence of oxygen, the polymers dissolve and sickle red blood cells (sRBCs) return to its original discocyte shape. In Fig.18, the images shown oxygenated sRBCs a) of a patient submitted to a deoxygenation b) and reoxygenation c) cycle as an example of the reversibility of the HbS polymerization formation.

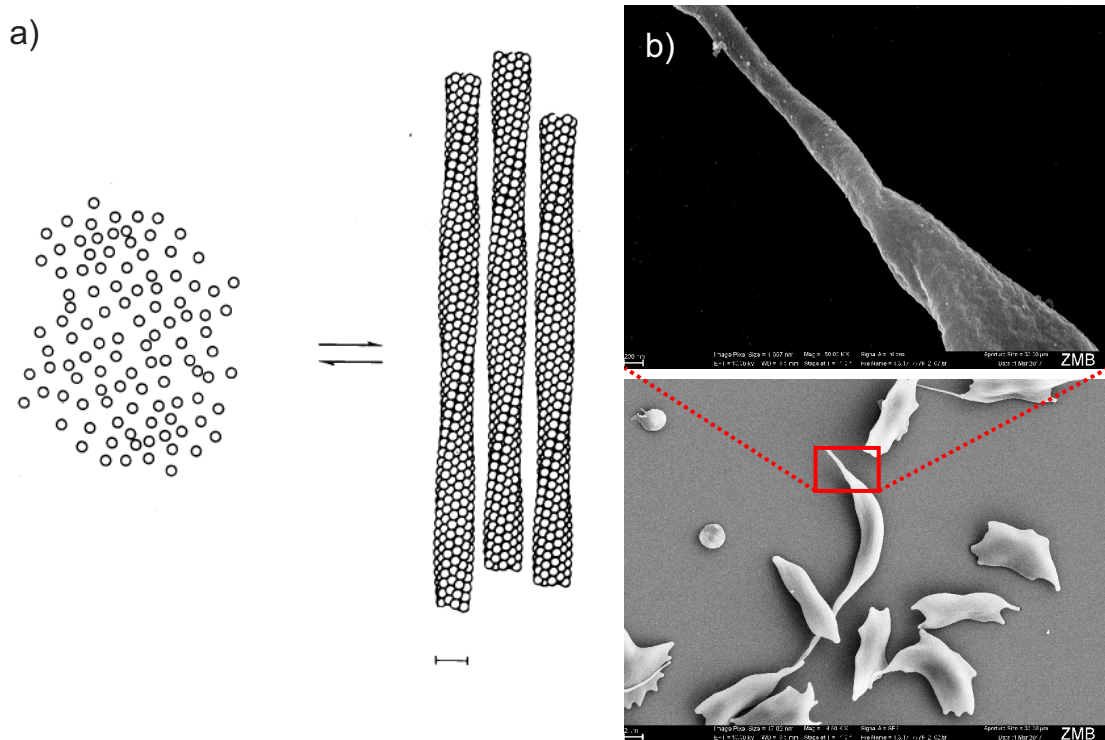


**Fig. 17:** a) Sketch of free HbS inside a sRBCs forming rope-like fibers of about 21 nm in diameter [4]. The rope-like fibers can be noticed in the zoomed image of the upper panel in b), of a deoxygenated sRBCs presented in the panel at the bottom. Images in b) were taken using a scanning electron microscope (SEM) by G. Simionato from AG Wagner.

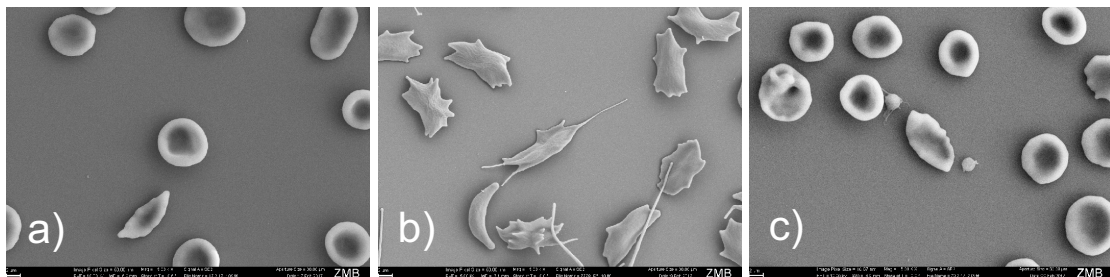


**Fig. 18:** Images of oxygenated sRBCs a) of a patient submitted to a deoxygenation (up to 1% of oxygen partial pressure) b) and reoxygenation c). The reversibility of the HbS polymerization can be noticed from the sequence of images from a) to c). However, in a) and c) some irreversible sRBCs are present (elongated and far from discocyte shapes). The images were taken using a scanning electron microscope (SEM) by G. Simionato from AG Wagner.

Several cycles of oxygenation and deoxygenation causes some irreversible changes as sRBCs gradually lose their plasma membrane and hydration [114–116] (see a) and c) in Fig.18). Due to polymerization, sRBCs have distorted shapes that lead to an increase in cell rigidity and membrane fragility [117, 118]. As a consequence, hemolysis of cells frequently occurs in the intravascular (about one third) and extravascular region (about

two thirds) [119], resulting in a shorter RBC lifetime of only 15 days [120] compared to 120 days for a normal RBC. Thus the average hematocrit in people with SCA is ~25%.

### sRBC deformation

sRBC deformability is significantly impaired, even in steady state conditions. This rheological behavior is mainly due to the elevated internal viscosity of irreversibly sickled cells and the reduced membrane flexibility of both irreversibly and transiently sickled cells [121]. The mean sRBC corpuscular volume is about 84.3 fL against 94 fL in healthy RBCs [8], and the mean corpuscular hemoglobin concentration (MCHC), defined as hemoglobin concentration/hematocrit, has a larger value than in healthy cells (see Table 3). In this respect, the shear modulus  $G_S$  of healthy RBCs and oxygenated sRBCs as a function of hemoglobin concentration has been compared by micropipette experiments [5]. In healthy cells this value remains constant for hemoglobin concentrations from 0.32 to 0.45 g/cm<sup>3</sup>, while for oxygenated sRBCs increases for hemoglobin concentrations from 0.32 to 0.38 g/cm<sup>3</sup> with a large increase for the most dense cells, with an hemoglobin concentration of 0.48 g/cm<sup>3</sup> (see Fig.19), 8 times stiffer than healthy cells.

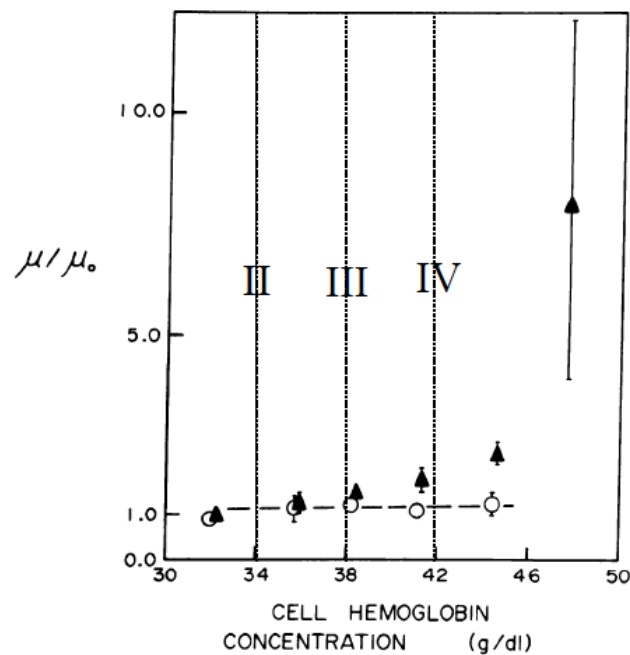


**Fig. 19:** Shear modulus  $G_S$  (here named  $\mu$ ) normalized by the healthy shear modulus of 0.32 g/cm<sup>3</sup> as a function of the intracellular concentration of hemoglobin MCHC. Empty circles are the values of healthy cells while triangles are the measured values of oxygenated sRBC [5].

Using a Laser assisted Optical Rotational Cell Analyzer (LORCA, RR Mechatronics, Hoorn, The Netherlands), and based on laser diffraction patterns obtained at user-defined

shear stress values (3 and 30 Pa), the elongation of RBCs was determined based on the values of the elongation index (EI) [8], that increases with increased RBC deformability. EI values for healthy RBC and sRBC are summarized in Table 3.

	AA ( $n = 52$ )	SCA ( $n = 21$ )
EI (at 3 Pa)	0.33±0.02	0.09±0.10
EI (at 30 Pa)	0.58±0.02	0.33±0.16
MCHC (g/dL)	33.5±1.2	35.6±1.1

**Tab. 3:** Values of the elongation index (EI) and mean corpuscular hemoglobin concentration (MCHC) for healthy RBCs (AA) and sRBCs in SCA.  $n$  indicates the number of donors for each case [8].

The percentage of oxygenated sRBC with MCHC higher than 0.37 g/cm<sup>3</sup> can reach 50% of the total population of cells while for healthy RBCs 90% MCHC values are in the range of 0.29 to 0.35 g/cm<sup>3</sup>. In general, MCHC is directly representative of RBC density, and it has a direct and strong impact on the rheology of blood, as it decreases sRBC deformability [8].

### sRBC adhesion

Rigid irreversibly sickled cells are less adherent than discocyte (oxygenated) sRBCs. This fact is more related to the decrease on deformability and shape than to the adhesion potential in the membrane [122], since artificially dehydrated deformable cells adhere less to endothelial cells compared to the original non-dehydrated deformable ones. Thus, adhesion can be related with the cell density (or MCHC level), since more dense and hence less deformable cells have lower adhesion potential to endothelial cells than the more deformable or less dense sRBC. However, plasma factors are an important parameter to take into account in the adhesion process [123]. Although the proteins which are responsible for an increase of adhesion of sRBC to endothelial cells is still unknown, the addition of albumin and fibrinogen to protein-free suspending medium at the highest concentrations found in plasma did not induce adhesion, implying that these plasma proteins are not involved in the process. However, the proteins that promote adhesion seem to be present in significantly higher concentrations in sickle cell plasma compared with normal plasma, since sRBC are more adherent in sickle plasma. Adhesion can be mediated by plasma factors, but can be also be induced by adhesion molecules [9] categorized as 1) red cell receptors, 2) adhesive bridging proteins, and 3) endothelial receptors (see Table 4 for a summary of this molecules). Sulfated glycolipids are exposed in the sRBCs membrane. CD36 and integrin  $\alpha_4\beta_1$  are expressed on reticulocytes under stress and can mediated adhesion when they interact with thrombospondin (TSP) and vascular cell adhesion molecule-1 (VCAM-1), respectively. Other adhesion molecules require signal transduction to be activated, like the integrin-associated protein (IAP) and intercellular adhesion molecule (ICAM-4).

Adhesive bridging proteins include TSP and von Willebrand (cWf) that are synthesized in endothelium and platelets, and can exist in soluble state in plasma, as well as expressed on the endothelial surface. The integrin  $\alpha_V\beta_3$  is the most prominent endothelial receptor.

sRBC receptors	adhesive bridging proteins	endothelial receptors
CD36	TSP	$\alpha_V\beta_3$
Sulfated glycolipid	TSP	$\alpha_V\beta_3$
Sulfated glycolipid	vWf	$\alpha_V\beta_3$
IAP	TSP	$\alpha_V\beta_3$
ICAM-4/ LW	$\longleftrightarrow$	$\alpha_V\beta_3$
PS	$\longleftrightarrow$	CD36
$\alpha_4\beta_1$	$\longleftrightarrow$	VCAM-1
Sialyl Lewis	$\longleftrightarrow$	P-selectin

**Tab. 4:** Potential mechanisms in sRBC adhesion to endothelium [9]. Sulfated glycolipids are exposed in the sRBCs membrane. Adhesive molecules on sRBCs can be activated by stress on the surface of the reticulocytes (CD36,  $\alpha_V\beta_3$ ) or on sRBC membrane by signal transduction (IAP and ICAM-4). Some of the molecules need adhesive bridging proteins to bind into the endothelial receptors while others can bind directly to the endothelial receptors.

Measurements of adhesion under defined shear stress revealed that sRBC adhesion to human endothelial cells was negligible above a shear rate of  $200\text{ s}^{-1}$  in a parallel plate flow chamber [124]. In the same study, the greatest adhesion was exhibit by the less dense sRBCs, the reticulocytes, and the least by the densest sRBCs. However, in *ex vivo* studies, infusion of oxygenated sRBCs resulted in adhesion of these cells to the postcapillary venules, where adherent sRBCs are able to withstand shear rates from about 200 to  $600\text{ s}^{-1}$ .

Under shear flow conditions, adhesion characteristics are determined by the ability of the cells to deform and establish sufficient areas of contact with endothelial cell surface, as well as differences in membrane mechanical and surface characteristics [123]. Then, sRBC density, shape and membrane characteristics play an important role in adhesion of sRBCs during flow conditions.

### sRBC aggregation

SCA patients are characterized by sRBC aggregation abnormalities. At steady state, sRBCs take longer to form aggregates [8] (see the aggregation half time  $t_{1/2}$  values in Table 5). The reason for this longer time remains up to date unknown. However, the robustness of the sRBC aggregates is 2 to 3 fold higher than aggregates between healthy cells [8] and higher than normal shear forces are required to disperse preformed sRBC aggregates. The increased minimum shear rate  $\gamma_{min}$  does not seem to be related to plasma fibrinogen concentrations since healthy and SCA blood had comparable values (see Table 5 for  $\gamma_{min}$  and fibrinogen concentration values). Fibrinogen is the main plasma protein responsible for RBC aggregation and hence comparable levels suggests a

role for cellular factors, like for example, glycocalyx properties. Since sRBC are exposed to increased oxidative stress, it seems possible that such stress may have a role in the specific RBC aggregation pattern observed for sRBC.

	AA ( $n = 16$ )	SCA ( $n = 21$ )
$t_{1/2}$ (s)	2.6±1.1	4.2±1.7
$\gamma_{min}$ ( $s^{-1}$ )	134.4±47.0	382.6±182.9
fibrinogen (g/L)	3.0±0.5	3.6±1.4

**Tab. 5:** Values of the aggregation half time  $t_{1/2}$ , minimum shear rate  $\gamma_{min}$  to disperse preformed sRBC aggregates, and fibrinogen concentration for healthy RBCs (AA) and sRBCs in SCA.  $n$  indicates the number of donors for each case [8].

The pathogenic potential of RBC aggregation within the microcirculation is dependent on the cohesive forces within the aggregate. The increase of the required shear forces might have important physiological consequences, especially at the microcirculatory level. It has been postulated that abnormal sRBC aggregation properties could play a role in the onset of vaso-occlusive events in SCA. Finally, it has been found that patients with higher sRBC aggregate strength are at higher risk to develop acute chest syndrome [125].

The effects of RBC aggregation on *in vivo* flow dynamics and flow resistance are complex and further studies are needed to better understand the association between RBC aggregation parameters and the severity of sickle cell disease.

### Cell free layer in SCA

There are not reported values of the CFL in SCA. However, due to the decreased deformability of sRBCs, it is expected that CFL thickness would be lower in a micro-circulatory network fed with SCA blood compared to healthy blood. sRBCs could be expected to flow close to the vessel walls than healthy RBCs, hence increasing the chance to interact with the vessel wall. Moreover, compared to healthy blood, SCA blood contains RBCs of various densities and thus deformabilities. Indeed, cell distributions under flowing conditions are probably different between healthy and SCA blood.

## 2.6.2 Vaso-occlusion

One of the main complications of the disease is the vasoocclusive events and the anemic state generated by a decrease in circulating sRBCs. Loss of sRBCs deformability by membrane stiffening was believed to be the main factor responsible for the jamming of cells, inducing vaso-occlusive events and progressive damage in the organs. But in the last decades different and more complex scenarios have been proposed [126] as the magnitude of the decrease in RBC deformability by itself does not predict the

severity of vaso-occlusion (VO). In fact, several studies have reported that patients with higher deformability are at a higher risk of developing frequent VO compared to those with lower sRBC deformability [116, 125, 127, 128]. This is an unexpected finding since sRBCs with higher deformability should demonstrate better migration to the center of the channels and thus better tissue perfusion. This could be related with the fact that sRBCs with the highest deformability are the most adherent to the vascular wall, though plasma proteins and adhesive molecules (see *sRBC adhesion* for details) are important parameters to consider in cell adherence and as a possible onset of VO and painful crisis [123].

However, other complex VO scenario have been proposed. One of those is related to the hemolysis of sRBCs as a triggering of the chain of events that leads to a VO episode. Hemolysis implies that HbS is present in blood plasma. (1) Free HbS triggers an inflammatory response in the blood vessels. (2) This inflammatory response could lead to leukocyte recruitment on endothelial cells and platelet activation and adhesion. At the same time, (3) free HbS molecules can bind to nitric oxide (NO) in solution in the plasma, reducing its bioavailability [129–131] and also producing oxydative damage [132, 133]. (4) NO acts as a vasodilatator and HbS-NO binding results in an imbalance of vasoconstrictor proteins that could lead to a strong vasoconstriction event (5), finally producing VO.

In another scenario of a VO event includes sRBC-endothelium interaction as a potential initiating mechanism of VO. A two step model of adhesion-induced VO in which preferential adhesion of deformable sRBCs (reticulocytes and discocytes) in postcapillary venules are followed by a trap of dense sRBCs (dense discocytes or irreversible sRBCs), increasing the transient times of the sRBCs, producing hypoxia, sickling of sRBCs, and finally VO [134, 135].

Finally, infections are often followed by the occurrence of VO due to the increased recruitment of white blood cells and their potential interaction with sRBCs in the microcirculation that can lead to a sluggish flow, increased transient times of the sRBCs, hypoxia, sickling of sRBCs, and VO (see Fig.21). Moreover, intermittent VO events may also induce an inflammatory endothelial phenotype, resulting in enhanced white cells-endothelium interactions [136].

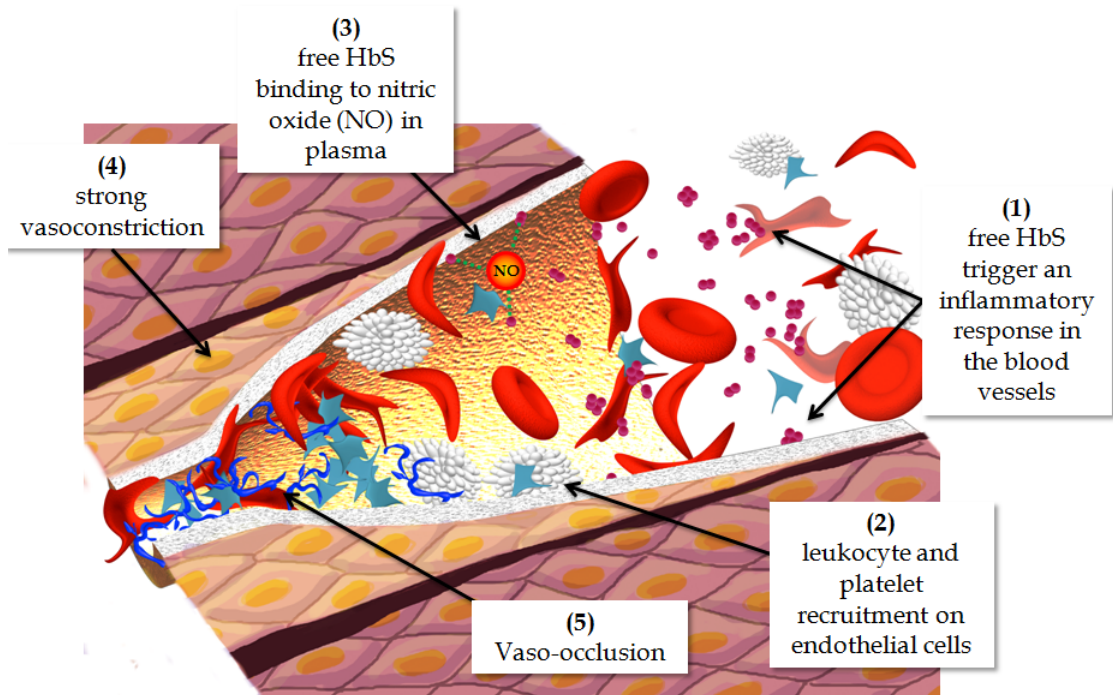


**Fig. 20:** Scenario of the chain of events leading to VO. (1) Free HbS triggers an inflammatory response in the blood vessels. (2) The inflammatory response leads to leukocyte and platelet recruitment on endothelial cells. (3) free HbS molecules can bind to nitric oxide (NO) in the plasma, reducing its bioavailability and producing oxidative damage. (4) HbS-NO binding results in an imbalance of vasoconstrictor proteins leading a strong vasoconstriction event (5) producing VO.

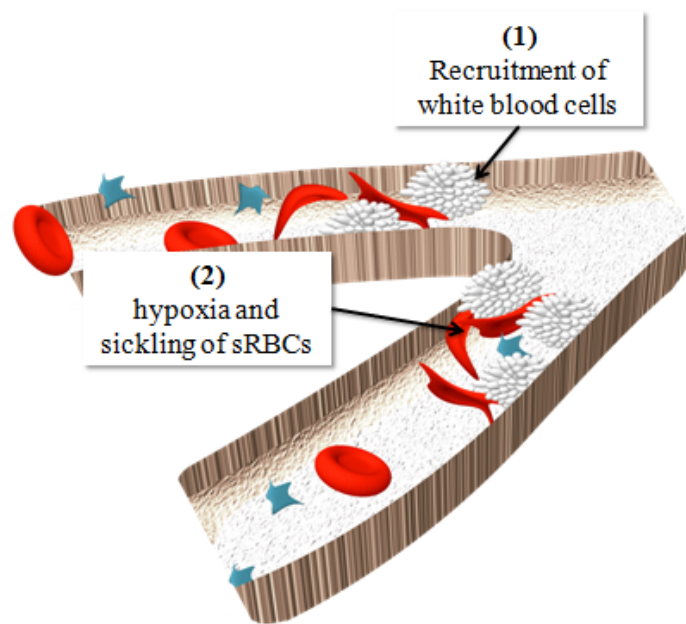


**Fig. 21:** Scenario of VO: (1) increased recruitment of white blood cells due to infections and/or pro-inflammatory state and their (2) interaction with sRBCs increasing its transient time, leading to hypoxia and sRBC sickling.



# 3 Chapter 3

## General materials and methods

### Materials and methods (english)

This chapter is dedicated to present the materials and methods used to perform my experiments.

### Matériels et méthodes (français)

Ce chapitre est dédié à la présentation du matériel et des méthodes utilisés pour réaliser mes expériences.

### Materialien und Methoden (deutsch)

Dieses Kapitel ist der Präsentation der bei meinen Experimenten verwendeten Materialien und Methoden gewidmet.

## 3.1 RBC and microfluidics preparation

### 3.1.1 Blood separation and suspending media

#### Healthy cells

Healthy blood samples were collected via finger prick from healthy donors. To remove all substances except RBCs, the samples were centrifuged at 1000 g for 3 minutes at 23°C, and the plasma and buffy coats removed by aspiration (Fig.22 schematize the different blood components after centrifugation). To wash the cells, the pellet was re-diluted in 1 ml of physiological buffer solution (PBS, phosphate buffered saline, Invitrogen, Darmstadt, Germany), centrifuged at 1000 g for 3 minutes at 23°C, and the liquid phase removed. The process is repeated twice. After the last process, the RBC pellet was re-suspended in PBS with a concentration of 1 mg/ml of bovine serum albumin (BSA, Polysciences, Warrington, USA) to preserve the biconcave shape of the RBCs [137]. PBS with this concentration of BSA was called base solution (BS). In order to mimic a suspending media with a healthy level of fibrinogen, 20 mg of dextran 70 (Sigma Aldrich, Taufkirchen, Germany) was diluted in 1 ml of BS. To mimic a suspending media with a pathological level of fibrinogen, 20 mg of dextran 150 was diluted in 1 ml of BS. These solutions were called BS+Dex70 and BS+Dex150, respectively.

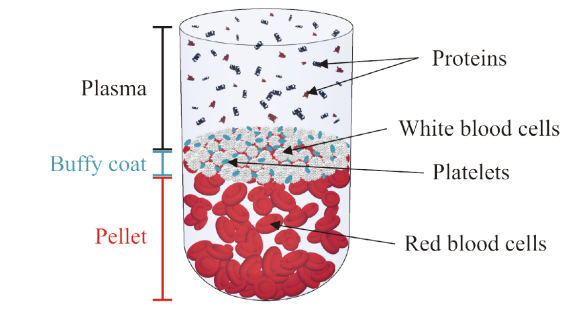


**Fig. 22:** Sketch of blood separated in different components after centrifugation. From top to bottom: plasma, buffy coat, and the RBCs pellet [1].

### Sickle cells

Sickle cells samples were provided by the Laboratoire de Biochimie et de biologie moléculaire from the Edouard Herriot Hospital in Lyon. To remove all substances except RBCs, the samples were centrifuged at 1000 g for 3 minutes at 23°C. Plasma was removed by aspiration, reserved in a plastic container, and stored at 4°C to use it as a suspending media. The buffy coat was removed by aspiration and the RBCs were washed 3 times following the same procedure described for healthy cells in the previous section.

### 3.1.2 Percoll continuous density separation

In this section, the method used to separate the RBCs accordingly to their densities is described.

A discontinuous density gradient based on Percoll was created. Percoll (P1644-500ML, Sigma Aldrich) is a media for density gradient centrifugation of cells, viruses, and subcellular particles. It is composed of colloidal silica coated with polyvinylpyrrolidone (PVP), whose diameters range from 15 to 30 nm. Percoll is non-toxic and does not adhere to membranes. It has a pH between 8.5 and 9.5 at 25°C. The density layers can be formed within the density range of 1.0 to 1.3 g/ml, being iso-osmotic throughout. To create a solution of a desire density  $d$  and 300 mOsm, it was necessary to mix Percoll, pure water, and a solution of 1.5 M of Sodium Chloride in pure water. This last solution was used to adjust the osmotic pressure. To calculate the proportion of each component, the following equation<sup>1</sup> was used:

$$V_0 = V \frac{d - 1/11 \times 1,058 - (1 - 1/11)}{1,13 - 1} \quad (8)$$

where  $V_0$  is the non-diluted percoll volume, and  $V$  the total final volume. 2 ml of each solution was created. Their density  $d$  and osmolarity were measured. With the help of a syringe pump, the layers were deposited carefully one by one in a 15 ml plastic falcon from bottom (most dense) to top (less dense). 2 ml of 50% of hematocrit in PBS was deposited at the very top of the layers. The falcon was centrifuged at 4000 g

<sup>1</sup>Cell separation media: methodology and applications, GE Healthcare, 2007

for 30 minutes at 4°C with the centrifuge set to zero deceleration. After centrifugation, different well define bands of cells of different densities were obtained as shown in Fig.23.

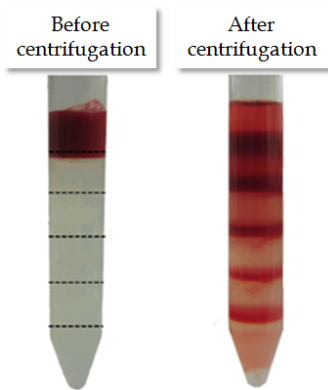


**Fig. 23:** left: 2 ml of 50% of hematocrit in PBS deposited at the very top of the percoll layers of different densities (separated by dashed lines). Right: falcon after centrifugation with different well defined bands of cells located in between the layers of different densities.

Percoll and each of the bands of RBCs were removed by aspiration. The different bands of RBCs were separated in different plastic containers and washed 3 times in PBS with 5 *mM* of glucose.

### 3.1.3 PKH 26 and 67

To label RBCs, PKH26 yellow-orange and PKH67 green Fluorescent cell linker kits for general cell membrane labeling were used (Sigma Aldrich). Each kit contains a fluorescence dye, consisting of long aliphatic tails that anchor into the lipid regions of the cell membrane [138,139], and a Diluent C solution designed to maintain cell viability, maximize dye solubility and increase staining efficiency during the labeling process [140]. Relative fluorescence intensity curves<sup>2</sup> of PKH26 and 67 are presented in Fig.24.

In the following, the protocol to label 50  $\mu$ l of RBCs is described. Any different volume of RBCs to be labeled should maintain the proportions there described.

To label 50  $\mu$ l of RBCs, the following two solutions should be mixed:

1. 10  $\mu$ l of PKH 26(67) diluted in 2.490 ml of Diluent C
2. 50  $\mu$ l of pure RBCs in 2.45 ml of Diluent C

Because staining is nearly instantaneous, rapid and homogeneous dispersion of cells in dye solution is essential for a bright, uniform and reproducible labeling. As it is recommended by the provider, the solution 1. was added to the solution 2. as fast as

<sup>2</sup>Specification Sheet PKH26(67) Fluorescent Cell Linker Kit for General Cell Membrane Labeling, Sigma Aldrich

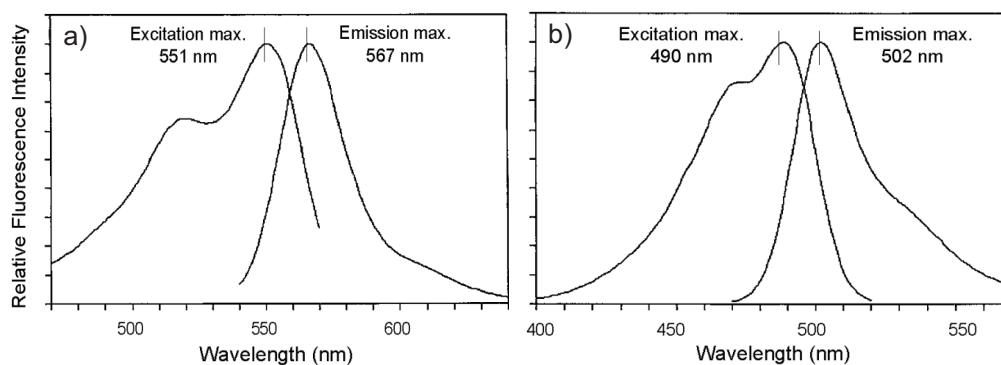


**Fig. 24:** Relative fluorescence intensity curves of PKH26 a) and 67 b) fluorescence cell linkers are presented. The maximum and the minimum wavelength of excitation and emission and their values are specified by a line on the curves.

possible (the mixture was called cell/dye solution). The cell/dye solution was incubated for 5 min (and no more) to avoid cell damage. To stop the staining, an equal volume of the total cell/dye solution of serum or complete medium with 1% of BSA was added to the cell/dye solution, and incubated for 1 minute to allow binding of the excess of dye. This last solution was changed to a new container and the cells were washed 3 times in PBS. After washing, the RBCs were re-suspended in the desired media.

### 3.1.4 PDMS chips

Polydimethylsiloxane (PDMS) is a silicon-based organic polymer known for its ability to mold and replicate features down to the nanoscale. It has excellent elastic properties, low cost, and optical transparency. It is the most widely used material in microfluidic device fabrication.

Photolithography aims at transferring a geometric pattern from a photomask to a light sensitive material such as SU-8 photoresist. It is required for fabricating a SU-8 master, that serves as a mold for pouring PDMS, enabling the replication of PDMS-based microfluidic devices.

The first step in PDMS-based microfluidics manufacturing was to have an appropriate mold. The mold used comprises of 25 parallel channels with a rectangular cross-section of  $11.9 \pm 0.3 \mu\text{m} \times 9.7 \pm 0.3 \mu\text{m}$  in width and height respectively and extra rectangular cross-section channels of approximately 20, 30 and 40  $\mu\text{m}$  to decrease the resistance in the microfluidic device. The channels had a length of approximately 4.0 cm. The next step was to mix a PDMS (Dow and Corning's Sylgard 184) base monomer with a curing agent in 10:1 mass ratio and to fill the mold with it. Bubbles appeared when the two components were stirred. To clear air bubbles, the master poured with PDMS was deposited in a desiccator connected to a vacuum line. When all bubbles were removed, the master was heating at  $75^\circ\text{C}$  for 1 h. After the heating period, the PDMS became

solid and can be peeled out of the mold. The solid PDMS contained the inverse of the original pattern embossed on the surface of the master.

In order to conduct the microfluidic device with an external reservoir, holes were punched at the entrance and outlet of the channels. The final step in the manufacturing process was to bond the PDMS to a glass slide. An exposure to the surface to be bonded to oxygen-plasma for 45 s was used in order to achieve a strong permanent bond between the glass slide and the solid PDMS. The final result of the PDMS-based microfluidic device is sketched in Fig.25.

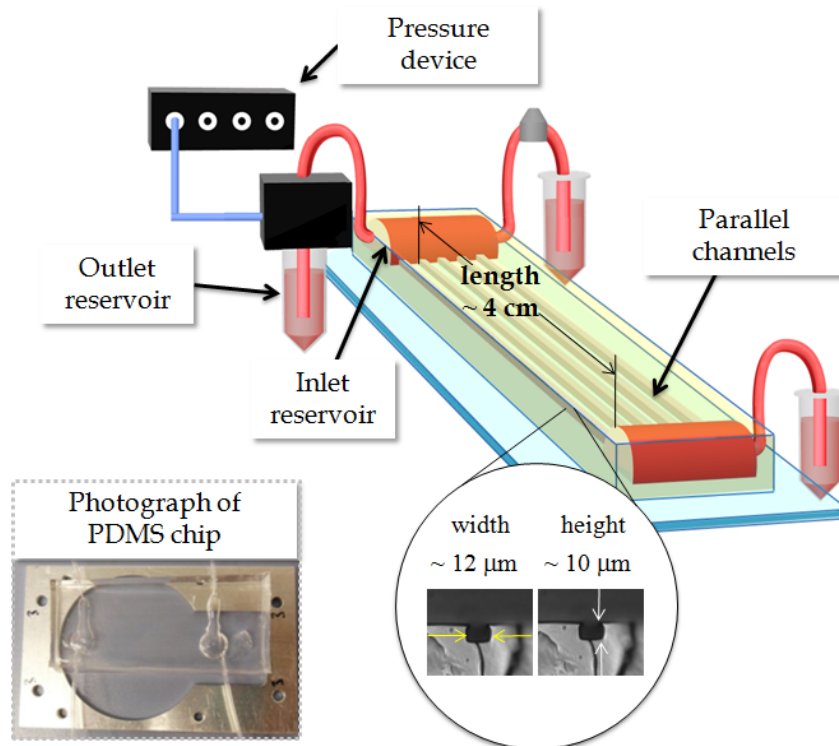


**Fig. 25:** Sketch and photograph of the PDMS-based microfluidic device.

### 3.1.5 Glass capillaries

To prepared glass capillaries-based microfluidic devices (see Fig.26), two round hollow glass capillaries (CV0508, CM Scientific) with inner and outer diameter of 50 and 80  $\mu\text{m}$ , and 50 mm in length were fixed diagonally on a clean cover glass (35 $\times$ 60 mm in length and width, respectively) by two drops of rapid-dry Epoxy. The capillaries should be fixed as near as possible from each other.

In the next step, the base of two needles (20G $\times$ 1", 0.9 $\times$ 25 mm, Terumo) were pulled until reached a height of 1 mm to be used to conduct the microfluidic device with an external reservoir. An entrance for the glass capillaries was created on the base

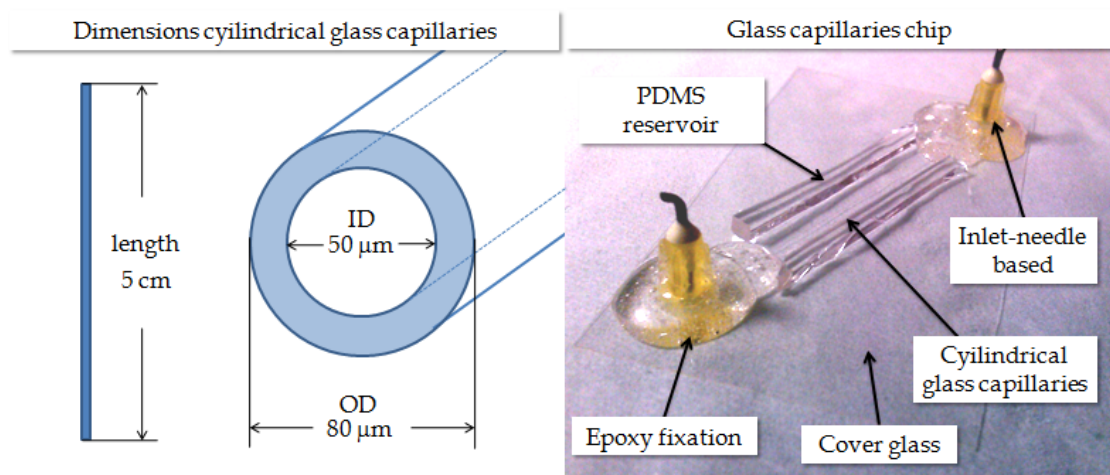


**Fig. 26:** Left: sketch of the glass capillaries dimensions and right, photograph of a glass capillaries-based microfluidic chip.

of the needles, and their tip cut and bent. The base of the needles were then fixed with epoxy to the cover glass on top of the inlet and outlet of the glass capillaries and completely sealed. The capillaries were then surrounded with liquid PDMS, that has the same refraction index than the glass capillaries. This last step was included to avoid non-desired refractions of light during observation.

## 3.2 Main devices

Images of the flowing cells were taken using an oil-immersion-objective (Nikon Corp.) with a 60 times magnification and numerical aperture of  $NA = 1.4$ . The objective is part of an inverted microscope (TE2000, Nikon). With the help of a motorized stage, different positions were able to be observed along the microchannels. A red light source was used to illuminate the samples.

Images of fluorescence membrane-labeled cells were acquired using an oil-immersion-objective (Olympus Corp.) with a 60 times magnification, installed in an inverted microscope (Olympus IX71 60, 100x objective). The images were recorded by a camera sensitive to fluorescence (Phantom miro LC310, Amatek/Vision research).

A high-precision pressure device (Elveflow, OB1, France) operating up to 2 bar to control the flow velocities was connected to an external reservoir that contained the samples. Through a polyethylene tube, the external reservoir was connected to the inlet of the microfluidic device to inject the sample into the channels.

### 3.3 Stop flow technique

A high-precision pressure device with 4 independent pressure outputs, called channels, was used to achieve the so called stop flow technique (see Fig.27). One of the channels was connected to an external reservoir (1) that contain the sample. Through a polyethylene tube, the external reservoir was connected to the inlet of a glass capillary microfluidic chip to inject the sample into the channels. This connection is called line 1. The output of the microfluidic device was at the same connected to a second external reservoir (2). Finally, the second external reservoir was connected to a different channel of the pressure device through a polyethylene tube. This connection is called line 2. The microchannels are observed under the microscope at 1 cm in distance from the entrance of the channels and the image of the cells projected to the computer.

First, the external reservoir 2 was opened and the sample flowed from the reservoir 1 to 2. When the sample reached the external reservoir 2, the system was closed and both channels in the pressure device were set to the same pressure drop. In an ideal case, the flow of cells into the channel stopped. If this was not the case, the pressure drop of the channels should be adjusted accordingly until the flow of cells was completely stopped. We called this base state. Then, a desired positive difference in pressure between channel 2 and 1 was set in order to have a flow at a define pressure drop from reservoir 1 to 2. To stop the flow, the base state should be reached again.

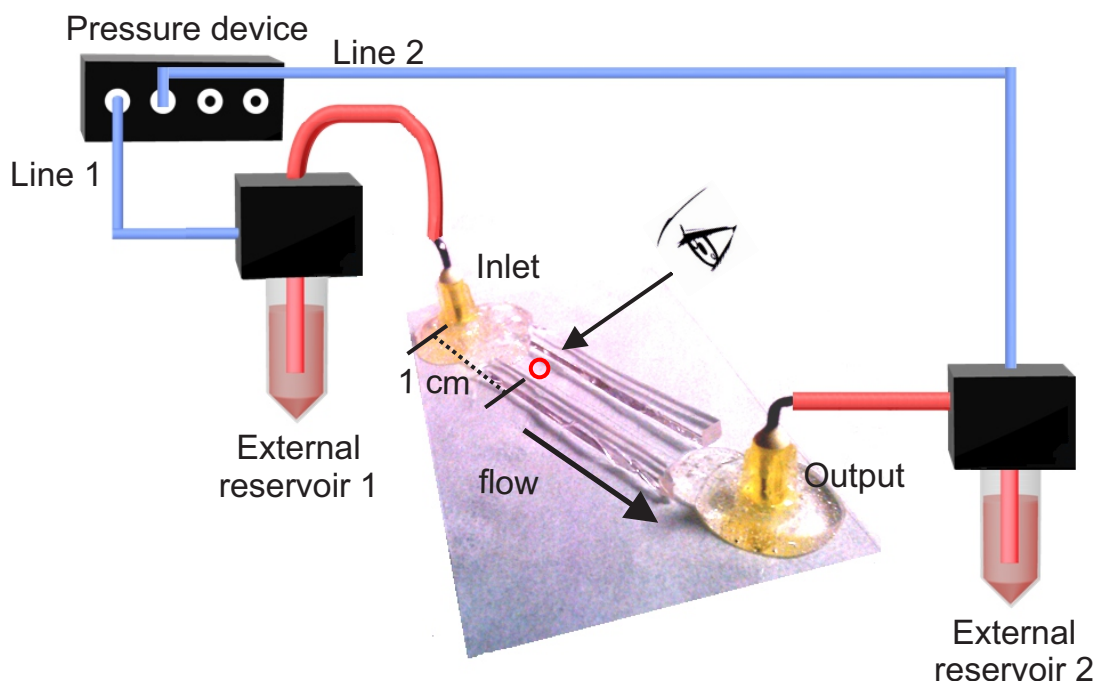


**Fig. 27:** Experimental setup for the flow stop technique.

## 3.4 Image analysis

### 3.4.1 Clustering of red blood cells

A semi-automatic Matlab R2015b routine is used to process the images. In the following, the routine is briefly explained:

1. In first place, the channels on the images were treated individually as is shown in Fig.28.

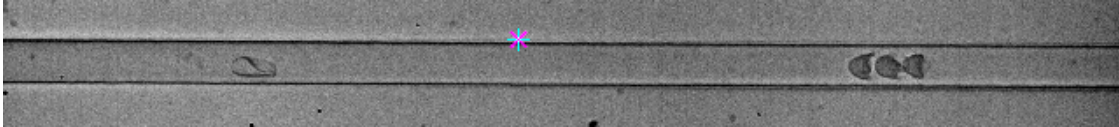


**Fig. 28:** In the image is shown how the upper border of the channel is manually marked.

2. A background image was obtained by averaging the pixel value from all the set of images recorded. The background was then subtracted to each individual frame. As an example, the image a) without background is presented in b) in Fig.29. In b), the pixel value of each column was average and as a result, a signal with bump where objects were passing (see c) in Fig.29) was obtained. The values of the signal of each frame was stored in the rows of a matrix.

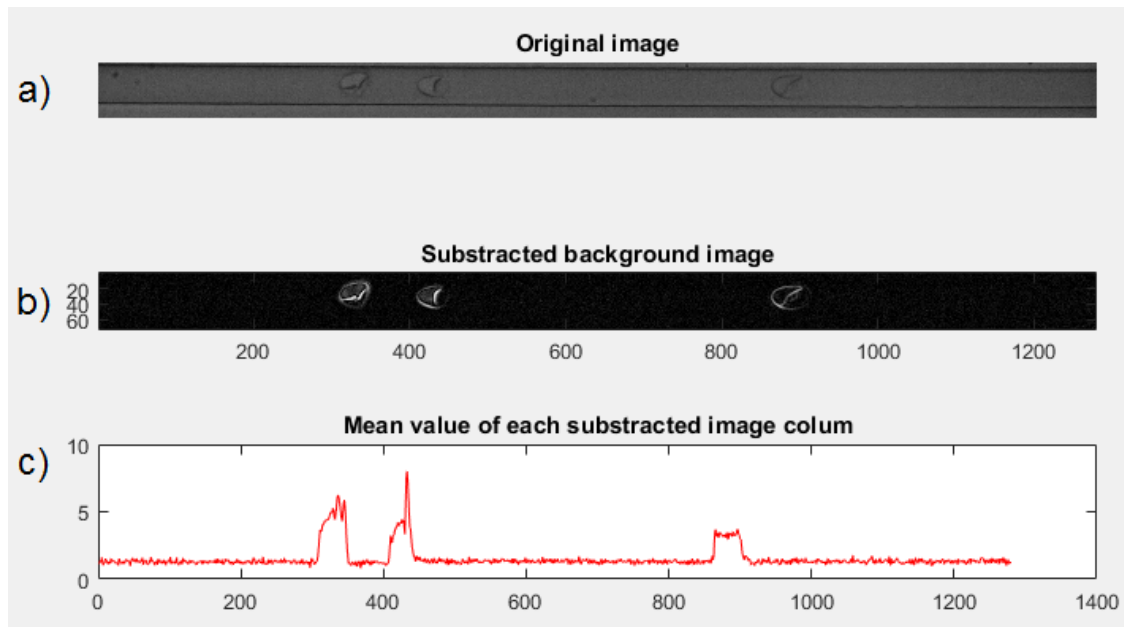


**Fig. 29:** Subtracting background of each image.

3. A cross correlation was done between two consecutive rows in the matrix. The displacements obtained by cross correlation were used to estimate the velocity of the cells (knowing the time lapsed between two frames). The average velocity  $\bar{v}_{RBC}$  of the cells of each measurement can be then obtained.
4. When the background was subtracted from each image, the grey scale was inverted, the intensity and contrast increased, the edge of the objects smoothed out, and the black regions filled in. A binarized image (objects in white and background in black) was in this way obtained. The white objects can include one or more cells.
5. The total number of cells passing through the channels in a define time lapse was used to estimated the tube hematocrit  $H_t$ . To ensure the inclusion of all objects, a manual selection of the objects was done after binarization. The number of cells inside each object was estimated by the program (see Fig.30) and manually corrected.

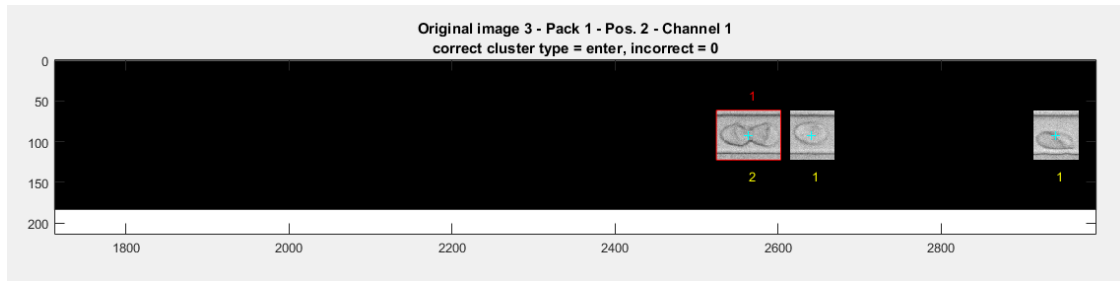


**Fig. 30:** Image showing the number of cells inside each object estimated automatically by the program. At the same time, the program is asking for a manual correction of the number of cells estimated.

When the sequence of images ends, the total number of cells  $N$  was obtained. By knowing the total number of cells  $N$ ,  $H_t$  was calculated as:

$$H_t = N \frac{V_{RBC}}{A \cdot \bar{v}_{RBC} \cdot t} \quad (9)$$

where  $V_{RBC}$  is the volume of a single cell,  $t$  is the recording time (calculated by total number of frames processed, and the frames per seconds set in the camera).

6. The upper and lower as well as the front and back borders of the cells in each object were manually selected and stored. In this way, the length  $D$  (see Fig.31) of a single cell was obtained, and the average length  $\bar{D}$  of the  $N$  cells calculated.
7.  $D/2$  was defined as the longitudinal center of each cell. The distance  $d$  between longitudinal centers of consecutive cells (see Fig.31) was automatically obtained. By definition, if  $d \leq 1.5 \cdot \bar{D}$ , the cells belonged to the same cluster. The program evaluated  $d$  and grouped the cells in clusters accordingly to the definition.

8. The length of the clusters,  $L$  (see Fig.31), was defined as the distance between the longitudinal center of the first cell and the last one in a cluster.
9. In clusters of 2 cells and more, the intercellular distance  $I$  was defined as the surface-to-surface (manually selected) intercellular distance (over the axial line) of consecutive cells. In Fig.31 this definition is sketched.

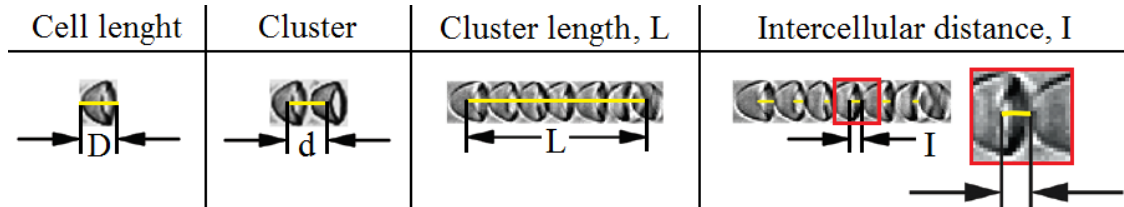


**Fig. 31:** From left to right: length  $D$  of a cell, distance  $d$  between two consecutive cells, cluster length  $L$  and surface-to-surface intercellular distance  $I$  over the axial line of consecutive cells belonging to the same cluster.

10. The spanwise position of a cell, was defined as the distance  $d_C = \frac{w}{2} - \frac{h}{2}$ , where  $w$  is the width of the channel and  $h$  is the height of the cell as it is shown in Fig.32. From this definition, the program stored the spanwise position of the individual cells.

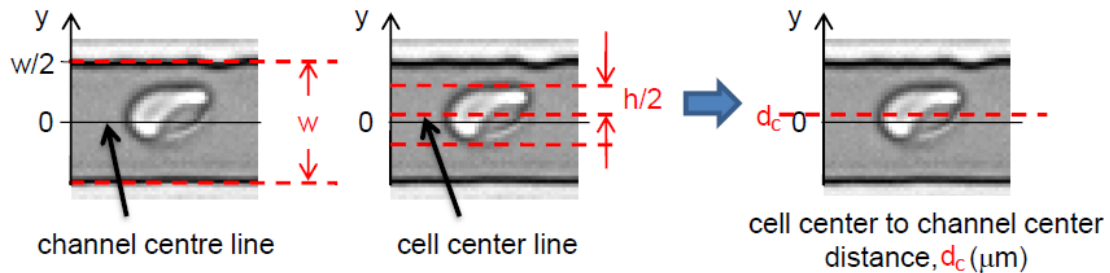


**Fig. 32:** The spanwise position of a cell  $d_C$  is sketched.  $d_C = \frac{w}{2} - \frac{h}{2}$ , where  $w$  is the width of the channel and  $h$  is the height of the cell.

11. In this further step, doublets (cluster formed by two cells) were manually classified into adhering clusters (if the adhesion between cells in the images was evident as is shown in Fig.33) or hydrodynamic in other case.
12. Finally, hydrodynamic doublets were classified by eye inspection into parachute–parachute (PP), parachute–round (PR), parachute–slipper (PS), slipper–slipper (SS) and slipper–parachute (SP) according to the shape of the front-and-back cell shape, respectively. In Fig.49, representative images of the doublet-shape classification is shown. Doublets were classified as Other if the previous classification was not appropriate.

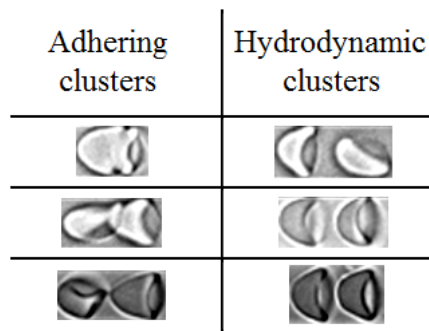


**Fig. 33:** Representative images of adhering and hydrodynamic clusters are presented.

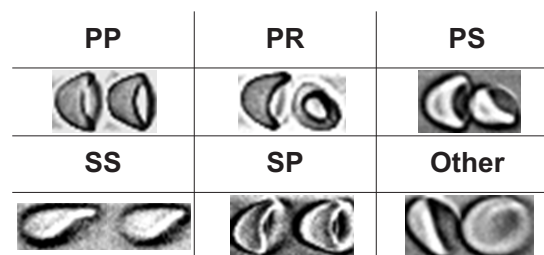


**Fig. 34:** Representative images of doublet-shape classification.

With all the previous information, statistics on different parameters can be performed.

### 3.4.2 Self-margination in sickle cell anemia

The images during the experiments were obtained by a camera connected to an Olympus IX71 60 Microscope and treated by Matlab R2015b and ImageJ 1.49v softwares. OriginPro 2016 was used for post-processing analysis. In the following, the routine is briefly explained:

#### Detection of individual cells

1. ImageJ 1.49v software was used to identify and select the position of fluorescence labeled cells on the sequence of images. The selection of the position was done on the "in focus" image of a cell. As an example, in Fig.35 is shown the focus and defocus images of a cell while moving back and forward on a sequence of images. The image nr. 5 is the "in focus" image of the cell and was selected to get the cell position. From the "in focus" image, the cell position is located in the central part of the cell and not on the edge or elsewhere. In this way, an approaching as much as possible to the center of mass of each cell was achieved.
2. After the previous step, the total  $N_L$  cell-positions were identified and the results saved.

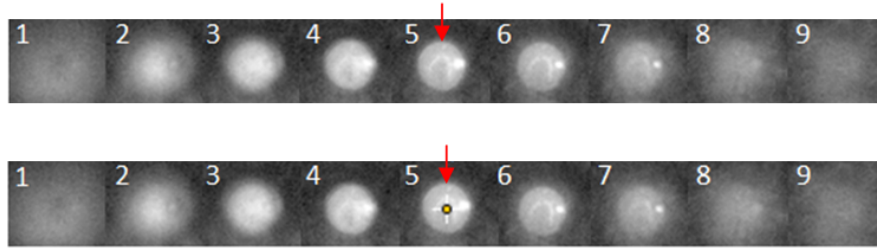


**Fig. 35:** Example of a sequence of images of the same cell. First row (from top to bottom) are images of the focus and defocus of the cell while moving back and forward on a sequence of images. The image nr. 5 is the "in focus" image of the cell. In the second row is shown the location of the cell position (yellow dot), located at the center of the cell.

3. The longitudinal middle-plane of the channels were found by eye (a), Fig.36). The origin of a coordinate system were located at the half of the middle-plane width (white dash line in Fig.36). In the same way, the bottom of the channels were identified (b) in Fig.36). Respect to the system of reference established, the  $y$  position of the cells were then obtained (c) in Fig.36).
4. A linear relationship was performed between the channel high  $h$  and the frame number  $i$ , knowing that the velocity  $v$  of the image acquisition was constant.  $h = a \cdot i + b$ , where  $a$  and  $b$  were obtained by linear fitting of experimental data. Afterwards, both, the high  $h$  and the  $y$  position of each cell, were known (see c) in Fig.36). The radial position  $r_i$  (see second column, c) in Fig.36) of each cell can be calculated.
5. A projection in a transversal plane of the positions of the cells was done. The cells detected above the middle plane were not considered (the fluorescence at this high was weak due to diffusion of light through the sample).  $n_L$  is the number of cells detected from bottom up to the middle plane, excluding the cells detected above. Their projection is shown in Fig.37.
6. Knowing the volume fraction of labeled-cells ( $1/x$ ) with respect to the total volume of RBCs,  $V$ , an estimation of the tube hematocrit can be done as follows:

$$H_t = \frac{n_L \cdot x \cdot V_{RBC}}{V_{C/2}} \quad (10)$$

where  $n_L$  is the total number of labeled-cells positioned up to the middle of the channel,  $V_{RBC}$  is the volume of a single cell and  $V_{C/2}$  is the half of the cylinder volume, whose length was obtained from the recoded images.

### Cell-free layer, CFL

The thickness  $\delta$  of the CFL is estimated as explained in the following:

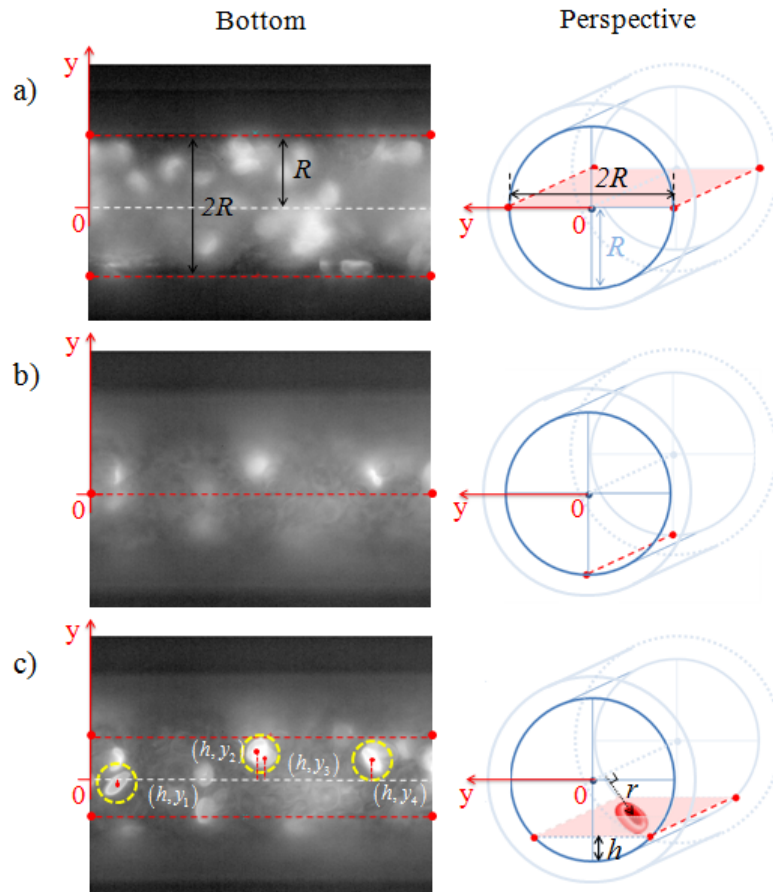


**Fig. 36:** The first column show the images of a channel and the second column sketch the cylindrical section of it. The longitudinal middle-plane of the channel is shown in a), and the channel bottom in b). The  $(h, y)$  and radial position  $r$  of the cells are shown in c).

1. Videos of the flowing cells were recorded at the middle plane of the channels. A kymogram is done for a define channel position. ImageJ software was used for this purpose.
2. A histogram of the intensity profile of each row in the kymogram was obtained (a) in Fig.38). The standard deviation of each histogram was plotted (b) in Fig.38). The maximum changes in pixel intensity were assumed to be the position of the cells border. These positions were located on the peaks of the standard deviation curves. Knowing the channel wall positions and the position of the peaks,  $\delta$  was estimated.

### Velocity profile

Using the cells as tracer particles, the instantaneous velocity profile of the flow was obtained. Particle image velocimetry (PIV) is applied between two consecutive frames using PIVlab 1.41 Matlab-App [141] (see as an example, Fig. 39). The software allows

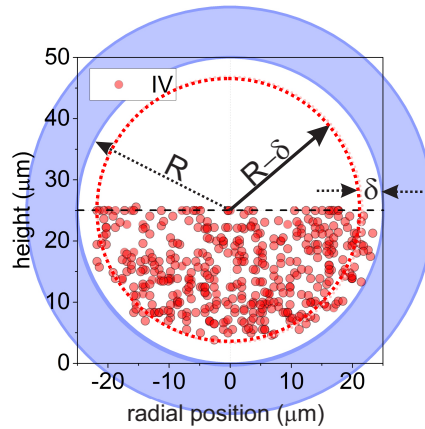


**Fig. 37:** Transversal projection of the position of the  $n_L$  cells detected in the channel (red dots). The cell-free layer (CFL) position (limit of the core where the cells flow) is located at  $R - \delta$ , where  $R$  is the tube radius and  $\delta$  the CFL thickness.

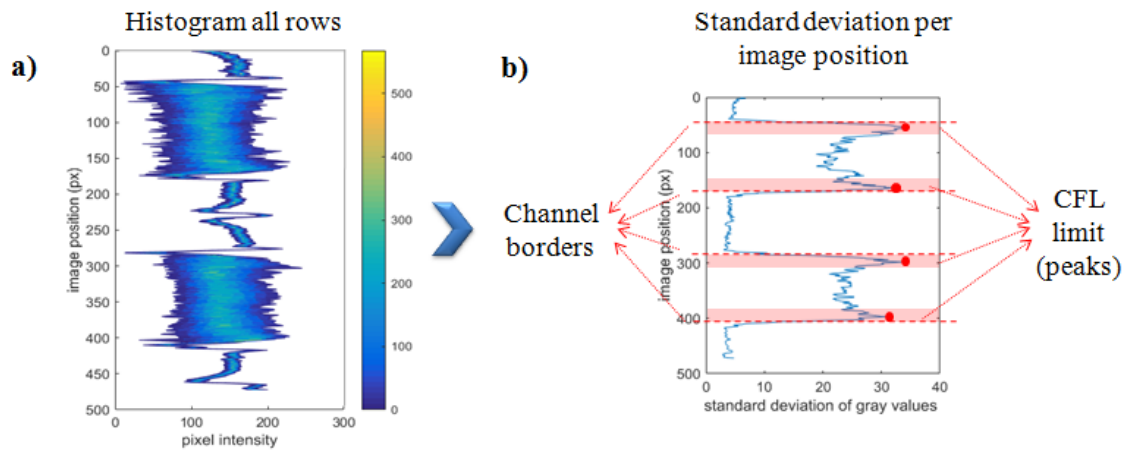


**Fig. 38:** The standard deviation of the row intensity values in b) are obtained from the histogram of the row intensity values in a). Distances from the channel borders and peaks of the standard deviation were considered as a value of the CFL for a given experimental conditions.

px/frame to mm/s calibration. As an output, profiles of the instantaneous velocity were obtained from different channel positions. The resulting profiles were approximated with a parabolic function (see Fig.40). In this way, the velocity profile, maximum flow velocity and wall shear rate were estimated.

### Cell-radial distribution

With the previous data, the radial distribution of the cells were obtained accordingly to their positions in the core of the channel where the cells flow, i.e., from the center of the channel up to the cell-free layer (CFL) position located at  $R - \delta$ , where  $R$  is the

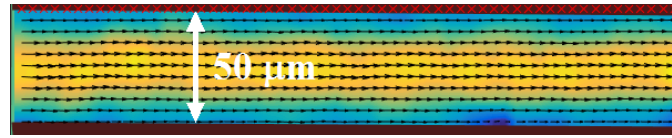


**Fig. 39:** Example of the velocity profile obtained by PIV over two consecutive images. Black arrows represent the direction and magnitude of the velocity.

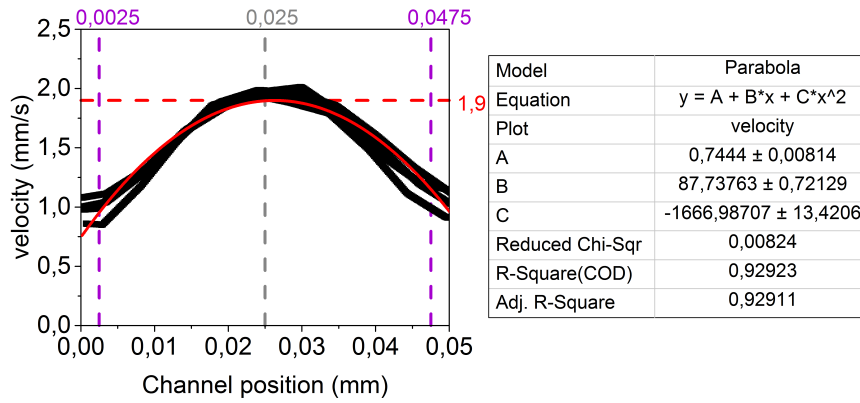


**Fig. 40:** Parabolic approximation (red continuous line) of the instantaneous velocity profiles obtained from Fig.39. As reference, dash lines have been plot: red indicates the value of the maximum velocity and purple the position of the CFL.

tube radius and  $\delta$  the CFL thickness (see Fig.37).

The cell density  $\rho$  was calculated as follows:

$$\rho = \frac{n_L}{\pi(R - \delta)^2} \quad (11)$$

The local density of particles  $\rho_l(r)$  was calculated taking into account the number of cells located on a semi-annulus area  $A$  (red area in Fig.41). The adimensional number  $\rho_l(r)/\rho$ , is defined as the variation of density of cells as a function of distance or radius  $r$  from the center of the channel.

However, to compare the distribution for different cases (for example, different pressure drops, were the thickness of the CFL changes), the radius was normalized by the  $R - \delta$  and  $\rho_l(r)/\rho$  plotted versus the normalized radius.  $r/(R - \delta) = 1$  is the outer limit of the core of the flowing cells, i.e., the (CFL) position and  $r/(R - \delta) = 0$  the center of the channel.

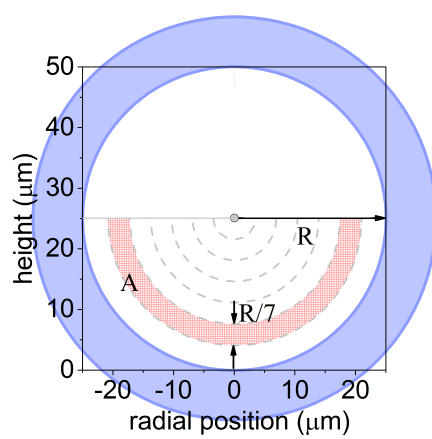


**Fig. 41:** Semi-annulus area  $A$  of the transversal cross section of the channel.

# 4 Chapter 4

---

## Cluster of cells in microcapillary flow

### 4.1 Introduction

In former studies on red blood cell (RBC) cluster formation through microcapillaries with diameters near to a red blood cell diameter at rest, either no macromolecules were added and only hydrodynamic effects were present [107], or the effects of the macromolecules were tested in channels that were smaller than the RBC diameter, with the effect of hydrodynamic attraction minimized [37]. In this study, we allow both mechanisms to take effect and we observe that both are relevant, but they form clusters of notably different geometrical forms (see Fig.14) in both, healthy and sickle cells. In this last case, the geometrical forms differs from the healthy cell and an additional cell property seems to be relevant in the cluster formation process: the adhesiveness of the cell membrane. Our two-dimensional numerical simulations predict that the flow velocity significantly affects the cluster configuration in the macromolecule case of healthy cells.

The typical adhesion energy  $\epsilon$  at healthy concentrations of fibrinogen is around  $5 \mu\text{J m}^{-2}$  [37]. In this particular study, we will mimic this condition in terms of adhesion energy and we will include an additional case with a higher adhesion energy using two dextran solutions with different molecular weights, based on data reported by Steffen et al. [36]. Even if dextran allows to mimic the typical adhesion energies, there are still many subtle differences between the effect of dextran and fibrinogen. Aggregation and disaggregation might have a different dynamic for different polymers or proteins [142] and it is also known that dextran adsorbs on the RBC surface, changing slightly its elasticity [143]. We use  $20 \text{ mg ml}^{-1}$  of dextran 70 (molecular weight of 70 kDa) to induce an interaction energy of  $\epsilon = 4.8 \mu\text{J m}^{-2}$  and  $20 \text{ mg ml}^{-1}$  of dextran 150 (molecular weight of 150 kDa) to induce an interaction energy of  $\epsilon = 12 \mu\text{J m}^{-2}$  [36] mimicking a pathological case of abnormal higher aggregation. Additionally, the interplay between different flow velocities and consequently different capillary numbers, with and without macromolecules inducing aggregation in the suspending media is also investigated.

### 4.2 Materials and experimental methods

Blood was collected from two healthy donors, washed and re-suspended in the different media. PDMS channels were build and observed under an inverted microscope. All previous was done as described in Chapter 3. The cells were injected into the PDMS

channels at three constant pressure drops  $\Delta P = (50, 100, 1000) \pm 0.5\%$  mbar and one additional pressure drop of  $20 \pm 0.5\%$  mbar for the BS (see Fig.42).

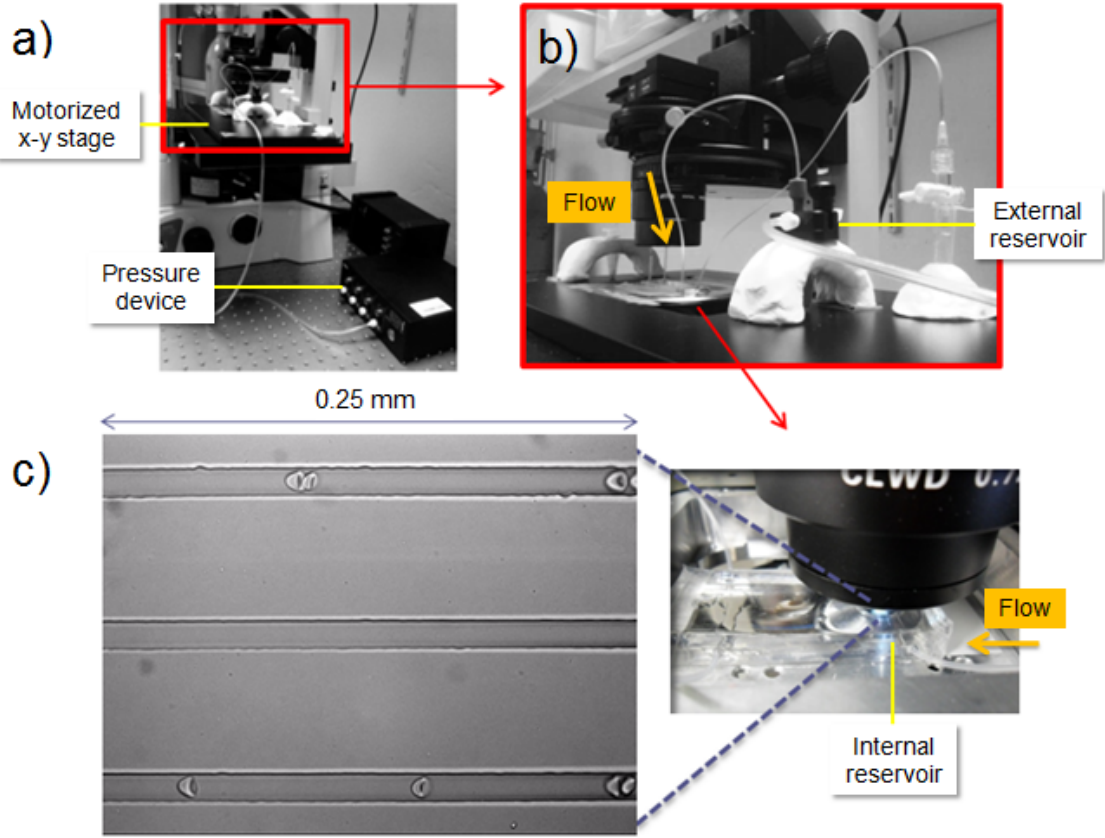


**Fig. 42:** Experimental setup. Images of the flowing cells are taken using a 60x, NA = 1.4 oil immersion objective. a) With the help of a motorized x–y stage, different positions are observed along the microchannels (see Fig.43 for details). A high-precision pressure device is connected to an external 1.5 ml reservoir that contained the sample. b) Through a polyethylene tube, the external reservoir is connected to the internal reservoir of the microfluidic device to inject the cells into the channels at different pressure drops. c) An image of the field of view of the microchannels on the computer is presented.

For rectangular channels, in the absence of cells, the maximum flow velocity  $v_{max}$  is given by [144]

$$v_{max} = \frac{4h^2\Delta P}{\pi^3\eta_{out}L} \sum_{n,odd} \frac{1}{n^3} \left[ 1 - \frac{1}{\cosh\left(\frac{n\pi w}{2h}\right)} \right] \sin\left(\frac{n\pi}{2}\right) \quad (12)$$

where  $h$ ,  $w$  and  $L$  are the channel height, width and length, respectively, and  $\eta_{out}$  is the suspending media viscosity.

For BS, BS+Dex70 and BS+Dex150 solutions,  $\eta_{out} = 1$ ,  $\eta_{out} = 1.67$  and  $1.80$  mPa·s respectively. With this values,  $v_{max}$  are calculated and summarized in Table 6. Remark

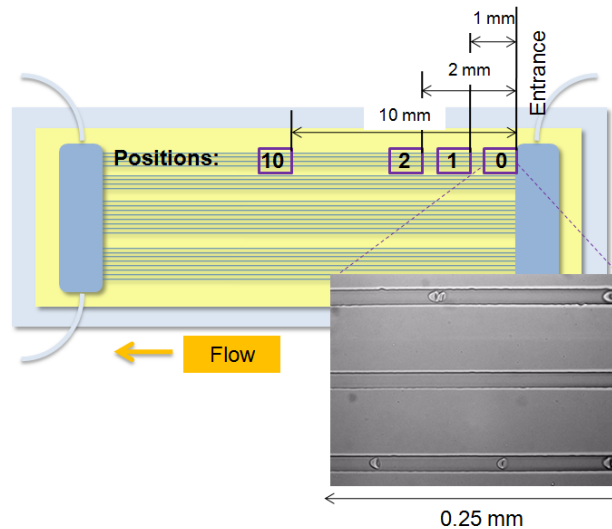


**Fig. 43:** Four different positions were observed along the channels with the help of a motorized x-y stage (see Fig.42). Each position cover a field of view of 0.25 mm in width and is located at 0 mm, 1 mm, 2 mm, and 10 mm from the entrance of the channels that are called Positions 0, 1, 2 and 10, respectively.

that the viscosity of the dextran solutions without RBCs did not show any Non-Newtonian, i.e., shear thinning behaviour in our commercial cone plate rheometer for shear rates between 10 and 1000  $s^{-1}$ .

$\Delta P$ (mbar)	$v_{max,BS}$ ( $mm s^{-1}$ )	$v_{max,BS+Dex70}$ ( $mm s^{-1}$ )	$v_{max,BS+Dex150}$ ( $mm s^{-1}$ )
20	0.41	–	–
50	1.03	0.62	0.57
100	2.07	1.24	1.15
1000	20.65	12.37	11.47

**Tab. 6:** Maximum flow velocity per solution calculated from Eq.(12) for the pressure drops used in this experiment in our rectangular cross-sectional channels.

Images of the flowing cells were taken at 30 frames per second for the lower values of the pressure drop and at 300 frames per second for a  $\Delta P = 1000$  mbar. Four different positions were observed along the channels. Each position covered a field of view of 0.25 mm in width and was located at 0 mm, 1 mm, 2 mm, and 10 mm from the entrance of the channels that were called positions 0, 1, 2 and 10, respectively. A home-made image-processing routine (for details see Chapter 3) enabled the detection of individual cells. Two cells were defined to be a part of a cluster if their center-to-center distance was smaller than or equal to 1.5 times the length of one single cell as proposed by Tomaiuolo *et al.* [102]. However, this value was heuristically selected and not based on theoretical considerations. Furthermore, as we always considered the length of the actual cell which becomes more and more elongated with the flow strength, this definition of

the length of a cluster changes with the flow strength. However, our statistical analysis below with the measured probability density functions of cluster length distribution, gives a posteriori justification of this simple definition.

## 4.3 Results and discussions

### 4.3.1 Healthy red blood cells

#### Overview

The average flow velocity of the RBC per pressure drop of each solution are presented in Table 7. Due to rouleaux formation and sedimentation of RBCs at the inlet reservoir in suspending media that included macromolecules that induced adhesion between the cells, only RBCs in BS solution were possible to flow at 20 mbar.

$\Delta P$ (mbar)	$\bar{v}_{BS}$ (mm s <sup>-1</sup> )	$\bar{v}_{BS+Dex70}$ (mm s <sup>-1</sup> )	$\bar{v}_{BS+Dex150}$ (mm s <sup>-1</sup> )
20	0.25 ± 0.01	–	–
50	0.73 ± 0.01	0.45 ± 0.01	0.35 ± 0.02
100	1.39 ± 0.08	0.92 ± 0.07	0.76 ± 0.01
1000	15.75 ± 0.5	10.47 ± 0.40	8.75 ± 0.42

**Tab. 7:** Average RBCs velocity per pressure drop and suspending media obtained by image analysis for each solution.

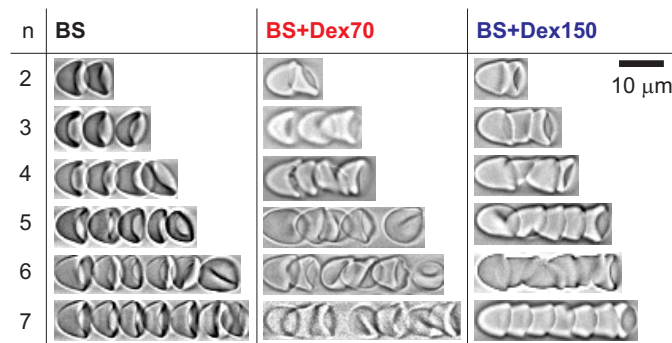
The velocity of the cells are inversely proportional to the medium viscosity. As a consequence, the capillary numbers are similar for all solutions for each pressure drop, implying a valid comparison among the different solutions for each pressure drop.

With the capillary number, the contribution of the simple shear at constant surface area and the out-of-plane bending of the membrane on RBC deformation respect to the deformation due to the stresses exerted by the flow on the cell can be compared. If we focus our attention on the values of  $Ca_S$ , we observed that up to  $\Delta P = 50$  mbar, the cell deformation is mainly affected by the simple shear strain (see Table 8) as the values are less than one. At  $\Delta P = 100$  mbar,  $Ca_S$  is near to one and the deformation could have similar contribution of the flow stress and the shear strain on the cell deformation. Finally, at  $\Delta P = 1000$  mbar,  $Ca_S$  is bigger than one and the deformation is attributed mainly to the stress that the flow exerts on the cell. Different is the case of the capillary number for bending resistance  $Ca_B$ , whose values are all bigger than one for all pressure drops. Then the bending resistance is not playing a role in the deformation of the cells at this non-local scale. Knowing this, we will refer for the different capillary numbers the pressure drop applied on the system.

$\Delta P$ (mbar)	$Ca_{S,BS}$	$Ca_{S,BS+Dex70}$	$Ca_{S,BS+Dex150}$
20	$0.100 \pm 0.004$	–	–
50	$0.292 \pm 0.004$	$0.301 \pm 0.007$	$0.252 \pm 0.014$
100	$0.556 \pm 0.032$	$0.615 \pm 0.047$	$0.547 \pm 0.007$
1000	$6.300 \pm 0.200$	$6.994 \pm 0.267$	$6.300 \pm 0.302$
	$Ca_{B,BS}$	$Ca_{B,BS+Dex70}$	$Ca_{B,BS+Dex150}$
20	$5.6 \pm 0.2$	–	–
50	$16.4 \pm 0.2$	$16.9 \pm 0.4$	$14.2 \pm 0.8$
100	$31.3 \pm 1.8$	$34.6 \pm 2.6$	$30.8 \pm 0.4$
1000	$354.4 \pm 11.3$	$393.4 \pm 15.0$	$354.4 \pm 17.0$

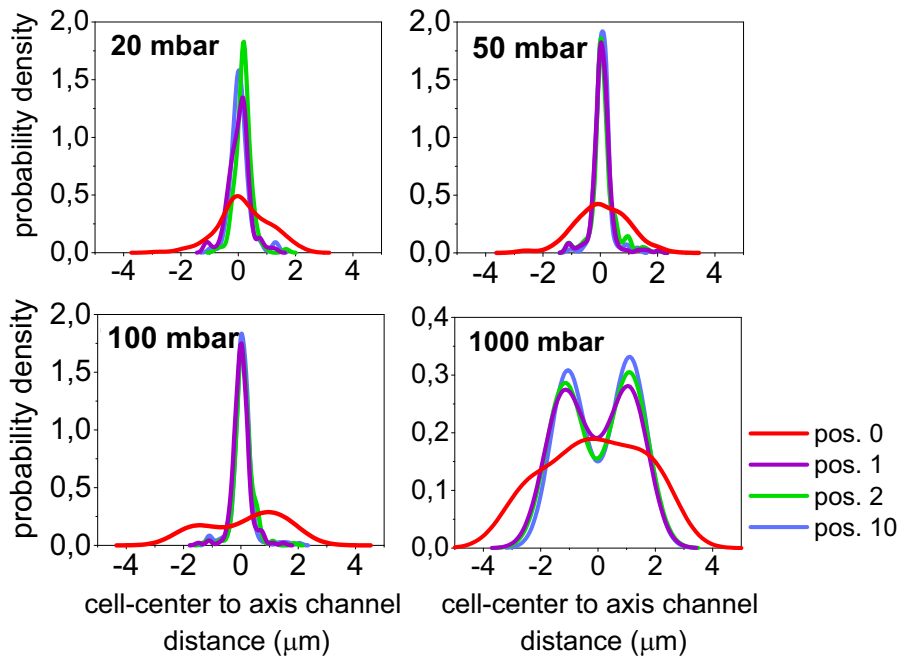
**Tab. 8:** Capillary number  $Ca_S$  and  $Ca_B$  for each pressure drop and solution.

Fig.44 shows an overview of different experimentally observed clusters type  $n$  for  $\Delta P = 100$  mbar, where  $n$  is the number of cells that belongs to the referred cluster. The shape of a RBC in a cluster formed in the BS solution is typically an axisymmetric parachute or a slipper and the cells within a cluster are clearly separated from one another. This result is different for the RBCs in the BS+Dex70 solution, where most of the cells adhere closely to their neighbors and their parachute shape is deformed. This result is even more pronounced in the case of BS+Dex150 where the cells have a bullet shape. There are no macromolecules in the BS solution, therefore, we conclude that the clusters are formed by hydrodynamic interactions only, whereas the cells in the solutions with dextran adhere closely because of the macromolecules. For the cluster  $n = 7$  in the BS+Dex70 solution (see Fig.44), as an example, it becomes apparent that this cluster may consist of two adhering cells followed by other three adhering ones. This result indicates that this cluster is an hydrodynamic cluster consisting of two macromolecule-induced clusters of 2 and 3 cells each.



**Fig. 44:** Snapshot of the typical RBC cluster configurations of type  $n$ , which contain  $n$  cells for an imposed  $\Delta P = 100$  mbar [2].

### Spanwise positions and cluster formation along the channels



**Fig. 45:** Probability density of the cell center to channel axis distance for  $\Delta P = 20, 50, 100$  and  $1000$  mbar in BS.

Before we quantify the clustering process in detail, we first characterize the spanwise position of the cells (see Chapter 3 for details). The cells enter the channels randomly, independent of the pressure drop and the solution. In Fig.45, the probability density of the cell-center to channel axis distance is plotted for the cell flow in BS solution. A centered axial alignment is observed for  $\Delta P = 20$  to  $100$  mbar from position 1 to 10. A different arrangement is observed for  $\Delta P = 1000$  mbar, where the cells tend to have a non-centered alignment with the axis of the channel located symmetrically up and above the channel axis at a distance of  $1.45 \pm 0.35 \mu\text{m}$  from position 1, and remain almost invariant until position 10. A similar behavior is observed for the macromolecule cases. This spanwise cell-positioning is apparently related to the shape of the cell that depends on the flow velocity. At smaller velocities, the cells are mainly in the axial-centered parachute configuration, but at higher velocities we found them to be in an off-centered slipper configuration predominantly.

Cluster formation in our experiment is a dynamic process and the total amount of cells of a cluster increases down the channel. To quantify this evolution, we maintained the tube hematocrit in the range of  $0.4 - 0.8\%$ , where no significant differences in cluster formation were observed, and we also determined the occurrence of clusters type  $n$  at each channel position. At  $\Delta P = 100$  mbar, most cells enter the channels as singlets ( $n = 1$ ). For the BS solution, a few clusters of type  $n = 2$  and  $3$  are observed. In the presence of macromolecules, rouleaux enter the channel and clusters of type  $n > 3$  are observed. The same behavior is observed for  $\Delta P = 50$  and  $1000$  mbar (see Fig.46). After-

wards, there is a monotonic increment in the cluster type  $n$  down the channel in all cases.

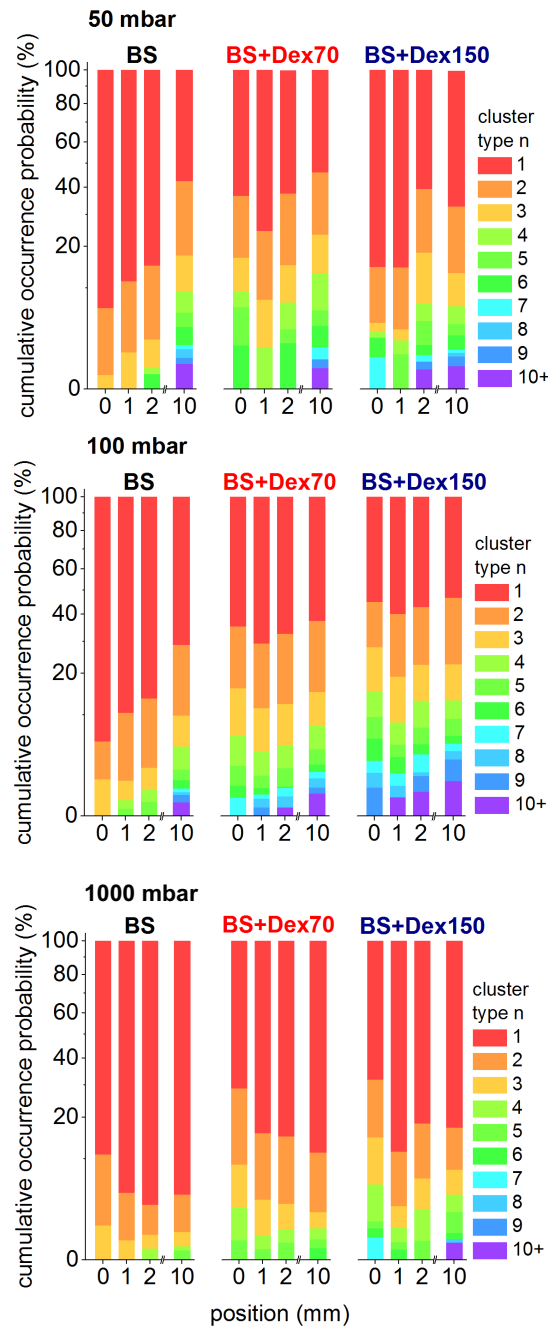


**Fig. 46:** Cumulative occurrence probability of different cluster types  $n$  per solution at four different distances from the entrance along the channel for  $\Delta P = 50, 100$  and  $1000$  mbar. Type 1 indicates single cells.

This observation in the BS solution clearly indicates that hydrodynamic interactions induce cluster formation along the channel. This conclusion is also true for the solutions

with dextran, where a few clusters appear to break up between positions 0 and 1 at first, but more clusters subsequently form down the channel. One may speculate from the larger number of the polymer-induced clusters that they should also be more robust against additional perturbations from irregularities in the flow, but this hypothesis should be verified in future studies.

Interestingly, while clusters build up progressively as the cells flow along the channel because of hydrodynamics interactions, increasing the flow strength does not intensify this phenomenon: to see that, one must compare configurations after equal residing time in the channel, e.g. position 1 at  $\Delta P = 100$  mbar (hereafter called the low stress configuration) and position 10 at  $\Delta P = 1000$  mbar (hereafter called the high stress configuration). Firstly, it is interesting to observe that, in the BS solution, the cluster size distributions are relatively close in both low and high stress configurations, as would be expected for objects of fixed shapes. This indicates that in the range of physiological velocities, flow-induced deformations of cells and the subsequent hydrodynamics interactions do not depend much on the flow stress. On the contrary, in the macromolecules cases, we observe a strong increase of the number of isolated cells between the low and the high stress configurations. This can be seen as a reminiscence of the well-known breaking of rouleaux by shear flow in unconfined configurations. Note that rouleaux remain present even in high stress configuration, although the mean shear rate is much higher than the typical shear rate of  $10 \text{ s}^{-1}$ , at which one generally considers all rouleaux broken under simple shear flow.

### Cluster length characterization

In order to go one step further in the quantification of the effect of flow on cluster formation, we need to describe more accurately those clusters.

We first quantify the differences between cluster types by their lengths, which are defined as the distance between the center of the first and last cells of the cluster (see the image at the upper left corner in Fig. 47 a)). Statistics on this length parameter as well as on the other cluster characteristics that are considered in the following are obtained by considering indiscriminately positions 1, 2 and 10.

Each data point on the graph a) in Fig.47 represents the median value  $\tilde{l}$  of the cluster length distribution by cluster type, and the error bars of their first and third quartil. If we take the case of  $\Delta P = 100$  mbar again, we observe that the length difference between the BS and BS+Dex70 (Dex150) solutions is 15% (33%), and between the two solutions with macromolecules is 16%. These length differences are significant but are a consequence of two opposite effects: the cells in the cluster in the BS solution have a parachute-like shapes, but some finite inter cell distances, whereas the cells in the solutions with macromolecules are more elongated, but closely attached to one another. This latter property becomes apparent if we look at the surface-to-surface intercellular

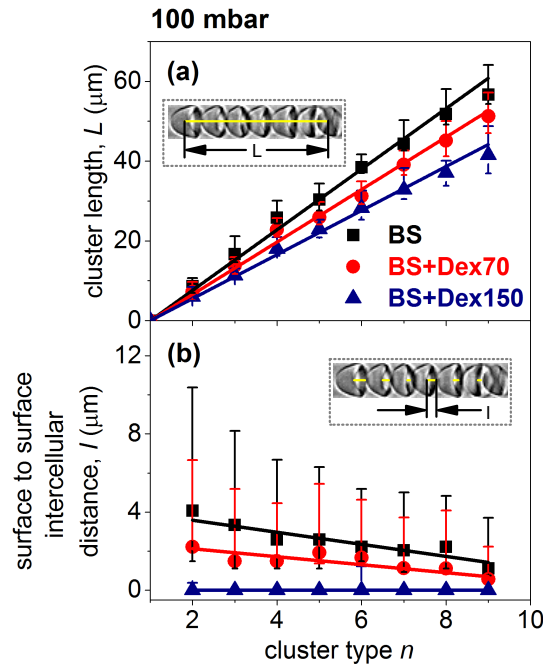


**Fig. 47:** ( $\Delta P = 100$  mbar) a) Median value  $\tilde{l}$  of the cluster length  $L$  distribution by cluster type  $n$ . The error bars are the positions of the first and third quartil. b) Median value of the surface-to-surface intercellular distance  $I$  over the axial line per cluster type  $n$ . The error bars represent the positions of the first and third quartil. Straight lines indicate linear fits.

distance  $I$  in Fig. 47 b). The distances  $I$  are asymmetrically distributed and we take the median as a representative value for  $I$  again. The 1st and 3rd quartiles of the distribution are shown as bars up and above the median value on the graph. We found that for the surface-to-surface intercellular distance in the BS solution, the distance starts from  $I = 4.1^{+6.3}_{-2.6} \mu\text{m}$  for the cluster type  $n = 2$  and  $I = 2.2^{+4.4}_{-0.0} \mu\text{m}$  in BS+Dex70, which decreases in both cases for larger cluster types. In comparison, it is practically zero in BS+Dex150 with  $I = 0.00^{+0.4}_{-0.0} \mu\text{m}$  for the cluster type  $n = 2$  and remain similar for larger cluster types. This result indicates that the clusters in the BS+Dex70 solution are often a mixture of hydrodynamic and macromolecule-induced clusters. Additionally we present in Table 9 the median  $\tilde{l}$  and the first and the third quartil of the cluster length distribution per pressure drop for the cluster type  $n = 2, 3$  and  $4$ , which are clusters of the most frequent occurrence for the pressure drops studied. The median value  $\tilde{l}$  of the cluster length  $L$  increases with pressure drop due to the larger deformation of the cells at larger velocities.

### Separating hydrodynamic and macromolecule induced clusters

As mentioned, clusters in macromolecule solutions are a mixture of hydrodynamic and macromolecule-induced clusters. To quantify its occurrence, we focus our analysis on the clusters type  $n = 2$ , as this cluster type has the highest cluster occurrence in comparison

$\Delta P$ (mbar)	$\tilde{l}_{n=2}$ ( $\mu\text{m}$ )	$q_2^-$ ( $\mu\text{m}$ )	$q_2^+$ ( $\mu\text{m}$ )	$\tilde{l}_{n=3}$ ( $\mu\text{m}$ )	$q_3^-$ ( $\mu\text{m}$ )	$q_3^+$ ( $\mu\text{m}$ )	$\tilde{l}_{n=4}$ ( $\mu\text{m}$ )	$q_4^-$ ( $\mu\text{m}$ )	$q_4^+$ ( $\mu\text{m}$ )
BS									
20	7.96	1.76	1.48	15.00	3.52	2.59	21.85	4.07	3.33
50	8.15	1.48	1.11	15.59	1.39	1.57	23.70	1.67	2.69
100	8.61	2.07	1.65	16.66	4.54	2.04	25.78	4.28	1.44
1000	11.11	3.15	1.85	19.48	3.15	3.33	28.00	4.63	4.63
BS+Dex70									
50	5.85	2.04	2.22	10.78	3.52	2.59	19.26	5.37	4.82
100	7.24	2.44	2.14	13.73	2.22	2.04	22.78	2.89	1.78
1000	10.26	2.78	1.11	18.43	4.63	3.80	26.96	2.65	6.05
BS+Dex150									
50	4.44	1.86	0.64	8.80	1.29	1.30	12.41	2.03	0.74
100	6.03	2.41	1.29	11.37	1.67	1.11	18.00	2.89	1.78
1000	9.44	2.41	1.29	16.48	3.15	1.66	25.19	5.00	3.52

**Tab. 9:** Median value  $\tilde{l}$  of the cluster type  $n = 2, 3$  and  $4$  length distribution for each pressure drop per solution.  $q_i^-$  and  $q_i^+$  are the first and 3rd quartil of the length distribution per cluster type.

to other cluster types (see Fig.46). A hydrodynamic cluster type  $n = 2$  is defined as a cluster with a non-zero intercellular distance between the component cells, while macromolecule-induced or adhering cluster is defined as a cluster with close to zero intercellular distance between the cells. Then, a relative occurrence of hydrodynamic and adhering clusters can be quantified among type  $n = 2$  clusters. As an example, we show in Fig.48 the plot of the occurrence of hydrodynamic and adhering clusters for the cluster type  $n = 2$  in BS+Dex70 and BS+Dex150 solutions flowing at a pressure drop  $\Delta P = 100$  mbar, as a function of cluster length.

We then classify the hydrodynamic cluster type  $n = 2$  by visual inspection according to the shape of the front-and-back cell belonging to the cluster with parachute-parachute (PP), parachute-round (PR), parachute-slipper (PS), slipper-slipper (SS), slipper-parachute (SP) and other, if the previous classification was not appropriate. Fig. 34 in Chapter 3 shows representative images of the cluster classification.

Hydrodynamic clusters of type  $n = 2$  were classified accordingly in each solution. From these cluster shape classifications, it is now possible to infer the typical cluster configuration for each median cluster length in Table 9 for  $n = 2$ . For  $\Delta P = 50$  mbar, the typical BS cluster configuration is PP, and adhering clusters for BS+Dex70 and BS+Dex150 solutions. When  $\Delta P$  is increased to 100 mbar, the typical BS cluster configuration remains PP, and only in BS+Dex150 solution does the cluster configuration remain adhering. In contrast, the main configuration is now PS in BS+Dex70 solution. Remarkably, at  $\Delta P = 1000$  mbar the main cluster configuration is SS, independent

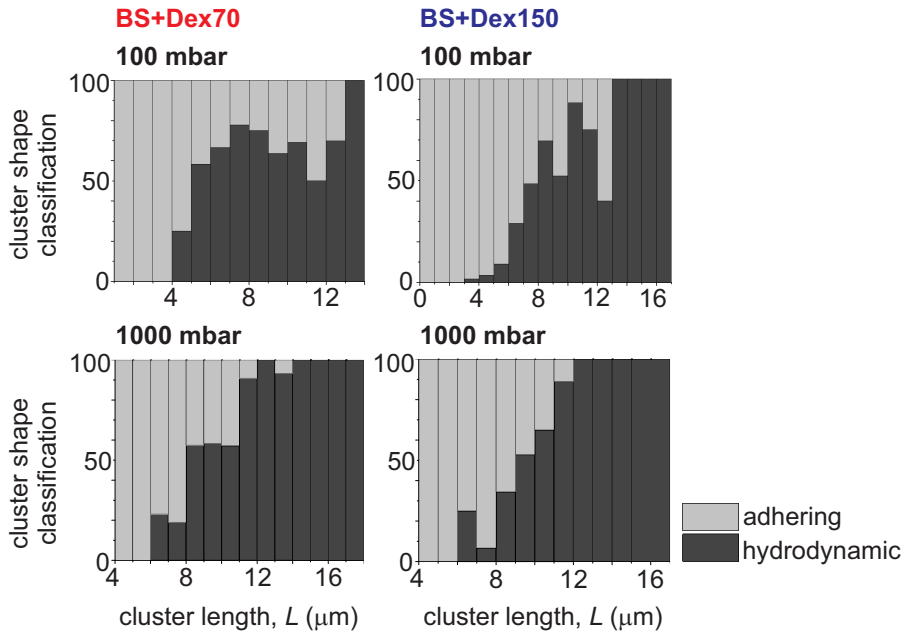


**Fig. 48:** Percentage of the hydrodynamic and adhering cluster type  $n = 2$  occurrence per cluster length in BS+Dex70 (left) and BS+Dex150 (right) solutions flowing at a pressure drop of  $\Delta P = 100$  mbar.

of the solution. This result is summarized in Fig.49, where an image of typical cell configuration per pressure drop with different solutions is presented.

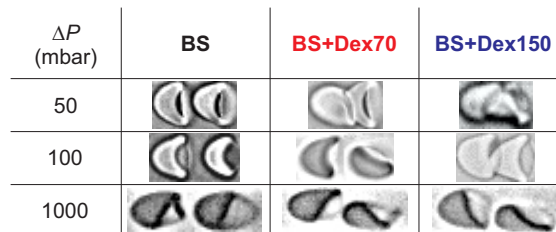


**Fig. 49:** Photographs of the typical cluster configuration as a function of the pressure drop and solution for the median value  $\tilde{l}$  of the cluster type  $n = 2$  length distribution presented in table 9.

These observations confirm that, while hydrodynamic interactions tend to create the so-called hydrodynamic clusters, and perhaps clusters where cells are so close that they would eventually collapse onto a macromolecules induced cluster, they do not succeed in counterbalancing the breaking of macromolecules induced clusters by flow stress: in the BS+Dex70 solution (resp. BS+Dex150) the occurrence of hydrodynamic clusters rises from 41% to 59% (resp. 29% to 55%) when  $\Delta P$  is changed from 50 mbar to 1000 mbar.

### Probability density functions of the cluster length

After we have clearly separated the effect of hydrodynamic and macromolecule induced clusters, we can finally present a noteworthy result for the pure hydrodynamic clusters that was obtained by evaluating the probability density function of the cluster length  $L$  of cluster type  $n = 2$  (Fig. 50). The results in BS solution show that, for  $\Delta P = 20$  mbar, there is a preferential position for the cluster length at  $7.96^{+1.76}_{-1.48}$   $\mu\text{m}$ . When we increase  $\Delta P$  to 50 mbar, the cell-to-cell distances in the BS solution start to be bimodally distributed: a pronounced peak for (short) distances comparable to the  $\Delta P = 20$  mbar that is observed experimentally, but also a populated position for large distances appears in the form of a shoulder on the right-hand side of the graph (see Fig.50). This bimodal distribution is enhanced when we increase the  $\Delta P$  to 100 mbar, where less clusters has a short cell-to-cell distance, but more are found to have a larger distance between them. Finally, if we increase the pressure drop to 1000 mbar, not only this behavior persists, but the cluster length is also shifted to higher values. The positions of the peaks of these bimodal distributions are found by fitting a double-peak function (the sum of two bi-gaussian functions) on the cluster length distribution.

In the case of solutions with macromolecules, it is possible to determine the probability density function of the cluster length  $L$  for the hydrodynamic clusters only, as it is shown in Fig .51. The probability density of the cluster length  $L$  of the BS+Dex70 and BS+Dex150 solutions are very similar to the probability density of the pure hydrodynamic clusters formed in BS solutions (upper graph, Fig. 50). Cell-to-cell distances in these cases are also bimodally distributed and again, a pronounced peak for short distances is observed, except in the length distribution at  $\Delta P = 50$  mbar in BS+Dex150 solution, where a high population of clusters with a short cluster length were adhering (lower graph, Fig. 50). This illustrates the subtle imbrication of hydrodynamics effects and short range adhesion forces, the former acting as a precursor mechanism for bringing the cells close enough for adhesion to occur, unless shear stress overcomes this process.

The positions of the peaks of the double-peak approximating function of the hydrodynamic cluster length distribution in Fig.50, upper graph (BS) and Fig.51 are presented in Table 10.

The hydrodynamic clusters of the cluster type  $n = 2$  in BS solution were classified according to their length, following the shape classification of Fig. 34. The resulting cluster-shape classification are presented in Fig. 49.

For lower pressure drop ( $\Delta P = 20$  mbar), the cells are mainly in a rather undefined configuration and are classified as Other. However, in the peak zone (cluster length  $L = 6.61^{+3.47}_{-1.64}$   $\mu\text{m}$ , see Fig.34), PP clusters are observed. When we increase the pressure drop to 50 mbar, the peak 1 (cluster length  $L = 7.67^{+1.52}_{-1.37}$   $\mu\text{m}$ ) of the bimodal distribution is now highly populated by PP clusters (52% of the cluster configurations) and peak 2 (cluster length  $L = 11.56^{+1.64}_{-1.61}$   $\mu\text{m}$ ) is populated mainly by PS configurations (40%). At

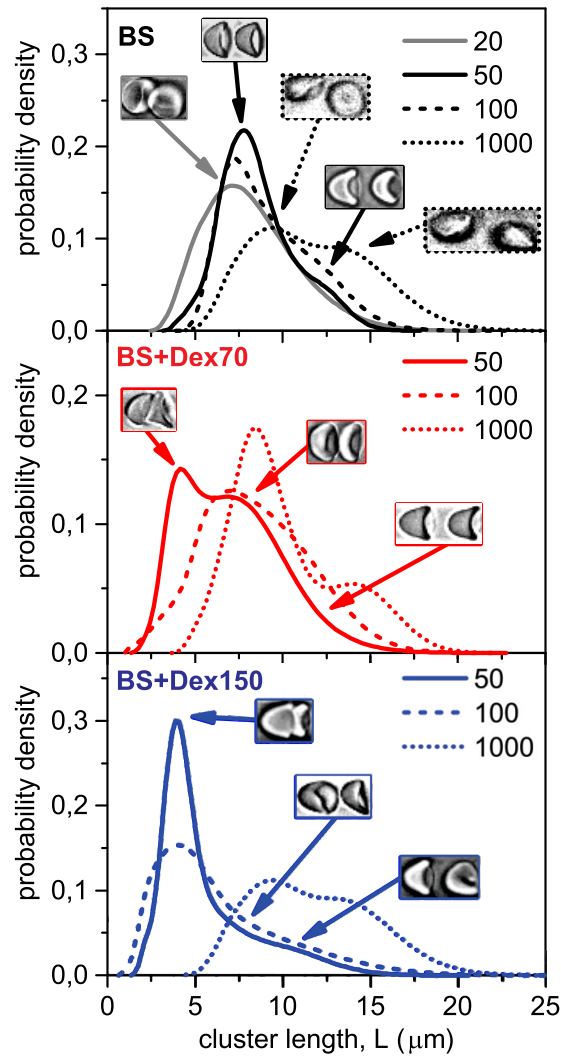


**Fig. 50:** Probability density of the characteristic cluster length  $L$  of the cluster type  $n = 2$  for BS, BS+Dex70 and BS+Dex150 solutions. The photographs are representative snapshots of the most frequent cluster configurations with the cluster length position indicated by the arrows between the photographs and the graph lines.

$\Delta P = 100$  mbar an even bigger population of PP (66% of the clusters) are present for peak 1 (cluster length  $L = 6.98^{+1.48}_{-0.93}$   $\mu\text{m}$ ), while for peak 2 (cluster length  $L = 10.43^{+2.63}_{-1.75}$   $\mu\text{m}$ ) PP (36%) and PS (32%) have a similar frequency of occurrence. For the largest pressure drop ( $\Delta P = 1000$  mbar) the occurrences are significantly different. Here, the preferred configuration is mostly SS with a 89% occurrence around the peak 2 (cluster length  $L = 13.44^{+2.92}_{-2.94}$   $\mu\text{m}$ ), but only 14% around peak 1 (cluster length  $L = 8.4^{+2.04}_{-1.47}$   $\mu\text{m}$ ), and 71% are classified as other. Evidently, the PP configuration is related to smaller velocities and axial cell migration (see Fig. 45), while the SS configuration appears at larger velocities and is related to the cell location between the channel axis and the channel wall.

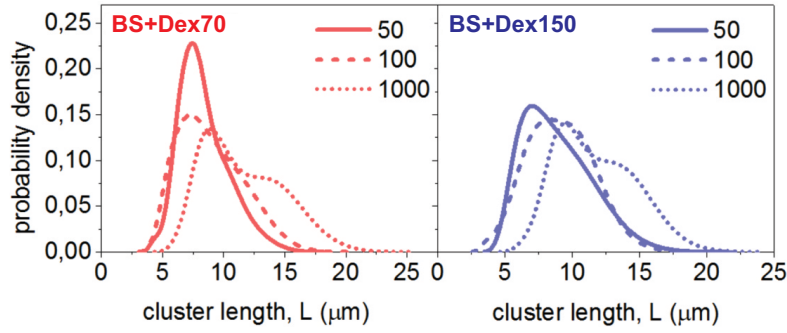


**Fig. 51:** Probability density of the cluster length distributions for the pure hydrodynamic clusters type  $n = 2$  in the macromolecule solutions BS+Dex70 (left) and BS+Dex150 (right).

$\Delta P$ (mbar)	peak 1			peak 2		
	$L_1$ ( $\mu\text{m}$ )	$w_1^-$ ( $\mu\text{m}$ )	$w_1^+$ ( $\mu\text{m}$ )	$L_2$ ( $\mu\text{m}$ )	$w_2^-$ ( $\mu\text{m}$ )	$w_2^+$ ( $\mu\text{m}$ )
	BS			BS		
20	6.61	1.64	3.47	-	-	-
50	7.67	1.37	1.52	11.56	1.61	1.64
100	6.98	0.93	1.48	10.43	1.75	2.63
1000	8.4	1.47	2.04	13.44	2.94	2.92
	BS+Dex70			BS+Dex70		
50	7.00	0.94	1.72	10.69	3.06	1.70
100	6.72	1.33	1.68	10.14	1.62	2.77
1000	8.56	1.27	1.76	13.51	2.59	2.96
	BS+Dex150			BS+Dex150		
50	6.52	1.03	2.92	11.26	2.14	2.41
100	7.30	1.62	1.66	10.46	1.59	1.96
1000	9.46	1.49	1.80	13.54	1.41	2.55

**Tab. 10:** Characteristic lengths of the hydrodynamic cluster type  $n = 2$ . The length distributions are fitted with a double-peak function composed of two bi-gaussian distribution of center  $L_i$ , and left and right standard deviation  $w_i^-$  and  $w_i^+$ .

A comparable bimodal distribution for hydrodynamic clusters in a confined flow has been observed in a three-dimensional numerical simulation [106]. It was shown that the cell-to-cell distances strongly depended on the RBC shapes, and even a dynamic transition was reported between the two different cell-to-cell distances because of the flow coupling with the cell shapes. Our experiments do not resolve the temporal dynamic of the cluster formation process, but it is known that the cell shapes also depend on their physical parameters.

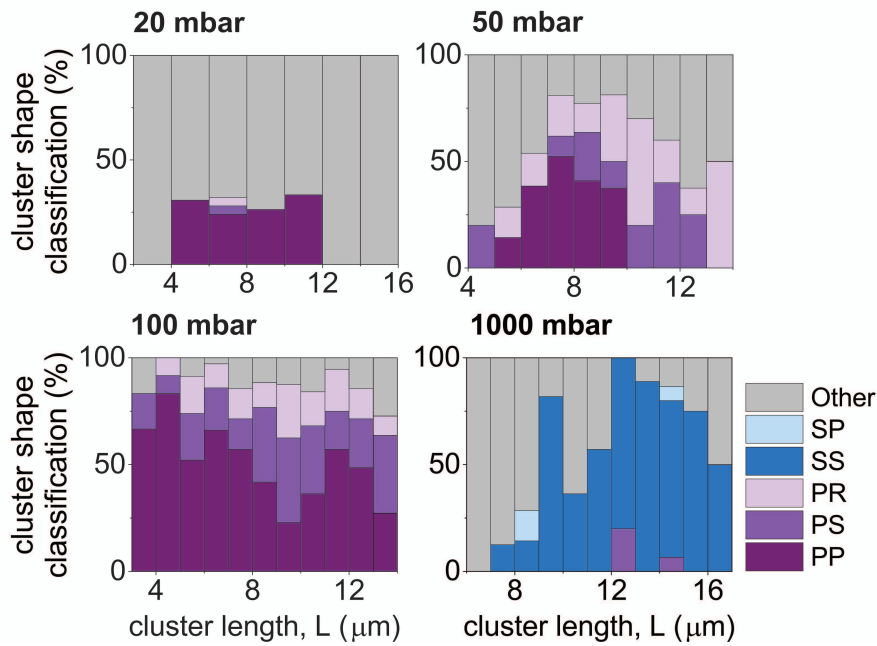


**Fig. 52:** Percentage of the different shapes of clusters of type  $n = 2$  (see Fig.49) per cluster length (BS solution).

### 4.3.2 Numerical simulations

Numerical simulations were performed by O. Aouane, at this time PhD student in the group of AG Wagner. He took the surface energy between two cells directly from the single cell force spectroscopy measurements [36, 37]. In order to reproduce a cell surface to cell surface distance comparable to the 25 nm that have been reported in the literature for adhering RBCs at rest in Dex70 solution [145], but to keep the effort due to finite numerical resolution limited, a zero force distance  $r = \sigma \cdot 2^{1/6} = 480$  nm is chosen which is still below the optical resolution in the experiments.

To verify the effect of the hydrodynamic interaction compared to the macromolecule-induced aggregation, two-dimensional numerical simulations for six different maximum centerline flow velocities of the undisturbed Poiseuille flow are done. Two vesicles with a radius of  $3 \mu\text{m}$  and a reduced area of  $\tau = 0.65$  are considered. The vesicles are suspended in a Poiseuille flow between two parallel walls with a distance of  $12 \mu\text{m}$  at low Reynolds number. The physical parameters of the RBC are first selected such that the bending rigidity is  $\kappa = 4 \times 10^{-19}$  J and the inner viscosity is  $\eta_i = 5$  mPas at  $37^\circ\text{C}$ .

The effect of the macromolecules is mimicked by an inter-cellular interaction force derived from a Lennard-Jones potential with interaction energies  $\epsilon_{Dex70} = 4.8 \mu\text{J m}^{-2}$  for the BS+Dex70 solution, and  $\epsilon_{Dex150} = 12 \mu\text{J m}^{-2}$  for the BS+Dex150 solution [36]. The simulations reproduce the effect of an additional interaction energy (adhesion energy between cells) in the cluster formation (see Fig. 53). Notable for the case of strong

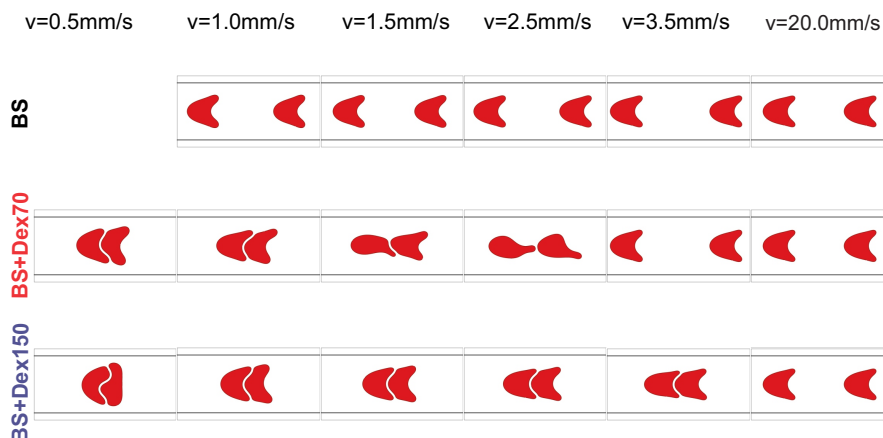


**Fig. 53:** Numerically obtained stationary shapes of cluster type  $n = 2$  at different maximum centerline flow velocities for different solutions.

adhesions (BS+Dex150 solution): the cells stick close to one another and share a significant part of their membranes in the interaction area. The interaction area depends strongly on the flow velocity, which decreases when the flow velocity increases. For the case of intermediate interaction energies (BS+Dex70 solution), the two cells stick close to one another and share part of their membranes only at low velocities (in the simulations up to  $v = 2.5 \text{ mm s}^{-1}$ ). At higher velocities, the cells are detached and flow separately in a hydrodynamic cluster configuration, even at flow velocities of  $v = 20.0 \text{ mm s}^{-1}$ . In a pure hydrodynamic flow with zero adhesion energy between the cells (BS solution), the cells flow separately, independent of the velocity with a non-zero inter-cellular distance between the cell surfaces.

Here we have to mention that in the numerical study the definition of a hydrodynamical cluster differs from the experimental results. The numerical simulation allows placing two vesicles at almost arbitrary (if not too far) distances and they always reach their shown stable inter-cellular distance. This means that cells that are placed closer to each other repel and if placed further away they attract, yielding a kind of an effective hydrodynamic interaction potential. In this way we find hydrodynamical induced clusters for all flow rates for the BS solution, but we also find that in the numerical simulations the polymer induced adhering clusters should become unstable at flow rates of 3.5 mm for the BS+Dex70 and 20 mm for the BS+Dex150 solutions. This is at least in qualitative agreement with our statistics on the occurrence of cluster types (Fig.46) where we find that at larger flow rates the percentage of hydrodynamic (non-adhering) clusters increases.

Our simulations reproduce the effect of macromolecule induced clusters in an almost quantitative manner, and we also find stable hydrodynamic clusters. However, the shape configurations at larger velocities are not well reproduced and we therefore concentrate on the experimental results for the analysis of the hydrodynamic induced clusters.

### 4.3.3 Sickle red blood cells

#### Introduction

Our study on clustering process with healthy cells shows that the flow of soft deformable objects that interact either via hydrodynamic or via polymer induced forces leads to a complex clustering scenario. It is the pronounced flow-structure or rather the flow-shape coupling that is responsible for this rich dynamics.

Some recent and notably detailed numerical predictions that soft objects should have a much stronger tendency to form clusters and obey an elaborated dynamics than hard systems [100]. Knowing that sickle cells are stiffer than healthy cells, in this second part we explore the cluster formation of sickle cells in a first approach: a oxygenated scenario. In this context the problem is already complex as sickle cells not only have different rigidity than healthy cells, but their membrane are more adhesive and the shape population is heterogeneous as irreversible flat-stiff cells different than discocyte are also present.

#### 4.3.4 Materials and experimental methods

Sickle cells samples were provided by the Laboratoire de Biochimie et de biologie moléculaire from the Edouard Herriot Hospital in Lyon, washed and re-suspended in the different media. PDMS channels were built and observed under an inverted microscope. All previous was done as described in Chapter 3. The cells were injected the cells into the PDMS channels at three constant pressure drops  $\Delta P = (50, 100, 1000) \pm 0.5\%$  mbar.

#### 4.3.5 Results and discussions

The average flow velocity of the sickle red blood cells per pressure drop of each solution are presented in Table 11.

$\Delta P$ (mbar)	$\bar{v}_{BS}$ (mm s <sup>-1</sup> )	$\bar{v}_{BS+Dee70}$ (mm s <sup>-1</sup> )
50	0.43 ± 0.01	0.37 ± 0.01
100	0.93 ± 0.02	0.80 ± 0.03
1000	10.00 ± 0.17	8.10 ± 0.31

**Tab. 11:** Average sRBCs velocity per pressure drop and suspending media obtained by image analysis for each solution.

The mean velocities of sRBCs are about 35% lower than the mean velocity of healthy RBCs flowing under the same conditions (see Table 7 and 11 to compare both mean cell velocity of healthy RBC and sRBCs, respectively). sRBCs are in general slower than healthy RBCs, highlighting the bad consequences of impaired sRBC rheology (mainly

differences among sRBCs in their density, rigidity, and viscosity) on the flow dynamics. This fact may have strong microcirculator/physiological impacts since the transient time flowing through capillaries increases compared with healthy RBCs, which implies that sRBCs can interchange more oxygen with the tissues involving the promotion of the formation of polymers inside the cells, their increase in rigidity, and their possible stack into the capillaries. However, polymer formation have been investigated mainly at resting conditions. The high deformation of cells travelling within these constricted capillaries and their complex dynamics can play a role in the polymer formation inside the cells. Further investigations will be necessary to explore the polymer formation of cells traveling through constricted channels under hypoxia (low level of oxygen) conditions.

### Spanwise positions and cluster formation along the channels

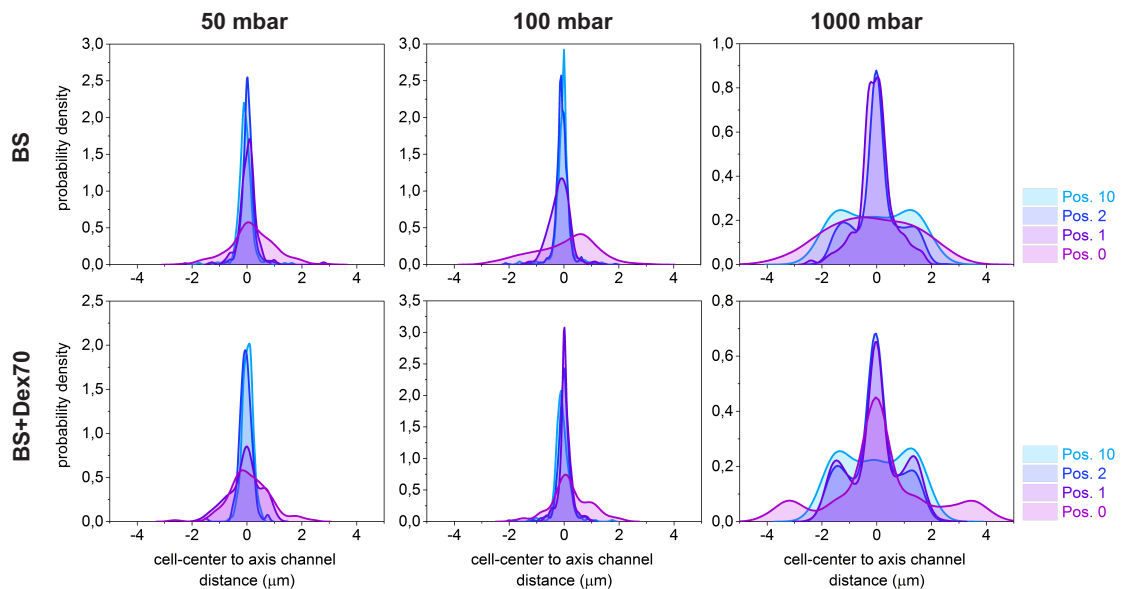


**Fig. 54:** Probability density of the cell-center to channel-axis distance for  $\Delta P = 50, 100,$  and  $1000$  mbar in BS (first row) and BS+Dex70 (second row).

The cells enter the channels randomly, independent of the pressure drop and the solution. In Fig.54, the probability density of the cell-center to channel-axis distance is plotted for the cell flow in BS and BS+Dex70 solutions. A centered axial alignment is observed for  $\Delta P = 50$  to  $100$  mbar from position 1 to 10 in both BS and BS+Dex70 solutions. A different arrangement is observed for  $\Delta P = 1000$  mbar, where the cells tend to have a non-centered alignment with the axis of the channel starting to evolve from position 2 (see in Fig.54 the side peaks that appear) up to position 10. Cells that are positioned symmetrically up and above the channel-axis, are located at around a distance of  $1.6 \mu\text{m}$  in position 2 and increasing to around  $1.8 \mu\text{m}$  at position 10. A similar behavior is

observed when the cells flow in the solution with macromolecules. However, in this last case, is still possible to distinguish in position 10 a small peak at the center of the channel (see Fig.54). Subsequently, the evolution of the off-center cell positioning seems to be slower than the evolution of cells flowing in a solution without macromolecules. This could be due to the increase of almost 70% on the viscosity of the BS+Dex70 solution compared to BS solution. Comparing the cell-center to axis channel distance between healthy RBCs and sRBCs flowing in BS solution (see Fig.45 for the curves in the case of healthy RBCs), we observed that at 50 and 100 mbar the cell distribution is mostly the same for both solutions, while at 1000 mbar the bimodal distribution of the spanwise cell-positioning is very pronounced at position 1 for healthy cells, while for sRBCs seems to start in between position 1 and 2 and in position 10 is still less pronounced than the distribution of healthy cells at the same position. This fact could be due to the highest values in rigidity of the sRBCs compared to healthy cells (see Fig.19 for referential values). The spanwise cell-positioning is apparently related to the shape of the cell that depends on the flow velocity. At smaller velocities, the cells are mainly in the axial-centered configuration, but at higher velocities we found them to be in an off-centered configuration predominantly. However, the preferred shapes are different from parachute and slipper, that is the case of healthy RBCs. This can be due to the higher heterogeneity in rigidity and shape among sRBC population, where more elliptical cell shapes are found compared with healthy RBCs (see Fig.56).

Cluster formation in our experiment is a dynamic process and the total amount of cells of a cluster increases down the channel. We quantify this evolution maintaining the tube hematocrit in the range of 0.2 – 0.4%, where no significant differences in cluster formation were observed, and determined the occurrence of clusters type  $n$  at each channel position. In the previous section of clustering formation of healthy RBCs, the hematocrit was higher (0.4 – 0.8%). To allow a direct comparison of the quantification of the cluster formation between healthy and sRBCs, a new set of experiments were done for healthy RBCs keeping the tube hematocrit fixed between 0.2 – 0.4%. The results are shown in Fig.55.

In BS solution, most cells enter the channels as singlets ( $n = 1$ ) of both healthy RBCs and sRBCs and just few as triplets or cluster type  $n = 4$ . Hydrodynamic cluster formation is favorable for healthy cells. This can be attributed to their higher flexibility compared with sRBC, where cells of up to 8 times stiffer can be found naturally among their population (see Fig.19). Moreover, the shape of sRBCs is more heterogeneous than healthy RBCs. To quantify this deviation, we obtained the eccentricity of at least 700 cells from a bright field image of healthy RBCs and sRBCs at rest. The normalized distribution of eccentricity is presented in Fig.56, where a Gaussian fitting ( $y = y_0 + Ae^{(-0.5(x-x_c)/w)^2}$ ) was done for each case. The mean eccentricity of healthy RBCs is  $0.38 \pm 0.13$  and  $0.48 \pm 0.19$  for sRBCs. This higher value can be consequence of the constant sickling of sRBCs as well as the presence of irreversible cells whose shapes are deviated from the typical discocyte of healthy RBCs, being more elongated and elliptical shaped.

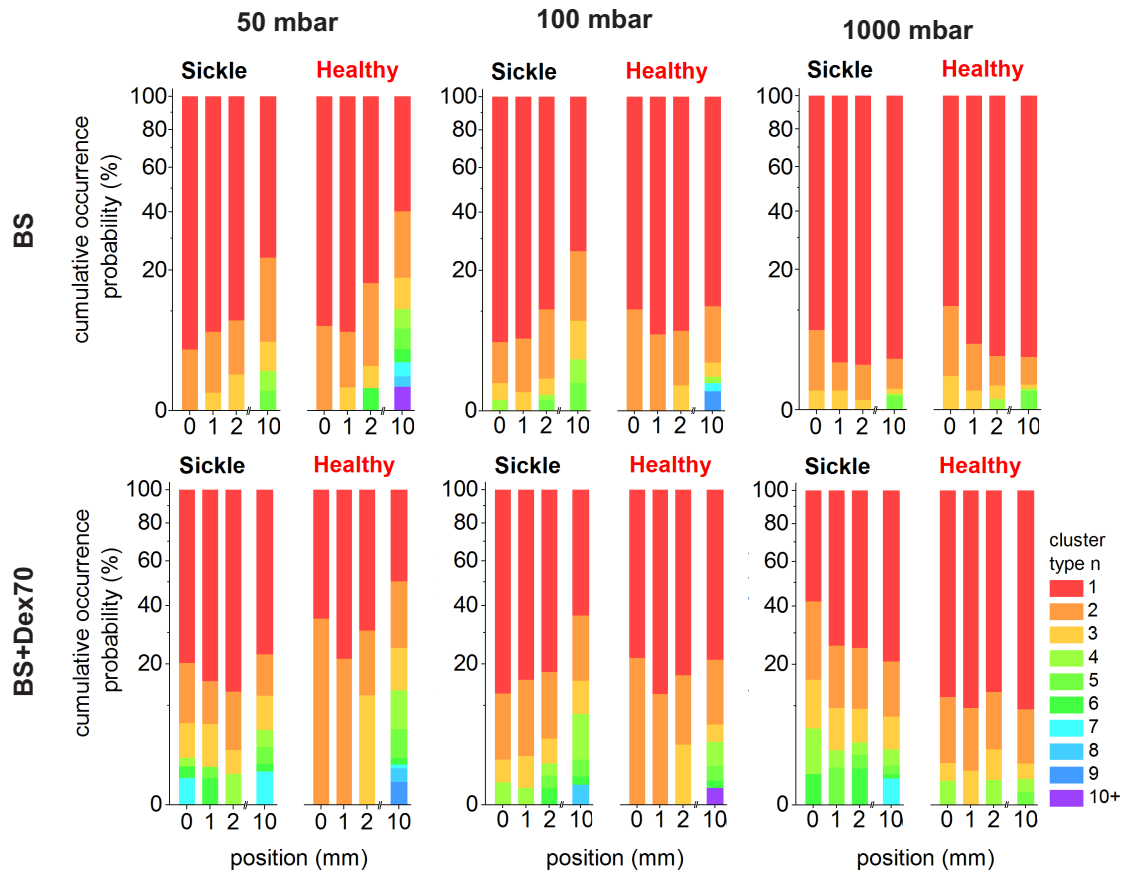


**Fig. 55:** Comparison of the cumulative occurrence probability between healthy RBCs (Healthy) and sRBCs (Sickle) of different cluster types  $n$  in BS solution (top) at four different distances from the entrance along the channel for  $\Delta P = 50, 100$  and  $1000$  mbar and BS+Dex70 solution (bottom). Type 1 indicates single cells.

In the presence of macromolecules rouleaux enter the channel and even clusters of type  $n > 6$  are observed (see 50 mbar, bottom in Fig.55), that is not the case of healthy cells. Indeed, more clusters in the case of sRBCs tend to enter to the channels compared to the healthy case. This can be due to the highest robustness of clusters formed among sRBCs compared to clusters formed between healthy RBCs (see Table 5). However, except in the case of cells flowing at 1000 mbar, the formation of clusters is faster in the healthy cases. This can be again attributed to the higher flexibility among healthy RBCs compared to sRBCs. Further experiments will be needed to explore the role of stiffness in the cluster formation.

In all cases, there is a monotonic increment in the cluster type  $n$  down the channel. This last observation in the BS solution clearly indicates that hydrodynamic interactions induce cluster formation along the channel in the case of sRBCs. This conclusion is also true for the solutions with dextran, where a few clusters appear to break up between

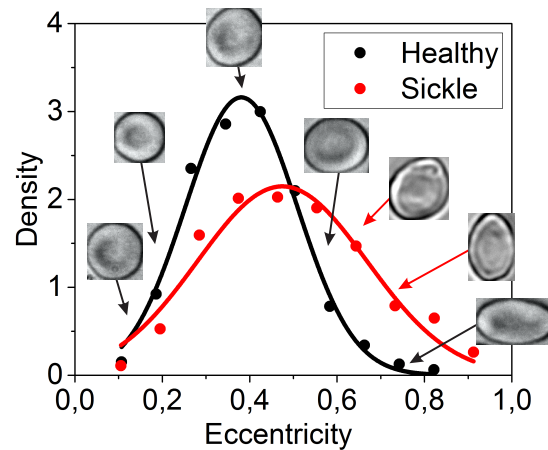


**Fig. 56:** Eccentricity of a population of healthy RBCs compared to the eccentricity of a population of oxygenated sRBCs. Representative images of cells are presented. A higher heterogeneity is observed for sRBCs, where the presence of irreversible sRBC cells as well as constant sickling, deviate the shape from the discocyte shape observed for healthy RBCs.

positions 0 and 1 at first, but more clusters subsequently form down the channel. One may speculate from the larger number of the polymer-induced clusters that they should also be more robust against additional perturbations from irregularities in the flow as was also the case for healthy cases. However, this hypothesis should be verified.

Increasing the flow strength does not intensify the cluster formation either in healthy patients, either in sickle cells. Again, if we compare configurations after equal residing time in the channel, e.g. position 1 at  $\Delta P = 100$  mbar and position 10 at  $\Delta P = 1000$  mbar in the BS solution, the cluster size distributions are relatively close in both low and high stress configurations. Then, flow-induced deformations of cells and the subsequent hydrodynamics interactions do not depend much on the flow stress. But, in the macromolecules cases, we observe a increase of the number of clusters unlike in healthy case where an increment of isolated cells between the low and the high stress configurations is observed (see Fig.46). It means that in sickle cells, rouleaux are even more robust against perturbations than the case of healthy cells.

### Probability density functions of the cluster length

Evaluating the probability density function of the cluster length  $L$  of cluster type  $n = 2$  (Fig. 57), we can observed that at  $\Delta P = 50$  mbar there is a peak appearing at around  $4.5 \mu\text{m}$  (see Fig.58 for some examples) which was not the case in healthy cells (see top graph in Fig.50). Still at  $\Delta P = 100$  and  $1000$  mbar, the tendency of the cluster length distribution is comparable to the case of healthy RBCs, being also apparently bimodally distributed. The pronounced peak around  $4.5 \mu\text{m}$  implies that sRBCs can often be very close each other and adding macromolecules that induce aggregation can enhance or increase the formation of rouleaux in flow. In the case of BS+Dex70 solution, the curve

at  $\Delta P = 50$  mbar shows a pronounced tendency to the lower cluster length values. At higher pressure drops, there is also a shifted to the lower cluster length values. These findings indicate that stronger rouleaux are formed compared to the rouleaux formation in healthy RBCs under the same conditions (see middle graph in Fig.50 for comparison). Evidently, the strength of the rouleaux due to the presence of dextran is higher in sRBCs than in healthy RBCs. Still it is possible to distinguish a bimodal distribution on the curves at  $\Delta P = 100$  and 1000 mbar in BS+Dex70 solution.

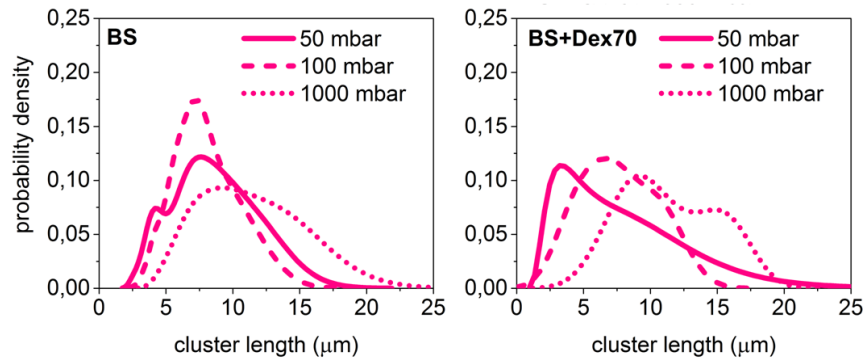


**Fig. 57:** Probability density of the characteristic cluster length  $L$  of the cluster type  $n = 2$  for BS (left) and BS+Dex70 (right) solutions for the three different pressure drop  $\Delta P = 50$ , 100 and 1000 mbar.

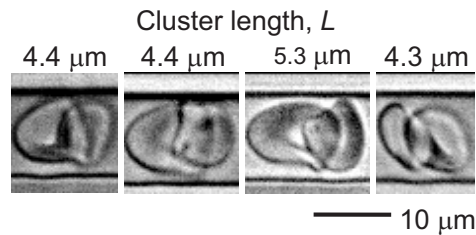


**Fig. 58:** Example images of clusters type  $n = 2$  with a cluster length,  $L$ , around 4.5 μm.

### Shape classification of hydrodynamic clusters

The hydrodynamic clusters of the cluster type  $n = 2$  in BS solution were classified according to their shape (see Fig.34). The resulting cluster-shape classification are presented in Fig.59.

For lower pressure drop ( $\Delta P = 50$  mbar), there is a big tendency to have parachutes. The peak of parachute-parachute (PP) configuration it is located at a cluster length of around 11 μm, shifted around 3.5 μm from the preferential cluster length that is around 7.5 μm (see Fig.57 to compare). At  $\Delta P = 100$  mbar, the number of PP configuration

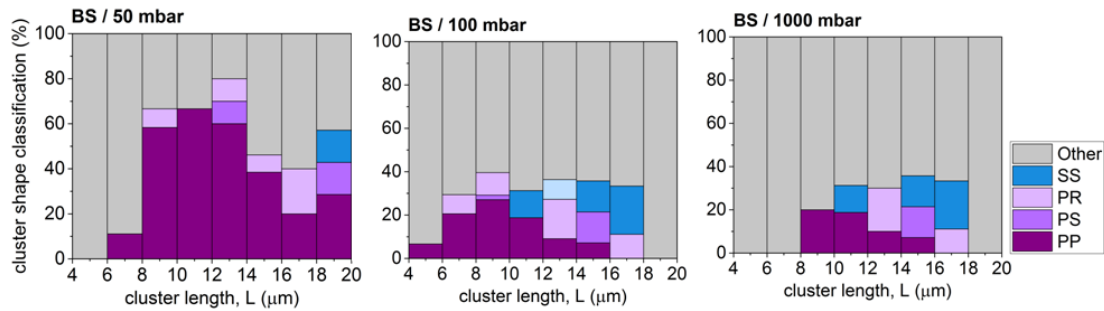


**Fig. 59:** Percentage of the different shapes of clusters of type  $n = 2$  per cluster length at 50, 100 and 1000 mbar in BS solution from left to right.

decreases, but is the preferred configuration of the preferential cluster length (see Fig.57 to compare) that is the case of healthy cells as well, even though in this last case, a much higher number of PP configurations were observed. Finally, at  $\Delta P = 1000$  mbar, the configuration others is the most frequent and then, different from the healthy case where the most popular shape was slipper-slipper (SS) for this high stress configuration. It is believed that parachute and slipper configurations at the microcirculatory level could increase the cell exposure area to the wall vessels in favor of the oxygen interchange between the cells and the tissues. Clearly this is not the case of sRBCs where other configurations (see for some examples Fig.60) are in all the stress configurations ( $\Delta P = 50, 100$  and  $1000$  mbar) more frequent. Even sRBCs flow slower than healthy RBC under the same conditions (see Table 7 and 11) increasing the transient time of sRBCs and their possible increase of oxygen exchange, the shape that the cells adopt are in general far from parachute and slipper, that can counteract the increases of oxygen exchange as the area exposure decreases.

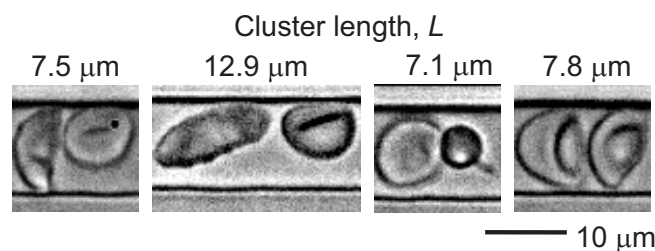


**Fig. 60:** Example images of clusters type  $n = 2$  classified as others.

## 4.4 Conclusion

### Conclusion (english)

Our study shows that the flow of soft deformable objects that interact either via hydrodynamic or via polymer induced forces leads to a complex clustering scenario. It is the pronounced flow-structure or rather the flow-shape coupling that is responsible for this rich dynamic. In hard sphere suspension or emulsions, polymer induced interactions (either based on bridging or on depletion) are only in the order of 3 to 20  $k_B T$  and would never be sufficient for clusters to resist the shear forces due to the flow profile. RBCs can deform and thus form large interaction surfaces which results in much larger interaction energies in the order of 10000  $k_B T$ . Furthermore, hydrodynamic forces in colloid systems are much more simple because they remain at least roughly spherical and the flow field is easier to determine.

In our system, we find that cluster formation in micro-capillaries under healthy physiological conditions should be caused by a combination of hydrodynamic and macromolecule-induced interactions (far from zero and close to zero inter-cellular distance between the surfaces of the cells, respectively). Macromolecule-induced interactions are not fully overcome by shear stresses within the physiological range, and they contribute to cluster stability. Yet, as confirmed by our two-dimensional numerical simulations, cluster stabilization by hydrodynamics becomes predominant in the upper part of the physiological range of flow velocities.

The physical origin of the pronounced bimodal distribution of the cell-to-cell distances in the hydrodynamic clusters results from changes in the cell shapes. Whether the changes in shape are dynamical because of the shape-flow coupling, or because of differences in the physical properties of the cell, remains an open question. To answer this, experiments will be necessary to resolve the temporal dynamics of the cluster formation process in direct comparison with three-dimensional simulations. Furthermore, it might be worthwhile to do experiments with RBCs that have been separated by density. This yields to a separation by age and eventually leads to a more monodisperse distribution of their physical parameters such as the bending rigidity.

Sickle cells show differences in flow compared to healthy cells and could in general be due to the formation of robust clusters in the presence of macromolecules that induce aggregation in the suspending media, as well as due to the decrease of cell deformability that lead to a different cluster length configuration, robust cluster formation in the presence of macromolecules and different shape configurations.

## Résumé (français)

Notre étude montre que l'écoulement d'objets déformables mous qui interagissent soit par voie hydrodynamique, soit par les forces induites via des polymères, mène à une formation d'agrégats très complexe. C'est la structure de l'écoulement ou plutôt le couplage écoulement-forme qui est responsable de cette dynamique si riche. Dans les suspensions de sphères dures ou les émulsions, les interactions induites entre polymères (soit par "bridging" soit par déplétion) sont seulement de l'ordre de 3 à 20  $k_B T$  et ne seraient jamais suffisantes pour que les agrégats puissent résister aux forces de cisaillement causées par le profil de l'écoulement. Les GRs peuvent se déformer et par conséquent, former de larges surfaces d'interaction, ce qui donne des énergies d'interaction beaucoup plus élevées, de l'ordre de 10000  $k_B T$ . De plus, les forces hydrodynamiques dans les colloïdes ou dans les systèmes de gouttelettes sont plus simples car elles restent quasi sphériques et le champ d'écoulement est plus facile à déterminer.

Dans notre système, nous trouvons que la formation d'agrégats dans les micro-capillaires et ce, dans des conditions physiologiques saines doit être causée par l'hydrodynamique et par les interactions induites par le biais de macromolécules (distances intercellulaires loin de zéro et proche de zéro entre les surfaces des cellules, respectivement). Les interactions induites par les macromolécules ne sont pas totalement dominées par les contraintes de cisaillement dans le domaine physiologique et contribuent à la stabilité des agrégats. Ainsi, comme le confirme nos simulations numériques en deux dimensions, la stabilisation des agrégats par l'hydrodynamique devient prédominante dans la partie physiologique supérieure des vitesses d'écoulement.

L'origine physique d'une telle distribution bimodale des distances cellule-cellule des agrégats hydrodynamiques est le résultat de changements dans la forme des cellules. Le fait que les changements de forme soient dynamiques à cause du couplage écoulement-forme ou causés par des différences dans les propriétés physiques de la cellule, reste sujet à discussion. Pour répondre à cette problématique, des expériences sont nécessaires pour résoudre la dynamique temporelle du processus de formation d'agrégats, en comparaison directe avec les simulations en trois dimensions. De plus, il peut être digne d'intérêt d'effectuer des expériences avec des GRs qui ont été séparés par densité. Ceci mène à une séparation par âge et éventuellement, à une distribution des paramètres physiques plus monodispersée.

Dans le cas de la drépanocytose, les GRs montrent des différences d'écoulement comparés aux GRs sains et, de manière générale, ces différences peuvent être dues à la formation d'agrégats robustes en présence de macromolécules, induisant l'agrégation dans le milieu de suspension mais aussi à cause d'une déformabilité des cellules moins importante, responsable de plusieurs configurations (en taille) des « clusters », la formation de « clusters » plus robustes en présence de macromolécules et différentes configurations de formes.

## Zusammenfassung (deutsch)

Unsere Studie zeigt, dass der Fluss weicher, deformierbarer Objekte, die entweder hydrodynamisch oder durch Polymer induzierte Kräfte interagieren, zu einem ausgeprägten Aggregationsverhalten führt. Die komplex Flusstruktur bzw. die Kopplung zwischen Fluss und Form ist für diese ausgeprägte Dynamik verantwortlich. Für den Fall harter Kugeln in Suspensionen oder Emulsionen sind die Polymer induzierten Interaktionen (basierend auf Depletion oder Bridging) nur in der Größenordnung von 3 bis  $20 k_B T$ , was für ein Aggregat nicht ausreichen würde um Flusskräften (aufgrund des Flussprofils) standzuhalten. RBC's sind deformierbar und können daher große Interaktionsflächen formen, was zu deutlich höheren Interaktionsenergien in der Größenordnung von  $10000 k_B T$  führt. Darüber hinaus sind hydrodynamische Kräfte in kolloidalen oder Tropfensystemen wesentlich einfacher, da sie annähernd rund bleiben und das Flussfeld einfacher zu bestimmen ist.

In unserem System haben wir festgestellt, dass die Formation von Aggregaten unter gesunden physiologischen Bedingungen durch eine Kombination aus hydrodynamischen- und Makromolekül-induzierten Interaktionen hervorgerufen wird (weit entfernt von keiner und nahe an keiner interzellulärer Distanz zwischen den Zelloberflächen). Makromolekül-induzierte Interaktionen werden nicht vollständig durch Schubspannungen innerhalb physiologischer Grenzen überwunden und tragen zur Stabilität von Aggregaten bei. Wie durch unsere zweidimensionalen numerischen Simulationen bestätigt wurde, überwiegt die Stabilisierung von Aggregaten durch Hydrodynamik im oberen Bereich der physiologischen Grenzen der Flussgeschwindigkeit.

Der physikalische Ursprung der ausgeprägten bimodalen Verteilung des Zell-zu-Zell Abstandes in hydrodynamischen Aggregaten resultiert aus einer Veränderung der Zellform. Ob die Änderungen der Form aufgrund der Form-Fluss Kopplung oder aufgrund der Unterschiede der physikalischen Eigenschaften der Zelldynamisch sind, bleibt eine offene Frage. Um dies zu beantworten sind Experimente nötig, welche die zeitabhängigen Dynamiken des Aggregatbildungsprozesses in direkten Vergleich zu dreidimensionalen Simulationen setzen. Darüber hinaus könnte es sinnvoll sein die Experimente mit RBCs durchzuführen, die aufgrund ihrer Dichte separiert wurden. Dies führt zu einer altersabhängigen Separation und letzten Endes zu einer monodisperseren Verteilung der physikalischen Parameter, wie zum Beispiel der Biegesteifigkeit.

Sichelzellen zeigen Unterschiede im Fluss bei Vergleich mit gesunden Zellen und könnten generell nicht nur mit robusten Aggregaten in der Anwesenheit von Makromolekülen, welche die Aggregation in suspendierenden Medien induzieren, begründet werden, sondern auch durch die Abnahme der Zelldeformabilität, die zu verschiedenen Aggregatslängen führt sowie robusten Aggregaten bei Anwesenheit von Makromolekülen und wodurch andere Zellformen hervorgerufen werden.

# 5 Chapter 5

## Self-margination of sickle cells

### 5.1 Introduction

#### 5.1.1 Aggregation and Self-margination in sickle cell anemia

A recent numerical study on the low-Reynolds-number flow of dilute suspensions of binary capsules, has found that margination could happen due to the change of rigidity, size and shape [78–82].

Platelets and white blood cells migrate towards the capillary walls while the flexible healthy red blood cells (RBCs) migrate to the center. Sickle red blood cells (sRBCs) have a higher variation in density and rigidity compared to healthy cells. Then, a natural question arises: do sRBCs self-marginate?

In healthy cells, RBC aggregation seems to enhance margination of white blood cells when the shear rate decreases [73]. This can be related to the fact that RBCs accumulate more in the core of the vessels due to the formation of rouleaux, producing an improvement in margination of white blood cells. In the case of SCA patients, RBC aggregation is abnormal. At steady state, aggregation is decreased compared to healthy individuals. However, once an aggregate is formed, its robustness is 2 to 3 fold higher [8].

Abnormal RBC aggregation properties could play a role in the onset of vaso-occlusive events in SCA. Patients with the highest RBC aggregate strength would be at higher risk to develop acute chest syndrome [125]. The RBC aggregation index, measured by laser backscatter technique, was greatly enhanced during vaso-occlusive crisis compared to values obtained without crisis. Density gradient separation of blood from sickle patients reveals a marked heterogeneity of cells. The more flexible less dense cells (with irregular discocytes shape) are more adherent to the endothelial cells than the more rigid and dense ones (irreversible sRBCs). This disparity is attributed to the difference in deformability of these two population of cells, since the irregular shape of irreversible sRBCs prevent sufficient membrane contact area with the endothelium, thus inhibiting their ability to form attachments. Discocytes sRBCs can be 4 to 5 times more adherent to endothelial cells than healthy RBCs. Adhesion can be mediated by plasma factors [123] as well as by adhesion molecules [9] that are in the sRBC membrane and in the endothelium (receptors). These molecules can interact directly or with the help of bridging molecules (ligands). Bridging molecules can be free in plasma.

By mixing suspensions with a given ratio of rigid-dense versus flexible-less dense sRBCs dyed with different fluorophores, we explored self-margination of sRBCs at different hematocrit levels, wall shear rates, and suspending media that include aggregative factors. To obtain the relative position of the different sRBC populations in the core of the flowing cells, measurements of the cell-free layer (CFL) for the different flowing conditions were needed. In the following, a brief description and the general importance of the CFL is done.

### 5.1.2 Cell-free layer, CFL

Blood is known to phase separate in the microcirculation leaving a CFL adjacent to the vessel wall and a higher hematocrit at the center. The CFL modifies blood viscosity. As a consequence, the CFL contributes importantly to microvascular function since effective blood viscosity and wall shear rate determine wall shear stress, one of the principal stimuli for release of the vasodilators, nitric oxide (NO), and prostaglandins by the endothelium [146]. While data on the CFL width in the microcirculation and *in vitro* is scarce in the literature, no measurements have been reported on this important rheological feature in SCA blood, neither *in vivo* nor *in vitro*.

CFL is at the heart of microcirculatory properties such as the local hydrodynamic resistance. In this study we report values of the CFL in SCA cells, flowing at different velocities and suspending media, both with non-inducive and inducive aggregation factors. The values obtained, were used to get the relative position of the different sRBC populations in the core of the flowing cells. These values were essential to investigate self-margination of sRBCs.

## 5.2 Materials and experimental methods

Sickle cells samples were provided by the Laboratoire de Biochimie et de biologie moléculaire of the Hospital Edouard Herriot in Lyon. The samples were centrifuged at 1000 g for 3 minutes at 23°C. Plasma was removed and reserved in a plastic container, and stored at 4°C to use it as a suspending medium later. The buffy coats were removed by aspiration and the sRBCs were washed 3 times in PBS. The total volume of sRBCs was measured by the help of a pipette. sRBCs were then separated as a function of their densities by discontinuous gradient Percoll-based solutions with densities of 1.085, 1.092, 1.101, 1.107 and 1.122 g/ml, respectively as described in Chapter 3. These densities correspond to mean corpuscular hemoglobin concentration, MCHC, of 31.2, 34.5, 38.7 and +42 g/dl, respectively [147]. The final sRBCs fractions were called band I, II, II, IV, and V, respectively. After separation, the volume of each band was measured with the help of a pipette. A define amount of sRBCs (1/16 of the total sRBCs volume) with densities between 1.092-1.101 g/ml (Band II) and 1.107-1.122 g/ml (Band IV) were labeled with the fluorophores PKH 26 and 67, respectively. After labeling, all fractions

of sRBCs were mixed up again.

Solutions at two different hematocrits are prepared in different media: PBS+1 mg/ml of BSA is called base solution or BS. Further suspensions were prepared adding 20 mg ml<sup>-1</sup> of dextran 70 (molecular weight of 70 kDa) to the BS. This suspending media was called BS+Dex70. This amount of dextran 70 is known to induce an interaction energy of  $\epsilon = 4.8 \mu\text{J m}^{-2}$  among healthy RBCs [36], mimicking an interaction energy induced by a physiological amount of fibrinogen. Finally, autologous plasma was used as suspending media. This solution was called simply Plasma. Glass capillary chambers were built and observed under an inverted microscope as described in Chapter 3. The cells were injected into the channels at 4 constant pressure drops of  $\Delta P = (25, 20, 100, 200)$  mbar. Stop flow technique (see Chapter 3 for details) is applied before scanning the cell positions and obtain the images for data analysis.

## 5.3 Results and discussions

### 5.3.1 Patients blood's composition

4 patients were studied. The band volume fraction ( $V_B/V$ , where  $V_B$  is the volume of each band of sRBCs, and  $V$  is the total volume of sRBCs) was obtained for each patient. The HbS as well as the HbF content (both percentages in respect to the total hemoglobin content) for each patient were provided by the staff of the Hospital Edouard Herriot. These values are summarized in Table 12. For a better visualization, the band volume fraction for each sRBC band is plotted and presented in Fig.61.

	Band volume fraction					Hemoglobin	
	I	II	III	IV	V	HbS (%)	HbF (%)
<b>Patient 1</b>	0.11	0.39	0.13	0.29	0.08	87.5	5.7
<b>Patient 2</b>	0.07	0.49	0.17	0.19	0.08	87.4	5.7
<b>Patient 3</b>	0.02	0.40	0.33	0.21	0.04	79.7	14.1
<b>Patient 4</b>	0.43	0.10	0.25	0.13	0.09	88.0	2.5

**Tab. 12:** Band volume fraction of each sRBC band, and HbS and HbF content of each patient is presented.

### 5.3.2 Solutions

4 patient's sRBCs were suspended in BS solution, 3 in BS+Dex70 solution and 2 in their autologous plasma. Table 13 summarized the suspending media used for each patient.

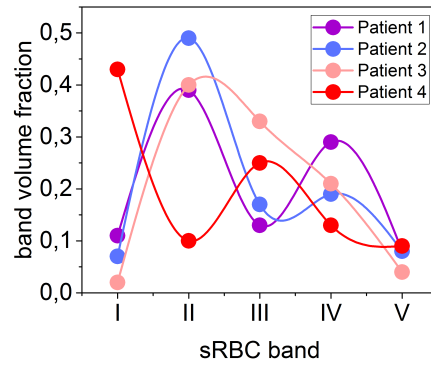


**Fig. 61:** Plot of the band volume fraction of each sRBC band. Patients 1 and 2 show a bimodal distribution of bands. Patient 3 has an additional increment of band III while Patient 4 has a high population of reticulocytes and band III, and low population of band II and IV, contrary to all the rest of the patients.

	BS	BS+Dex70	Plasma
<b>Patient 1</b>	✓	✓	✓
<b>Patient 2</b>	✓	✓	✓
<b>Patient 3</b>	✓	✓	-
<b>Patient 4</b>	✓	-	-

**Tab. 13:** Summary of the suspending media used for the experiments for each patient.

### 5.3.3 Hematocrit

Two solutions at different bulk hematocrit are prepared to investigate the effects of tube hematocrit  $H_t$  values classically found in patients with sickle cell anemia. The tube hematocrit,  $H_t$ , was obtained as described in Chapter 3. The average values of  $H_t$ , for each suspending media per patient, are summarized in Table 14. The average low  $H_t = 18.49 \pm 0.99\%$ , and the average high  $H_t = 25.87 \pm 1.24\%$ .

### 5.3.4 Velocity profile and CFL

RBCs in Poiseuille flow migrate toward the center of the tube, forming a central core of cells, and a CFL near the wall as it is shown in the sequence of images in Fig. 62 for sRBCs flowing in BS. The increases on the thickness of the CFL values, represented by a red dash line on each image, is clearly observed when pressure drop increases from 25 to 200 mbar in both low and high  $H_t$ .

The resulting velocity profile of both, core and suspending media at different pressure drops were obtained as described in Chapter 3. The resulting velocity profiles and their associated errors (standard deviation) are shown in Fig. 63 for BS solution, as an example. Light blue dashed lines correspond to the parabolic profiles of the Newtonian suspending-

	BS	BS+Dex70	Plasma
	Low Ht		
<b>Patient 1</b>	17.67 ± 2.82	18.84 ± 3.46	19.33 ± 2.89
<b>Patient 2</b>	17.99 ± 2.92	18.35 ± 2.92	18.72 ± 2.77
<b>Patient 3</b>	19.32 ± 2.91	20.12 ± 3.35	-
<b>Patient 4</b>	16.04 ± 2.73	-	-
	High Ht		
<b>Patient 1</b>	26.88 ± 3.46	28.27 ± 4.40	27.03 ± 4.13
<b>Patient 2</b>	22.33 ± 1.71	23.16 ± 2.77	24.40 ± 3.36
<b>Patient 3</b>	26.99 ± 4.06	26.23 ± 3.83	-
<b>Patient 4</b>	27.50 ± 4.78	-	-

**Tab. 14:** Average hematocrit per patient obtained by suspending media. Low  $H_t$  values are presented at the top, and high  $H_t$  values are presented at the bottom of the table.

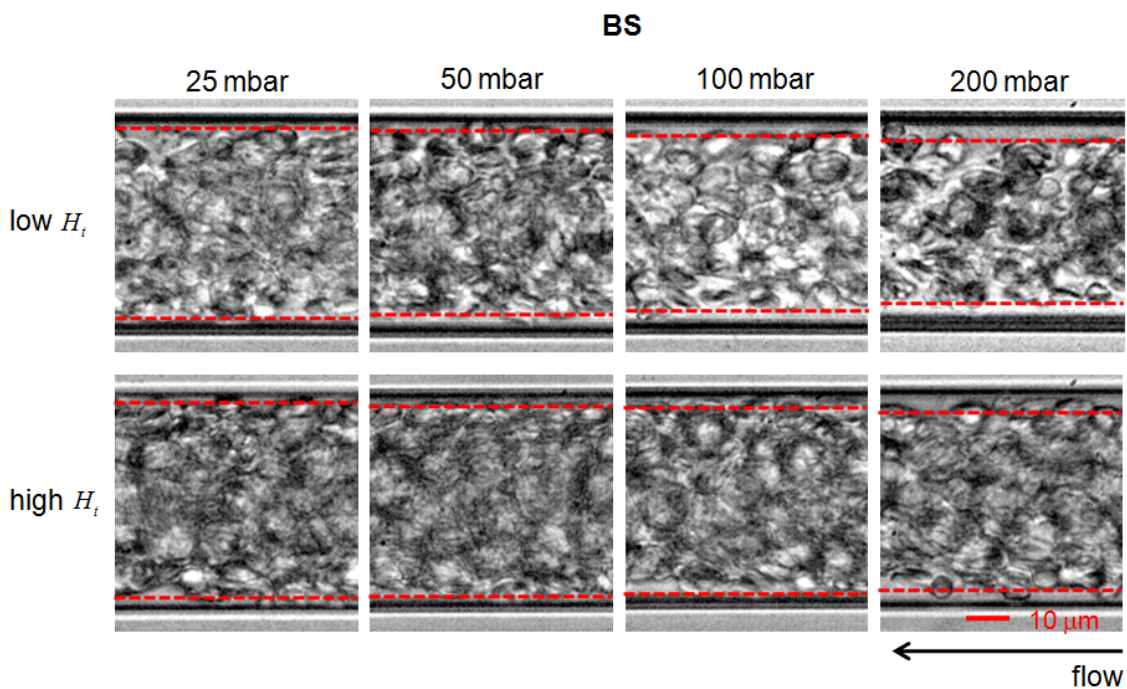


**Fig. 62:** Representative images of sRBCs flowing at different pressure drops in BS. It is possible to notice the increasing of the CFL thickness when pressure drop increases.

ing media in the absence of cells for the same pressure drop and the same channel length.

The velocity profile in all cases does not correspond to the Newtonian flow profile and shows a reduction in magnitude: the flow rate decreases in the presence of cells. However, when pressure drop increases, the difference between Newtonian flow and the cell core velocity profiles mitigates. The velocity profiles for high  $H_t$  are flatter and lower in

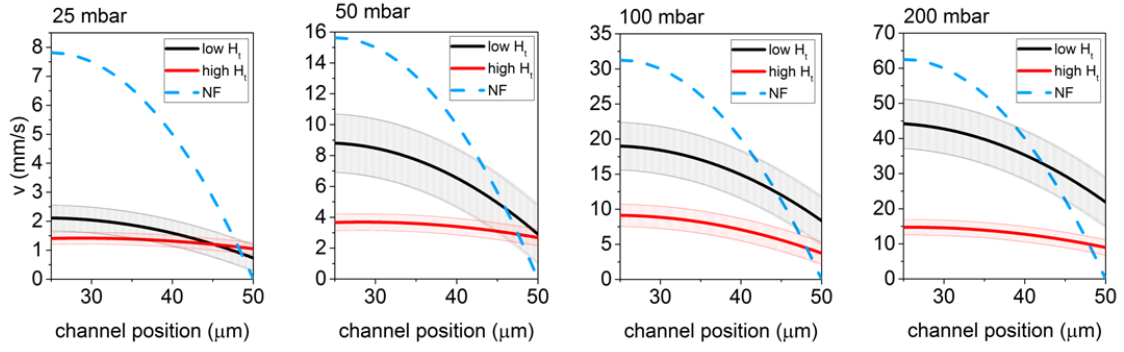


**Fig. 63:** Velocity profile of low (black straight line) and high (red straight line)  $H_t$  for BS at different pressure drops. The error zone is given by the standard deviation of the fitting from all data. Light blue dash line is the Poiseuille velocity profile of a Newtonian fluid with the same viscosity than the suspending media.

magnitude than the velocity profiles for low  $H_t$ . A similar behavior is observed in plasma or dextran, where macromolecules induce aggregation. In this last case, an important parameter to consider for analysis, is the influence of shear rate on the apparent blood viscosity, that appears to be not significant for the average shear rates above  $\bar{\dot{\gamma}} = 30 \text{ s}^{-1}$  in both *in vitro* and *in vivo* experiments. Below this value, strong effects of shear rate on viscosity are expected [148], attributed to RBC sedimentation and aggregation properties.

The fitting functions (see black and red lines in Fig. 63) give us the velocity profile for low and high  $H_t$ , from which the flow rate can be calculated. The mean value of a function  $f(x)$  between  $x = a$  and  $x = b$  is given by

$$\bar{f} = \frac{1}{b-a} \int_a^b f(x) dx \quad (13)$$

Knowing that the shear rate  $\dot{\gamma}(r)$ , as a function of the radial position  $r$ , is given by

$$\dot{\gamma}(r) = \frac{\Delta P \cdot r}{2\mu L} \quad (14)$$

where  $\Delta P$  is the pressure drop between the extremes of the tube,  $L$  the length of the tube, and  $\mu$  the viscosity of the core of cells. The mean shear rate  $\bar{\dot{\gamma}}$  can be obtained evaluating (14) in (13), with  $r$  between 0 and  $(R - \delta)$ , where  $R$  is the tube radius, and  $\delta$  is the CFL thickness. As a result,  $\bar{\dot{\gamma}} = v_{max}/(R - \delta)$ , where  $v_{max}$  is the maximum center-line velocity of the cell core. The mean shear rate will be used as a parameter to compare the behavior of sRBCs at different  $\Delta P$ . The different velocity values ( $v_{max}$ , and the maximum velocity of the newtonian suspending fluid,  $v_N$ ), as well as  $\bar{\dot{\gamma}}$ , are summarized in Table 15 for each suspending media.

CFL thickness,  $\delta$ , was obtained as described in Chapter 3, and plotted versus the mean

$H_t$	$\Delta P$ (mbar)	$\bar{\gamma}$ (1/s)	$v_{max}$ (mm/s)	$v_N$ (mm/s)
<b>BS</b>				
low	25	95.52 ± 6.90	2.11 ± 0.06	7.80
	50	426.94 ± 30.40	8.81 ± 0.25	15.63
	100	1004.30 ± 46.40	19.02 ± 0.54	31.25
	200	3512.00 ± 530.08	44.35 ± 1.12	62.50
high	25	65.29 ± 3.12	1.41 ± 0.03	7.80
	50	182.16 ± 13.02	3.69 ± 0.24	15.63
	100	444.52 ± 20.94	9.13 ± 0.16	31.25
	200	733.39 ± 61.55	14.72 ± 0.48	62.50
<b>BS+Dex70</b>				
low	25	55.43 ± 8.29	1.02 ± 0.03	4.68
	50	147.34 ± 9.95	3.19 ± 0.09	9.36
	100	361.94 ± 30.61	7.88 ± 0.21	18.71
	200	813.12 ± 68.69	16.20 ± 0.51	37.43
high	25	46.32 ± 5.46	1.05 ± 0.04	4.68
	50	103.80 ± 7.00	2.27 ± 0.09	9.36
	100	193.50 ± 10.82	4.29 ± 0.11	18.71
	200	526.51 ± 33.73	11.06 ± 0.34	37.43
<b>Plasma</b>				
low	25	28.96 ± 22.18	0.73 ± 0.03	6.01
	50	81.69 ± 9.04	1.78 ± 0.07	12.02
	100	319.35 ± 24.51	6.23 ± 0.25	24.04
	200	804.25 ± 55.84	13.27 ± 0.28	48.08
high	25	35.84 ± 3.13	0.81 ± 0.03	6.01
	50	94.52 ± 13.93	2.06 ± 0.13	12.02
	100	220.99 ± 13.52	4.87 ± 0.12	24.04
	200	573.54 ± 38.41	11.27 ± 0.37	48.08

**Tab. 15:** From left to right: tube hematocrit,  $H_t$ , pressure drop,  $\Delta P$ , mean shear rate,  $\bar{\gamma}$ , maximum center-line velocity of the cell core,  $v_{max}$ , and the maximum center-line velocity of the newtonian fluid,  $v_N$ , whose viscosity is the one of the suspending media. The values were averaged over all patient for each solution.

shear rate,  $\bar{\gamma}$  (Fig.64).

The thickness of the CFL increases when  $\bar{\gamma}$  increases, and decreases with the hematocrit increases. At low  $H_t$ , the thickness of the CFL is similar between BS and BS+Dex70, but higher in the case of Plasma as shown in Fig.64. At high  $H_t$  (see right graph in Fig.64), the same trend, but with lower values, is observed with respect to the values obtained at low  $H_t$ . Aggregation effects due to plasma and to dextran, are different. Aggregation seems to be more robust when the cells flow in autologous plasma. This

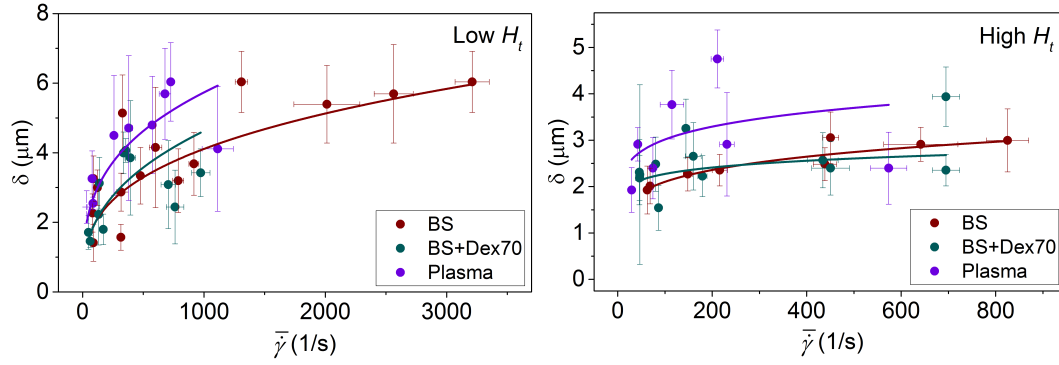


**Fig. 64:** CFL thickness,  $\delta$ , versus mean shear rate,  $\bar{\gamma}$ , for BS, BS+Dex70 and Plasma solutions.

fact can be due the presence and role of plasma factors in sRBC aggregation, that could increase the strenght on top of the ability of sRBC to aggregate (i.e., sRBC aggregability), that depends on cellular factors. To corroborate this finding, the sRBC disaggregation threshold have been measured for sRBC suspended in plasma and 3% of dextran 70 kDa at standarized hematocrit of 40% using laser backscatter techniques (LORCA, Mechatronics, The Netherland). The result for the disaggregation threshold in Plasma was  $343 \pm 160 \text{ s}^{-1}$  while in dextran the value was  $243 \pm 90 \text{ s}^{-1}$ . These results clearly indicates that sRBC aggregates are more robust in plasma than in dextran because of the contribution of both cellular and plasma factors to aggregation when sRBCs are suspended in plasma.

Aggregation maintains or increases the thickness of the CFL depending on the aggregant. A power fitting  $\delta = a\bar{\gamma}^b$  was performed on the data and represented by continuous lines (see Fig.64). The constants  $a$  and  $b$  for each case are summarized in Table 16.

Solution	<b>a</b>	<b>b</b>
Low $H_t$		
BS	$0.45 \pm 0.22$	$0.32 \pm 0.07$
BS+Dex70	$0.36 \pm 0.16$	$0.37 \pm 0.08$
Plasma	$0.67 \pm 0.16$	$0.31 \pm 0.05$
High $H_t$		
BS	$0.98 \pm 0.15$	$0.17 \pm 0.03$
BS+Dex70	$1.54 \pm 0.55$	$0.09 \pm 0.06$
Plasma	$1.69 \pm 0.91$	$0.13 \pm 0.12$

**Tab. 16:**  $a$  and  $b$  of the fitting  $\delta = a\bar{\gamma}^b$  on the CFL thickness data points in Fig.64.

In healthy case, *in vitro* experiments have shown that aggregation increases the thickness of the CFL [149] while *in vivo* experiments the thickness have reported to remain

the same with or without aggregating agents in the suspending media. For example, Kim et al. [146] performed *in vivo* experiments in the rat cremaster muscle. The authors used dextran 500 to induce red blood cell aggregation at the levels seen in blood of healthy humans. They found no significant difference in the thickness of the CFL that remains around  $3\ \mu\text{m}$  in arteriols with diameters of around  $50\ \mu\text{m}$ , systemic hematocrit of 41-42%, and  $v_{max}$  around 14-11 mm/s before and after dextran infusion, respectively. Pseudo shear rates (ranging from 100 to 1/s), defined as  $\bar{v}/D$ , where  $\bar{v}$  is the mean velocity and  $D$  the vessel diameter, and arterial pressure before and after infusion of the aggregant, did not change significantly, either. The authors argue that the variations in the CFL thickness is not significantly affected by increasing RBC aggregability, because the shear rates near the wall would be too high for aggregate formation. This behavior is comparable to our results, where mean shear rates between 100 and  $500\ \text{s}^{-1}$  (see Fig. 64), produces a CFL thickness of around  $2.5\ \mu\text{m}$  in both low and high  $H_t$  showing no significant differences between BS and BS+Dex70 solutions in each case, even though,  $H_t$  in our case is about half of the hematocrit used in Kim et al. experiments. From this difference in hematocrit, one can speculate that in our case, the CFL thickness should be bigger than the value reported by Kim et al., but instead, our value is lower. This could be an indication that the thickness of the CFL decreases for sRBCs in comparison with the CFL produced by healthy cells under similar conditions.

*In vitro* experiments performed by Maeda et.al. [149] on hardened (H) and elastic (E) microvessels isolated from rabbit mesentery, showed that the thickness of the CFL decreases by increasing hematocrit for both H and E microvessels. This is an expected result and have been also observed in our experiment (see Fig. 64). Maeda et al. also explored the CFL thickness depending on the cell rigidity. Results showed that CFL thickness decreases when cells become more rigid, condition that could be comparable of sRBCs that in average are more rigid than healthy RBCs (see Fig.19 for values of the shear modulus of both healthy RBCs and sRBC). Indeed, as discussed in the previous paragraph, our findings shows that the CFL thickness formed by sRBC apparently decreases compared to CFL formed by healthy RBCs under similar conditions. To corroborate this, additional experiments at different tube hematocrits should be done.

In the same study, Maeda et al. explored the role aggregation in the CFL formation adding different concentrations of dextran 70 to the suspending media. Increasing dextran concentration, produces an increase on the CFL thickness, result that seems to be in contradiction with ours as well as with Kim et al. results. However, the range of velocities and in consequence shear rates, explored by Maeda et al. is lower than our cases. At his velocity range, the shear rates near the wall would be too low to brake the aggregates and then, the aggregation as a parameter on CFL formation became significant.

An increase in the thickness of the CFL may reduce vascular resistance as discussed in the introduction. However, another physiological consequence would be a change in the nitric oxide (NO) scavenging effect of the RBC core. In fact, Liao et al. [150]

showed that, during flow, the scavenging of NO by RBCs in the vessel lumen was greatly reduced in isolated, blood-perfused arterioles, presumably because of the presence of the CFL. This an interesting consequence that should be considered in the case of SCA, where the presence of NO could be critical in the chain of events that produces vaso-occlusion (see Fig.20).

The values obtained for the CFL thickness under different conditions are interesting by themselves for their possible physiological consequences. For our research, the CFL thickness are essential to investigate self-margination of sRBCs as the core of cells are used get the relative position of the different sRBC populations, results that will be discussed in the following sections.

### 5.3.5 Bands distribution

For each patient, the distribution of the cells belonging to band II and IV is obtained as described in Chapter 3. We discuss in the following the results obtained for Patient 1.

#### Role of $\Delta P$

##### 1. Low $H_t$ .

First, we compared the behavior of each band for different pressure drops at low  $H_t$  without aggregating factors, i.e., in BS. The cell distribution is shown in Fig. 65. For band II, a variation closer to the channel center in the cell distribution is observed at increasing  $\Delta P$ . For band IV this variation seems to occur in the central zone (between channel center and the CFL position).

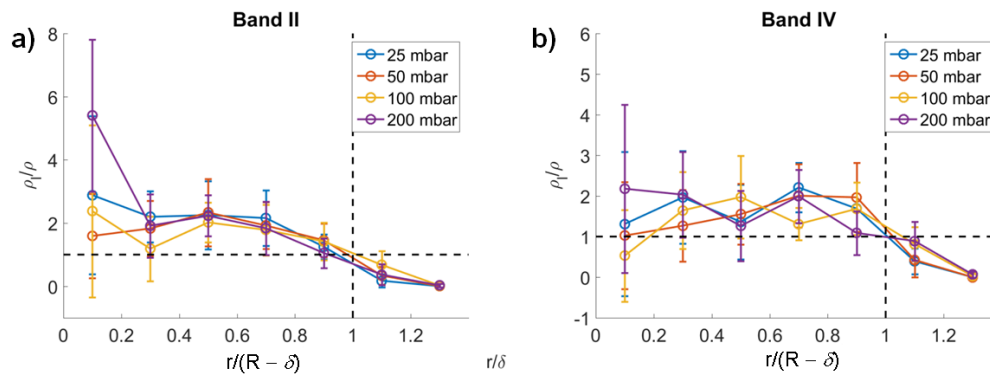


**Fig. 65:** Distribution of cells belonging to the a) band II and b) band IV flowing in BS at low  $H_t$  for each pressure drop.

To better visualize the cell distribution for each pressure drop and to compare the behavior between bands, we separate the distribution per pressure drop as shown in Fig. 66. Focusing on the behavior of the band II, we observe that at 25 mbar there is a higher concentration of cells near the center of the channel.

At 50 mbar, the cell population in the center drops down, while the rest of the cell distribution remains almost unchanged with respect to the distribution at 25 mbar. However, the concentration near the center of the channel increases again at 100 mbar and even more at 200 mbar.

Band IV, on the contrary, is distributed in the central zone at 25 mbar with a tendency to accumulate in the proximity of the CFL position. At 50 mbar, the concentration of cells is higher near to the CFL decreasing monotonously towards the channel center. Therefore, increasing shear rate seems to produce a displacements of the cells to the CFL zone. However, at 100 mbar, cells tend to accumulate in the central zone and move to the channel center at 200 mbar.

If we compare the distribution between bands, band II displacement is anti-correlated to the displacement of band IV in all cases: at 25 mbar, when band II accumulates in the center of the channel, we observed that band IV is present in the central region although a bigger concentration of cells is detected near the CFL position. When pressure drop increases to 50 mbar, RBC concentration in the center decreases in both cases generating a higher accumulation of band IV near to the CFL position. For the 100 mbar case, band II concentration increases in the center of the channel, band IV concentrates in the middle of the channel and at 200 mbar, both bands accumulate significantly more in the center of the channel.

We can also notice that a measurable population of cells from both bands are present after the CFL edge, flowing next to the channels wall.

Even if there should be a role of the pressure drop in the cell distribution, our data shown on Fig.65, do not show a significant trend. A plausible explanation of such a behavior can be found in the choice of the position in the channel where data were acquire (1 cm onwards the entrance of the tube). It is possible that this distance is sufficient to reach a stable relative band positioning or cell arrangement. Therefore, to have an overview on the relative distribution between bands, we average the cell distribution over all pressure drops for each of these cell populations. The resulting curve is presented in Fig.67. Here, band II shows an evident tendency to accumulate to the channel center while band IV is depleted from the center and accumulate mostly near the CFL position.

## 2. High $H_t$ .

The cell distribution at high  $H_t$  in BS is shown in Fig. 68. Band II distribution in the central zone, (a) in Fig. 68), changes with  $\Delta P$  while band IV (b) in Fig. 68) accumulate near the CFL position. However, the distributions are very similar, meaning that the increase in pressure drop is not playing a significant role on the cell distribution in any of the bands. An average of the distributions over all pressure drops is illustrated in Fig. 69.

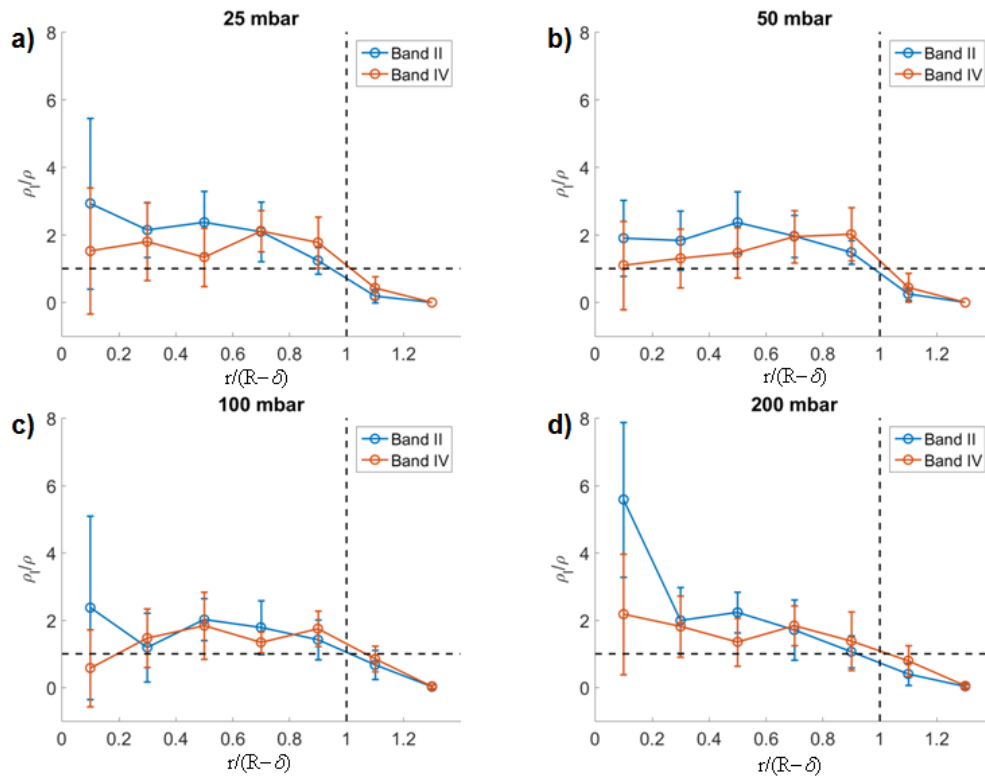


**Fig. 66:** Distribution of cells belonging to the a) band II and b) band IV flowing in BS at low  $H_t$  is presented for each pressure drop for patient 1.

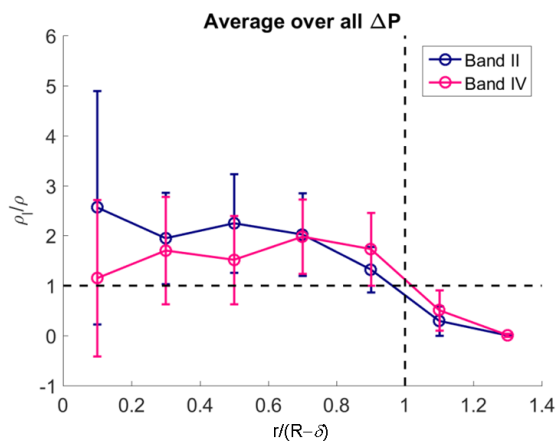


**Fig. 67:** Average cell distribution over all pressure drops of band II and IV flowing in BS at low  $H_t$  for patient 1.

It is possible to observe in Fig. 69, that band II is homogeneously distributed between the center of the channel and the central zone, while band IV has an evident tendency to accumulate near the CFL border.

The distributions of the bands for both low and high  $H_t$  in the rest of the patients

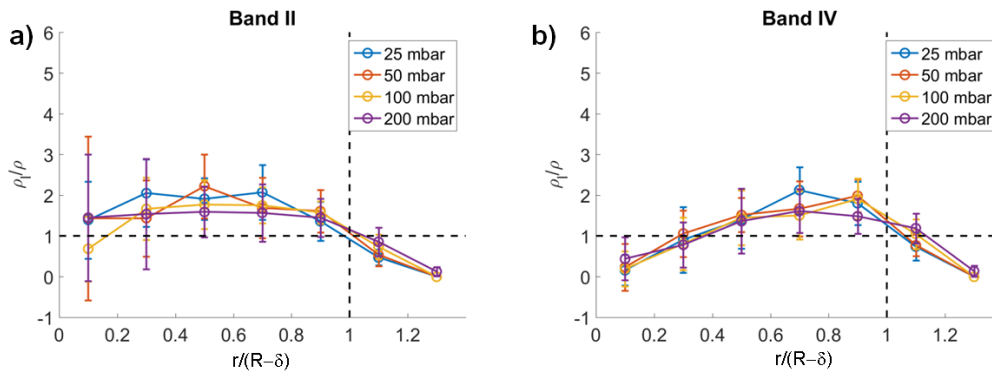


**Fig. 68:** Distribution of cells belonging to the a) band II and b) band IV flowing in BS at high  $H_t$  is presented for each pressure drop for patient 1.

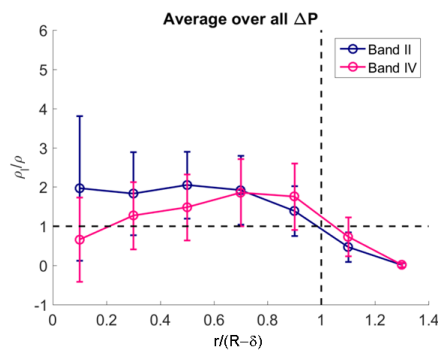


**Fig. 69:** Average cell distribution over all pressure drops of band II and IV flowing in BS at high  $H_t$  for patient 1.

do not show as well significant differences increasing the pressure drop. Therefore, we averaged the distributions over all pressure drops and plotted the curves for each patient in Fig. 70, in both cases of  $H_t$ , for better comparison.

Focusing first on low  $H_t$  cases in Fig. 70, band II in all patients accumulates mostly around the center of the channel. The presence of cells belonging to band IV is higher near the CFL with a crossing point between the curves around  $r/\delta = 0.7$  and  $0.8$ . Nevertheless, band IV of patient 2 is homogeneously distributed in the central zone increasing their concentration near to center of the channel in patient 3 and 4. This behavior of band IV can be related to the presence of band III, that is believed to have an intermediate rigidity [5]. In Table 12, we observe that band volume fraction of band III increases from patient 1 to 3. Meanwhile, the population of band IV is displaced to the central zone from patient 1 to 3. Patient 4 has a low amount of band volume fraction of band II and IV and a high presence of reticulocytes (almost 43% of cell population of band I). Then, both band II and IV, seem to have a similar distribution although the crossing point is still appearing between distribution curves around  $r/\delta = 0.8$ .

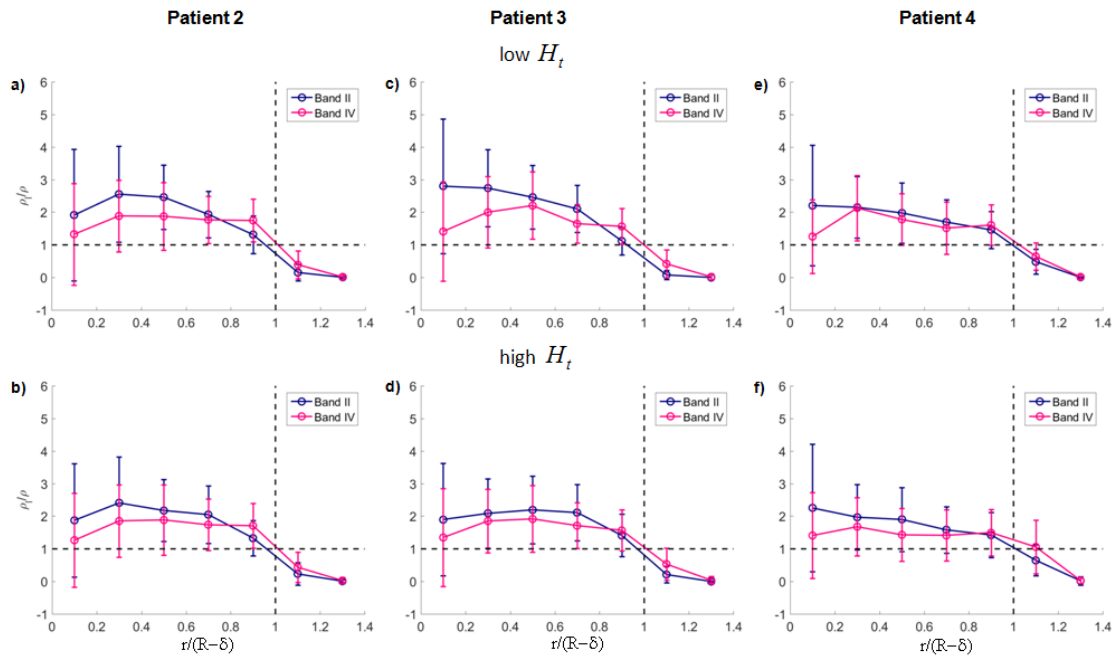


**Fig. 70:** Average cell distribution over all pressure drops of band II and IV flowing in BS at low (first row) high (second row)  $H_t$  for patient 2, 3 and 4.

At high  $H_t$ , band II and IV have a similar behavior. However, a crossing point between bands is again located around  $r/\delta = 0.8$ . A higher presence of cells belonging to band IV near the CFL position is found for all patients, indicating that cells of this band tend to self-marginate under the investigated conditions.

### Role of $H_t$

To compare band II and IV trend as a function of  $H_t$ , distribution curves for both, low and high  $H_t$ , are plotted per patient in Fig.71.

An increase of approximately 7% in  $H_t$  does not produce significant differences in the distribution curves for cells flowing in BS. Even in this case, in analogy with the investigation of  $\Delta P$  effect on cell distribution, the different bands could have reached a steady arrangement in the position chosen for the data acquisition in the tube. An increase in the frequency of collisions due to the increase in hematocrit could accelerate the radial tube positioning of each band. However, this process has not been corroborated in this study.

### Role of aggregation

In this section, the role of aggregation induced by dextran macromolecules and autologous plasma in the bands II and IV distribution, is investigated. In healthy cells, shear rates below  $\bar{\gamma} = 30 \text{ s}^{-1}$  produce strong effects on blood viscosity, mostly because of

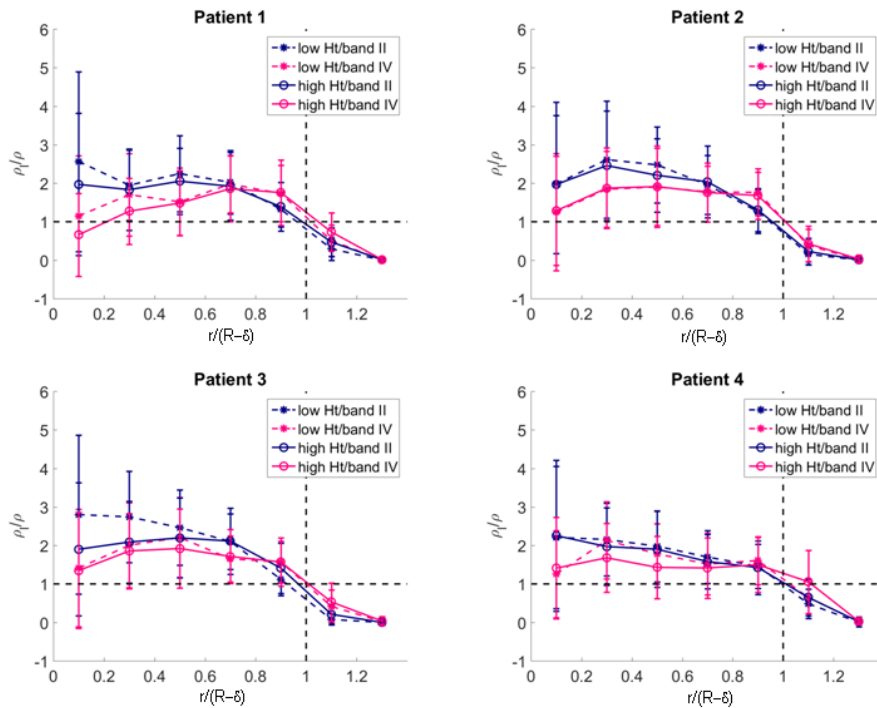


**Fig. 71:** Average cell distribution of band II and IV of cells flowing in BS over all pressure drops at low and high  $H_t$ . Results per patient is presented.

RBC sedimentation and aggregation. In this study, mean shear rates below  $30 \text{ s}^{-1}$  in BS+Dex70 and Plasma suspending media were not explored for the same reason (strong sedimentation on the tubes and reservoir in our experimental setup did not permit accurate measurements). The mean shear rates are higher than  $30 \text{ s}^{-1}$  in all cases (see Table 15).

### 1. BS+Dex70

The distribution curves for patient 1, for different  $\Delta P$  at low and high  $H_t$ , flowing in BS+Dex70 solution, are presented in Fig. 72.

Curves on graph a) in Fig. 72 show that the vast majority of cells is concentrated at the core of the channel at 25 mbar. Due to the low mean shear rate (about  $55 \text{ s}^{-1}$ , see Table 15), aggregation can still have an effect and be the responsible of this distribution. The cells are displaced to the CFL position while the mean shear rate increases, probably due to mitigated aggregation effects between cells. Distributions curves of band II (see b) in Fig. 72) do not show a clear tendency with increasing shear rates.

Increasing  $H_t$  seem to do not intensify significantly the concentration of cells at the core of the channel at 25 and 50 mbar. Differences in  $\Delta P$  at high  $H_t$  in band

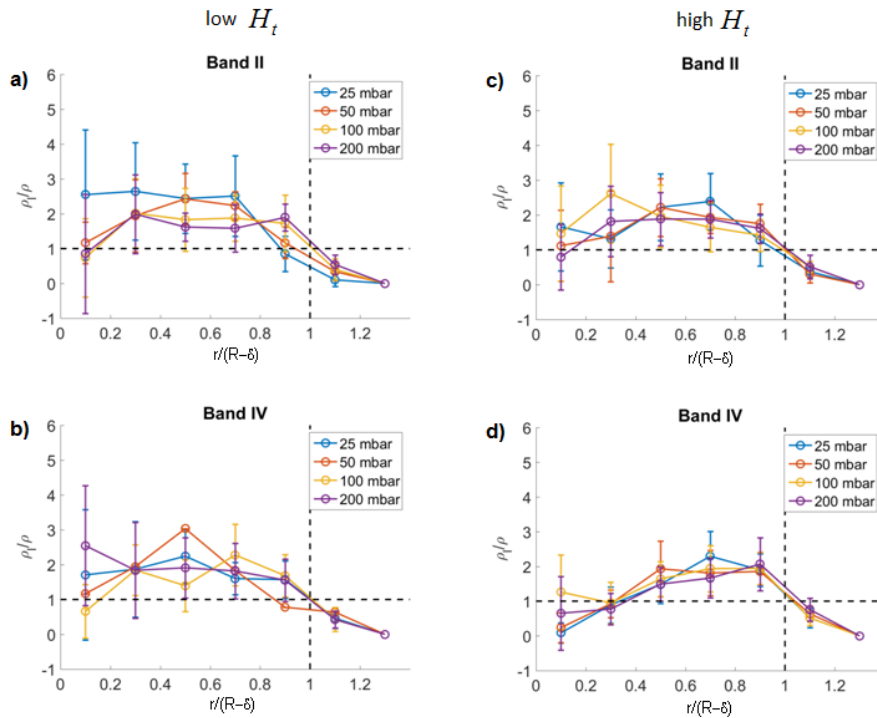


**Fig. 72:** Distribution of cells per pressure drop of band II and IV of patient 1 flowing in BS+Dex70 solution. Results for low (left column) and high (right column)  $H_t$  are presented.

IV, do not produce significant variations on the distribution curves.

In general, no evident variations in band distribution curves are observed depending on  $\Delta P$ . To compare the distribution of cells in BS solutions for both low and high  $H_t$ , the data is averaged for each band (over all  $\Delta P$ ). The results for patients 1, 2 and 3 are presented in Fig. 73.

At low  $H_t$  (see first column in Fig.73) aggregation produces a slight accumulation of cells of both bands in the center of the channel in patient 2 and 3. The effect is more pronounced for patient 3 in the case of band IV. Self-margination of cells observed in BS is inhibited. At high  $H_t$ , no significant differences in the distribution curves are observed in the aggregative and non-aggregative scenarios. In patient 3, the presence of dextran produces an accumulation of cells in the center of the channel in both, band II and IV.

## 2. Plasma

The distribution curves of patient 1 for different  $\Delta P$  at low and high  $H_t$ , flowing in Plasma, is presented in Fig. 74. Similarly to the case previously discussed, no strong variations on the band distribution curves are observed with  $\Delta P$ . Then, to

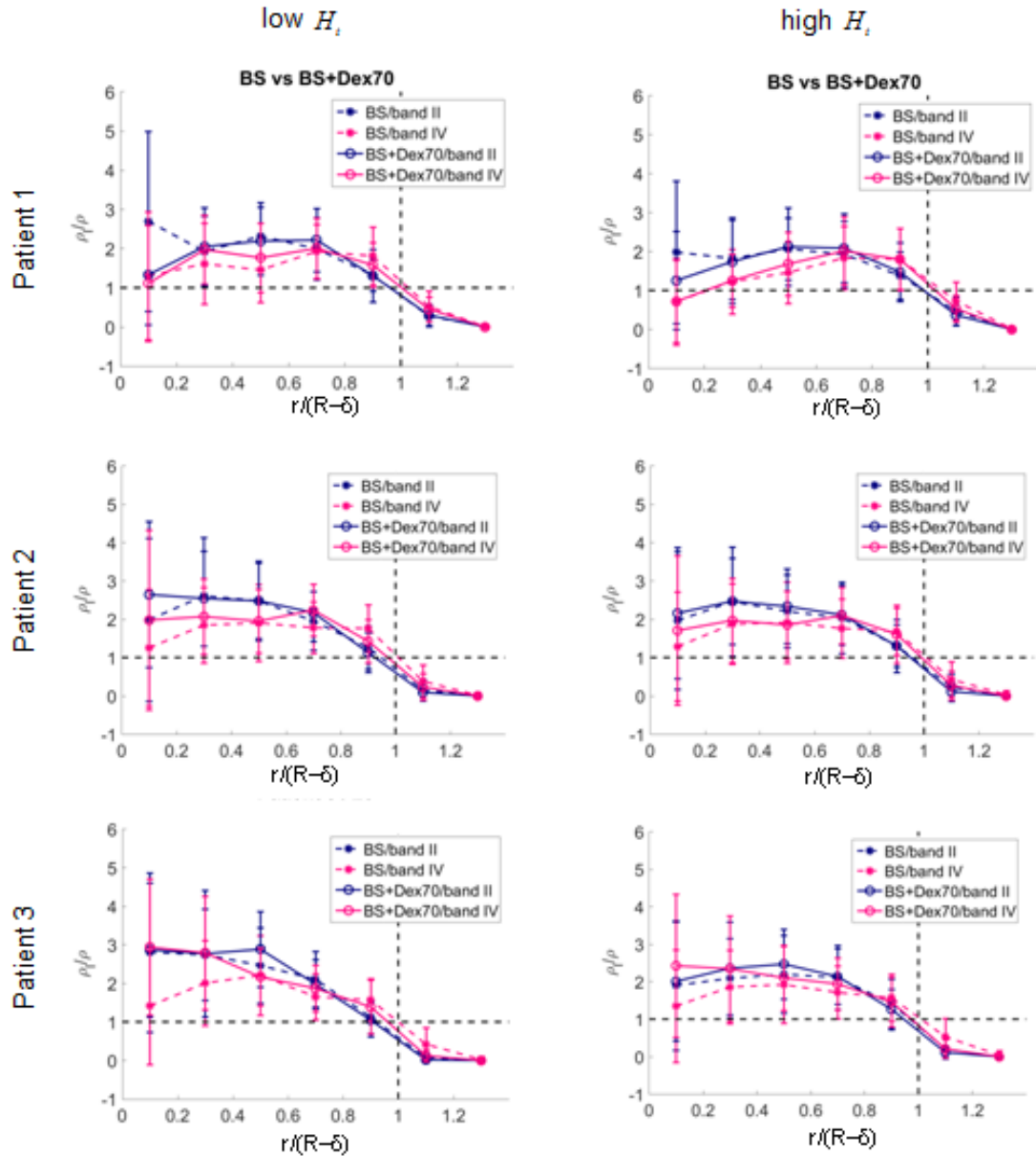


**Fig. 73:** Comparison of the average distribution curves of band II and IV between BS and BS+Dex70 solutions for patients 1, 2 and 3 from top to bottom. Results for low (left column) and high (right column)  $H_t$  are presented.

make a comparison with the distribution of cells flowing in BS solution for both, low and high  $H_t$ , an average over all  $\Delta P$  of the distribution curves is done.

In patient 1, at both low or high  $H_t$  (see first column in Fig. 75), aggregation due to autologous plasma tends to increase the concentration of cells in the center of the channel. However, this tendency is more pronounced at high  $H_t$ . A similar

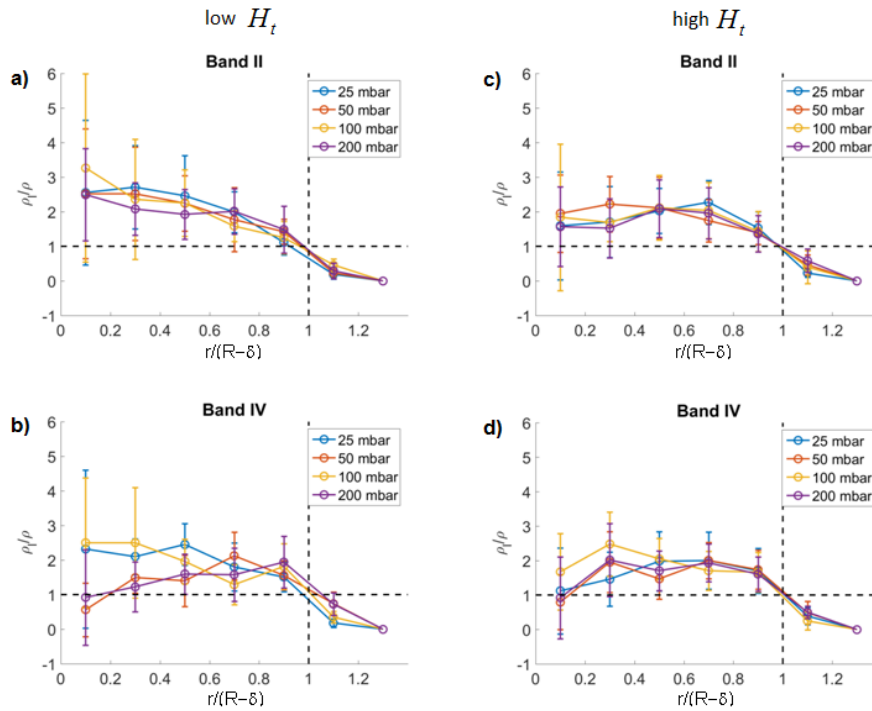


**Fig. 74:** Distribution of cells per pressure drop of band II and IV of patient 1 flowing in autologous Plasma. Results for low (left column) and high (right column)  $H_t$  are presented.

behavior is observed in patient 3. On the other hand, band II and IV display a similar trend, although a crossing point between bands is observed around  $r/\delta = 0.8$ . Then, contrary to what has been observed for cells flowing in BS, and specially at high  $H_t$ , the presence of plasma inhibits the self-margination effect.

Summarizing, the variation concerning cell distribution across the channel tuned by RBC aggregation is different depending on the aggregative factor: cells flowing in BS+Dex70 solution behave differently than flowing in autologous plasma. In the second case, the cells accumulate more in the center compared to the non-aggregative scenario at both, low and high  $H_t$ . Self-margination of band IV is inhibited. On the contrary, a slight variation on band distribution is produced by the presence of dextran compared with the non-aggregative scenario, although this result depends on the patient. Self-margination of band IV is inhibited in some cases. This variations can be due to changes in the viscosity of the suspending media that increases about 70% in BS+Dex70 solution compared to BS, leading to different behavior of the cells under flow. Plasma contains factors that could induce adhesion on cell membrane, as TSP and vWf factors (see Table 4). Both TSP and vWF are increased in sickle cell disease compared to healthy individuals, and they further increase during a vaso-occlusive crisis. Also, the presence of other proteins as fibrinogen in plasma (known to be the main responsible for cell aggregation in blood) could also play a role and help to explain the differences observed in behavior compared to BS+Dex70 solution. It was already observed in Fig. 64 that

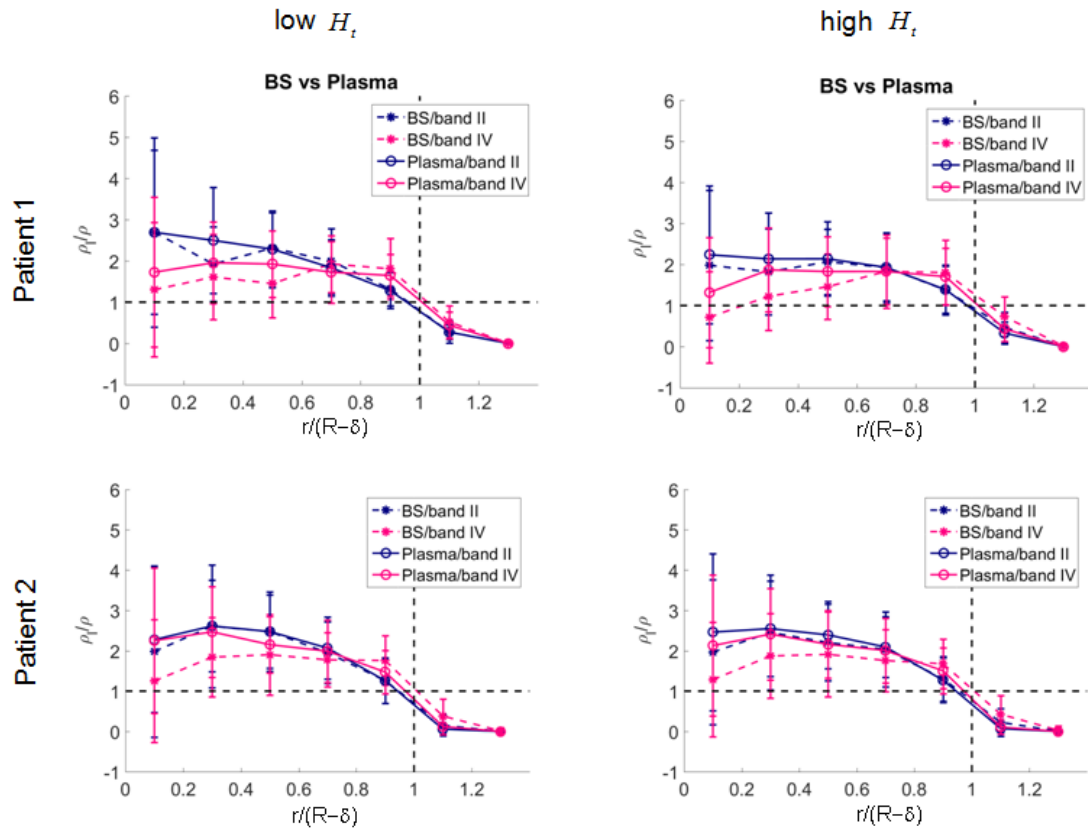


**Fig. 75:** Comparison of the average distribution curves of band II and IV between BS and Plasma solutions for patients 1 and 2 (top to bottom). Results for low (left column) and high (right column)  $H_t$  are presented.

CFL thickness depends on the aggregative factor. Aggregation is more robust in plasma than in dextran. This could explain the similarity on the cell distribution curves between bands in Plasma: the distribution of cells across the channel (independent to their density) could be affected in a similar way due to the presence of plasma.

## 5.4 Conclusion

### Conclusion (english)

Margination is a complex phenomenon, whose mechanism and its main parameters remain unknown for red blood cells (RBCs). These parameters can include tube hematocrit, relative band volume fraction, mechanical properties of cells, channel position, tube diameter, viscosity contrast between the cytosol and suspending medium and the aggregation mechanism between cells. Moreover, in sickle red blood cells (sRBCs) the oxygen level could also play an important role. In this study, channel position, tube diameter, and oxygen level are fixed parameters. An obvious difference in the radial dis-

tribution of different sRBCs populations in the tube where they flow and self-margination to the tube walls of the more dense-rigid cells (also with a different shape) have been observed. However, this behavior seems to depend strongly on the patient. The main reason could be the differences in band volume fraction that vary from patient to patient.

The role of  $\Delta P$  and  $H_t$  on cell distribution was not yet addressed: not considerable changes on cell distribution varying these parameters was detected. We speculate that this behavior could be the result of the choice of the position in the channel where data were acquired (at 1 cm distance to the entrance of the channels). It is possible that this distance is sufficient to achieve a stable relative band distribution. Further experiments need to be done to corroborate this fact. One proposition is to investigate the evolution of the cell distribution of each band, between the entrance and 2 cm onwards the channels, covering the distribution of cells produced at 1 cm.

On the other hand, to have an accurate cell radial distribution, statistic needs to be improved in the experiment (including the amount of data for each experiment and number of patients). The stop flow technique does not allow to have a high enough statistic of the cell radial distribution in a short period of time. Other techniques that include a continuous approach in time on integrating the signal of labeled cells, can be used instead (confocal or two-photon excitation microscopy).

Aggregation seems to inhibit self-margination depending on the aggregative factor: dextran allows self-margination in some patients and inhibits it in others. sRBC aggregates are more robust in plasma than in dextran because of the contribution of both cellular and plasma factors to aggregation when sRBCs are suspended in plasma. sRBCs have been demonstrated to be 4 to 5 times more adherent than healthy RBCs, a process that is mediated by plasma factors [123] and adhesive molecules. Adhesion, as an extra property of the cells flowing in plasma, can produce more robust aggregates in plasma than aggregates formed flowing in dextran.

On the other hand, the cell-free layer (CFL) thickness (Fig. 64) is higher for plasma than dextran. As a consequence, the heterogeneous distribution of cell populations observed in a suspending media without aggregants, is inhibited in sRBCs flowing in plasma. Moreover, it can be speculated that changes in the cell membrane due to the presence of TSP and vWF factors in plasma (towards more or less adhesive) can affect the collisions between the cells when they flow in plasma, and as a consequence, change the cell distribution compared to the cell distribution of cells flowing in solutions without aggregants. Finally, proteins such as fibrinogen (present naturally in plasma) are known to have a different aggregative mechanism compared to dextran, which could also contribute to the differences observed. Additionally, we have explored the case of 20 mg/ml of Dextran 70 knowing from literature [1, 36] that this value induces a similar adhesive interaction energy between cells at physiological values of fibrinogen in healthy patients. Steffen et al. [36], obtained the adhesion energy between cells by atomic force microscopy (AFM) based on Single Cell Force Spectroscopy (SCFS),

while Flormann [1], considered the interaction area between cells and their change in shape (from near flat to a buckling induced sigmoid shape) at different macromolecule concentrations including fibrinogen and dextran. The interaction energy could be different in sRBCs due to their differences in cell membrane composition, shape and rigidity.

Finally, we have observed that the CFL thickness seems to decrease for sRBCs in comparison with the CFL produced by healthy cells under comparable conditions. This result that can be attributed to the increased rigidity of sRBCs compared with healthy ones. In both cases, the addition of dextran do not produce any significant effect on the CFL thickness for the ranges of shear rates explored. The range of shear rate is in general high enough to break the aggregates formed by the presence of dextran. However, this is not be the case of autologous plasma, where aggregates seems to be in general more robust and as a consequence, the thickness of the CFL increases.

An increase in the thickness of the CFL may reduce vascular resistance as discussed in the introduction. However, another physiological consequence would be a change in the nitric oxide (NO) scavenging effect of the RBC core. During flow the scavenging of NO by RBCs in the vessel lumen was greatly reduced in isolated, blood-perfused arterioles, presumably because of the presence of the CFL [150]. This is an interesting consequence that should be considered in the case of sickle cell anemia (SCA), where the presence of NO could be critical in the chain of events that produces vaso-occlusive events (see Chapter 2 for details).

The values obtained for the CFL thickness under different conditions are interesting by themselves for their possible physiological consequences. For our research, the CFL thickness was essential to investigated self-margination of sRBCs as the core of cells was used as a limit of the relative position of the different sRBC populations.

Self-margination in sRBCs has been explored and observed. No investigation on self-margination on healthy cells have been done up to date. A further step on this research will include a higher number of patients, improve statistic on cell distribution, investigate additional channel positions, and investigate self-margination in healthy cells (needed as a control parameter).

## Résumé (français)

La margination est un phénomène complexe, avec un mécanisme et des paramètres principaux qui restent encore inconnus pour les globules rouges (GRs). Ces paramètres peuvent comprendre le taux d'hématocrite dans le tube, la fraction relative de bande volumique, les propriétés mécaniques des cellules, la position du canal, le diamètre du tube, le contraste de viscosité entre le cytosol et le milieu de suspension ainsi que le mécanisme d'agrégation entre les cellules. De plus, le taux d'oxygène dans les globules rouges drépanocytaires (GRDs) peut aussi jouer un rôle important. Dans cette étude,

la position dans le canal, le diamètre du tube et le taux d'oxygène sont fixés. Une différence notable dans la distribution radiale de différentes populations de GRs dans le tube où ils se déplacent et une "automargination" vers les parois du tube, pour les cellules plus denses et rigides (avec des formes différentes) ont été observées. Néanmoins, ce comportement semble être très dépendant du patient.

Le rôle de  $\Delta P$  et  $H_t$  sur la distribution des cellules n'a pas encore été traité : aucun changement considérable sur la distribution des cellules n'a été détecté après variation de ces paramètres. Nous pouvons supposer que ce comportement résulte de la position dans le canal où les données ont été acquises (à 1cm de l'entrée du canal). Il est possible que cette distance soit suffisante pour obtenir une distribution de bande relative stable. D'autres expériences doivent être réalisées pour corroborer ceci. L'une des propositions est d'investiguer l'évolution de la distribution des cellules de chaque bande, entre l'entrée du canal et 2 cm plus loin, couvrant ainsi la distribution de cellules présentes à 1 cm de l'entrée.

D'autre part, dans le but d'avoir une distribution radiale précise des cellules, les statistiques doivent être améliorées dans l'expérience (y compris la quantité de données pour chaque expérience et le nombre de patients). Les techniques dites « stopped-flow » ne permettent pas d'avoir des statistiques suffisantes sur la distribution radiale des cellules pour un temps très court. Une autre technique qui consiste en une approche continue en temps sur l'intégration du signal des cellules marquées peut être utilisée à la place (confocal ou microscopie par excitation à deux photons).

L'agrégation semble inhiber l'automargination en fonction du facteur d'agrégation : le Dextran permet l'automargination chez certains patients et l'inhibe chez les autres. Les agrégats de GRDs sont plus robustes dans le plasma que dans le Dextran à cause de la contribution des cellules et des facteurs du plasma dans l'agrégation, lorsque les GRDs sont resuspendus dans le plasma. Les GRDs ont montré être entre 4 et 5 fois plus adhérents en comparaison avec des patients en bonne santé, processus qui est soumis aux facteurs du plasma [123] et aux molécules adhésives. L'adhésion, en tant que propriété « extra » des cellules se déplaçant dans le plasma, peut produire des agrégats plus robustes dans le plasma que ceux s'écoulant dans le Dextran.

D'autre part, l'épaisseur de la couche sans cellule (CSC) (Fig. 64) est plus importante pour le plasma que pour le Dextran. Par conséquent, la distribution hétérogène des populations de cellules observée dans un milieu de suspension, sans agrégant, est inhibée, pour les GRDs se déplaçant dans le plasma. De plus, nous pouvons supposer que les changements dans la membrane de la cellule dus à la présence de TSP et vWF (plus ou moins adhésifs) peuvent influencer sur les collisions entre les cellules et ainsi produire des mécanismes différents pour les cellules qui se déplacent dans le plasma et en conséquence, changer la distribution des cellules se mouvant dans une solution sans agrégant. Enfin, les protéines telles que les fibrinogènes (naturellement présents dans le plasma) sont connues pour avoir des mécanismes d'agrégation différents en comparaison

au Dextran, ce qui pourrait témoigner des différences observées. De surcroît, nous avons exploré le cas du Dextran 70 à 20mg/ml qui d'après la littérature [36] a pour valeur une énergie d'interaction d'adhésion comparable aux valeurs physiologiques en présence de fibrinogènes chez les patients en bonne santé. Steffen et al. [1, 36] ont obtenu l'énergie d'adhésion entre les cellules par microscopie à force atomique (AFM) basée sur la spectroscopie de force "Single Cell Force Spectroscopy" (SCFS). Flormann [1], dans sa thèse, a considéré la surface d'interaction entre les cellules et les changements de forme (des formes plates aux formes tordues sigmoïdales) à différentes concentrations de macromolécules y compris les fibrinogènes et le Dextran. L'énergie d'interaction peut être différente pour les globules rouges à cause des hétérogénéités dans la composition de la membrane, la forme ou encore la rigidité.

Enfin, l'épaisseur de la CSC semble diminuer pour les GRDs par rapport à la CSC produite par les GRs sains dans des conditions similaires. Ce résultat peut être attribué à la rigidité des GRDs comparés au GRs sains. Dans les deux cas, l'ajout du Dextran ne produit pas d'effet significatif sur l'épaisseur de la CSC, pour l'ensemble des taux de cisaillement exploré. Les taux de cisaillement imposés sont en général suffisants pour rompre les agrégats formés dans le Dextran. Cependant, ce n'est pas le cas pour le plasma autologue, où les agrégats semblent être plus robustes et par conséquent, l'épaisseur de la CSC augmente.

L'augmentation de l'épaisseur de la CSC peut réduire la résistance vasculaire comme nous l'avons spécifié dans l'introduction. Néanmoins, une autre conséquence physiologique peut être provoquée par la trapping de l'acide nitrique (AN) au cœur des GRs. Dans l'écoulement, la fixation de l'AN par les GRs dans la lumière du vaisseau a été considérablement réduite dans les artérioles perfusées et isolées, vraisemblablement à cause de la présence de la CSC [150]. C'est une conséquence intéressante qui doit être considérée dans le cas de l'anémie drépanocytaire, où la présence d'AN peut être critique dans la chaîne des événements qui mène aux crises vaso-occlusives. (Voire Chapitre 2 pour plus de détails).

Les valeurs obtenues pour l'épaisseur de la CSC, dans de différentes conditions, sont intéressantes en elles-mêmes pour leurs possibles implications physiologiques. Dans notre recherche, l'épaisseur de la CSC s'est révélée essentielle dans l'investigation de l'automargination des GRDs, tout comme le cœur de cellules était utilisé en tant que limite de la position relative des différentes populations de GRDs.

L'automargination des globules rouges a été explorée et observée. Aucune investigation en rapport avec l'automargination de cellules saines n'a été effectuée à ce jour. Une future étape de recherche consiste à augmenter le nombre de patients, améliorer les statistiques sur la distribution des cellules, investiguer plus de positions de canaux et l'automargination des cellules saines (nécessaires en tant que paramètre de contrôle).

## Zusammenfassung (deutsch)

Margination ist ein komplexes Phänomen, dessen Wirkungsmechanismus und dessen wesentliche Parameter für rote Blutzellen (RBCs) unbekannt sind. Diese Parameter können den Röhren-Hämatokrit, den relativen Banden-Volumenanteil, die mechanischen Eigenschaften der Zellen, die Kanalposition, den Röhrendurchmesser, den Viskositätsunterschied zwischen Zytosol und dem suspendierenden Medium und den Aggregationsmechanismus zwischen den Zellen beinhalten. Darüber hinaus könnte das Sauerstofflevel für die Margination von sichelförmigen roten Blutzellen (sRBCs) auch eine wichtige Rolle spielen. In dieser Studie sind die Kanalposition, der Röhrendurchmesser und das Sauerstoffniveau fixierte Parameter. Ein offensichtlicher Unterschied zwischen der radialen Verteilung von verschiedenen Grundgesamtheiten von sRBCs in dem Röhren, in dem sie fließen, und Selbst-Margination dichter steiferer Zellen (auch für verschiedene Formen) zu den Wänden des Röhrens wurde beobachtet. Jedoch scheint dieses Verhalten stark vom Patienten abhängig zu sein. Die Hauptursache könnte im Unterschied des Banden-Volumenanteils, der von Patient zu Patient variiert, liegen.

Die Rolle von  $\Delta P$  und  $H_t$  für die Zellverteilung wurde noch nicht angesprochen: Es wurden keine beachtlichen Veränderungen für die Zellverteilung unter Variation dieser Parameter festgestellt. Wir spekulieren, dass dieses Verhalten ein Resultat der Wahl der Position innerhalb des Kanals, an der die Daten erfasst wurden, sein könnte (bei 1 cm Abstand von dem Eingang des Kanals). Es ist möglich, dass dieser Abstand ausreicht, um eine stabile relative Banden-Verteilung zu erreichen. Weitere Experimente sind zur Bestätigung dieses Sachverhalts notwendig. Ein Vorschlag ist es, die Entwicklung der Verteilung der Zellen jeder Bande zwischen Eingang und 2 cm inner halb des Kanals unter Abdeckung der Zellverteilung bei 1 cm zu untersuchen.

Andererseits ist es notwendig die Statistik der Experimente zu verbessern (einschließlich der Anzahl von Daten für jedes Experiment und der Patientenzahl), um eine präzise radiale Zellverteilung zu gewährleisten. Die Methode bei der der Fluss angehalten wird, gewährleistet keine ausreichend gute Statistik der radialen Zellverteilung in einem kurzen Zeitabschnitt. Stattdessen können andere Techniken, die eine kontinuierlich Integration des Signals von mit Fluoreszenzfarbstoff markierten Zellen beinhalten, verwendet werden (Konfokal- oder Zwei-Photonen-Mikroskopie).

Aggregation scheint die Selbst-Margination abhängig von Aggregationsfaktoren zu hemmen: Dextran führt zur Selbst-Margination in einigen Patienten und hemmt diese in anderen. sRBC Aggregate sind in Plasma robuster als in Dextran, weil zelluläre und Plasmafaktoren zur Aggregation beitragen, wenn sRBCs in Plasma suspendiert sind. Es wurde gezeigt, dass sRBCs etwa 4 bis 5 Mal stärker adhären als gesunde RBCs, ein Effekt der durch Plasmafaktoren [123] und adhäsive Moleküle verursacht wird. Adhäsion, als zusätzliche Eigenschaft von in Plasma fließenden Zellen, kann stabilere Aggregate hervorbringen als solche, die sich im Fluss in Dextranlösung formen.

Andererseits ist die Dicke der zell-freien Schicht (ZFS, Fig.64) im Plasma größer als in Dextran. Demzufolge wird die heterogene Verteilung von Zellpopulationen, die in einem suspendierenden Medium ohne Aggregate beobachtet wird, im Fall von sRBCs, die in Plasma fließen, gehemmt.

Zusätzlich kann spekuliert werden, dass Veränderungen der Zellmembran aufgrund der Anwesenheit von TSP und vWF Faktoren im Plasma (gegenübergestellt mehr oder weniger adhäsiv) die Kollisionen zwischen Zellen beeinflussen können, wenn sie im Plasma fließen und als Konsequenz die Zellverteilung verglichen mit der Zellverteilung von Zellen, die in einer Lösung ohne Aggregate fließen, verändern. Schließlich ist bekannt, dass Proteine wie Fibrinogen (das natürliche im Plasma vorkommt), zu Aggregationsmechanismen führen, die sich zu dem von Dextran induzierten unterscheiden, was ebenfalls zu den beobachteten Unterschieden führen könnte. Zusätzlich haben wir den Fall von 20 mg/ml Dextran 70 erforscht, wobei wir aus der Literatur [1, 36] wissen, dass dieser Wert zu einer ähnlichen adhäsiven Interaktionsenergie zwischen Zellen führt, wie physiologische Werte von Fibrinogen im Fall gesunder Patienten. Steffen et al. [36] erhielten die Adhäsionsenergien zwischen den Zellen durch die Nutzung eines Atomkraftmikroskops (AFM) bei Verwendung von Einzelzellkraftspektroskopie (SCFS), während Flormann et al. in seiner Doktorarbeit [1] die Interaktionsbereiche zwischen Zellen und deren Formänderung (von annähernd flach bis hin zu einer buckling-induzierten sigmoidalen Form) in Abhängigkeit verschiedener Makromolekülkonzentrationen einschließlich Fibrinogen und Dextran betrachtete. Die Interaktionsenergien von sRBCs könnten sich auf Grund ihrer Unterschiede in Zellmembran-Komposition, Form und Steifheit unterscheiden.

Schließlich scheint die Dicke der zell-freien Schicht (ZFS) für sRBCs im Vergleich zu der ZFS, die bei gesunden Zellen unter vergleichbaren Bedingungen produziert wird, abzunehmen. Dieses Resultat kann der erhöhten Steifheit der sRBCs verglichen mit gesunden Zellen zugeschrieben werden. In beiden Fällen führt die Zugabe von Dextran nicht zu einem signifikanten Effekt bezogen auf die Dicke der ZFS für die untersuchten Scherratenbereiche. Der Scherratenbereich ist allgemein hoch genug, um Aggregate, die durch die Anwesenheit von Dextran geformt wurden, zu brechen. Aber für autologes Plasma, in dem Aggregate allgemein robuster wirken und als Konsequenz eine Zunahme der Dicke des ZFS beinhalten, ist dies nicht der Fall.

Eine Zunahme der Dicke der ZFS könnte den Gefäßwiderstand reduzieren, wie in der Einleitung diskutiert wurde. Aber eine andere physiologische Konsequenz wäre die Änderung des NO reinigenden Effekts des Bereichs, in dem sich die RBCs befinden (Kern). Während des Flusses wurde die Reinigung von NO durch RBCs im Gefäßlumen deutlich auf isolierte, durchblutete Arteriolen, vermutlich aufgrund der Anwesenheit des ZFS [150], reduziert. Dies ist eine interessante Konsequenz, welche im Fall der SZA, bei der die Anwesenheit von NO kritisch im Bezug auf die Kette von Ereignissen, die vaso-okklusive Ereignisse hervorrufen, ist, Beachtung finden sollte (vergleiche Chapter 2).

Die Werte, die für die Dicke der ZFS unter bestimmten Bedingungen erhalten wurden,

sind für sich selbst genommen im Bezug auf mögliche physiologische Konsequenzen interessant. Für unsere Forschung war die ZFS-Dicke essentiell, um die Selbst-Margination von sRBCs zu untersuchen, da der Kern, als Grenze der relativen Position verschiedener Populationen von sRBCs genutzt wurde.

Selbst-Margination von sRBCs wurde beobachtet und untersucht. Bisher wurden keine Untersuchungen der Selbst-Margination von gesunden Zellen durchgeführt. Ein weiterer Schritt dieser Studie wird eine größere Zahl an Patienten beinhalten, eine verbesserte Statistik der Zellverteilung, Untersuchungen weiterer Kanalpositionen und Untersuchungen der Selbst-Margination gesunder Zellen (notwendig als Kontrollparameter).

# 6 Chapter 6

---

## General conclusion

### General conclusion (english)

Two different phenomena have been addressed in this work in the context of the flow of cells under microcirculatory conditions: the clustering process and the self-margination phenomenon. Interesting results were obtained: cluster formation of healthy RBCs in micro-capillaries under physiological conditions can be a result of a combination of hydrodynamic and macromolecule-induced interactions. Macromolecule-induced interactions can not be fully overcome by shear stresses within the physiological range, and contribute to cluster stability. Aggregated clusters of sickle cells were more robust compared with aggregated clusters of healthy cells. Oxygen starts to be released into the tissues before the capillaries and this is an important factor to consider in the clustering process of sickle cells. This study, has addressed an oxygenated scenario only, giving some hints about the dynamics of the process in both healthy and sickle cells. The pronounced bimodal distribution of the cell-to-cell distances in the hydrodynamic clusters results from changes in the cell shapes. Whether the changes in shape are dynamic due to shape-flow coupling, or due to differences in the physical properties of the cell, remains an unanswered question. To answer this, experiments that will resolve the temporal dynamics of the cluster formation process in direct comparison with three-dimensional simulations are necessary. In the case of sickle cells, a gradient of oxygen content of the channels would be an important factor to consider in further studies as the shape of the cells changes strongly when oxygen is released. However, shape changes of sickle cells have been greatly studied under static conditions and the polymerization process of hemoglobin inside the cells could be affected by the forces exerted by the flow on the cells. Furthermore, it might be worthwhile to do experiments with RBCs that have been separated by density. This yields a separation by age and eventually leads to a more monodisperse distribution of their physical parameters such as the bending rigidity and shear modulus.

Our study on the self-margination phenomenon has shown that, under certain conditions, sickle cells tend to be heterogeneously distributed with more deformable cells accumulating in the channel center while rigid cells accumulate at the external border of the core of the channel where the cells flow. This distribution depends strongly on the patient and the suspending media. More experiments are needed to uncover the important parameters that can lead to a particular distribution. Aggregation seems to inhibit self-margination depending on the aggregative factor: dextran allows self-margination in some patients and inhibits it in others. Plasma inhibits self-margination of cells in all

cases. Plasma is known to contain factors that can induce adhesion on the cell membrane to endothelial cells. The change in the adhesive properties of the cells could play a role in the differences with dextran solution. Moreover, we found that the cell-free layer thickness is higher for plasma than dextran, meaning that the values of shear rate explored in this work seems to be high enough to brake the aggregates formed by the presence of dextran, but not in the case of autologous plasma, where aggregates seems to be more robust. Additionally, it can be speculated that changes in the cell membrane (towards more or less adhesive) can affect the collisions between the cells when they flow in plasma, and as a consequence, change the cell distribution compared to the cell distribution of cells flowing in solutions without aggregates. Heterogeneity of the cell distribution is an important factor to consider in studies of dynamics of cells at the capillary branches.

The comprehension on the behavior of cells at the venule/arteriol level and in capillaries is critical to understand the dynamics of formation of vaso-occlusive events in the case of sickle cell anemia. Further comparison with the behavior of healthy cells is critical to detect abnormalities and correct them in possible future treatments.

## Conclusion générale (français)

Deux différents phénomènes ont été abordés dans ce travail en ce qui concerne la circulation des cellules dans conditions microcirculatoires : le processus d'agrégation et le phénomène d'automargination. Des résultats intéressants ont été obtenus : la formation d'agrégats de GRs sains dans les micro-capillaires, dans des conditions physiologiques saines, peut-être le résultat d'une combinaison des interactions hydrodynamiques et des interactions induites par les macromolécules. Les interactions induites par les macromolécules ne peuvent pas être complètement dominées par les contraintes de cisaillement dans des conditions physiologiques et contribuent à la stabilité des agrégats. Les « clusters » agrégés de GRDs ont été plus résistants par rapport aux agrégats formés par des cellules saines. L'oxygène commence à être libéré dans les tissus avant les capillaires et c'est un facteur important à considérer dans le processus d'agrégation des cellules drépanocytaires. Dans cette étude, nous avons seulement abordé le cas des cellules oxygénées, en donnant quelques indications sur la dynamique des processus, à la fois dans le cas des cellules saines et dans le cas des cellules drépanocytaires. L'origine physique de la distribution bimodale des distances entre les cellules, dans l'hydrodynamique des agrégats vient des changements dans la forme de la cellule. Le fait de savoir si les changements de formes sont dynamiques, grâce au couplage de la forme et du flux, ou grâce à des différences dans les propriétés physiques de la cellule, reste une question sans réponse. Pour répondre à cette question, des expériences permettant de résoudre la dynamique temporelle de processus de la formation d'agrégats en comparaison directe avec des simulations tridimensionnelles sont nécessaires. Dans le cas de cellules drépanocytaires, un gradient de la quantité d'oxygène dans les canaux serait un facteur important à considérer dans des études ultérieures car la forme des cellules change fortement lorsque l'oxygène est libéré. Néanmoins, les changements

de forme des cellules drépanocytaires ont été largement étudiés dans des conditions statiques et le processus de polymérisation de l'hémoglobine à l'intérieur des cellules peut être affecté par les forces exercées par l'écoulement sur les cellules. En outre, il pourrait être intéressant de faire des expériences avec des globules rouges qui ont été séparés par densité. Cela aboutit à une séparation par âge et conduit finalement à une distribution monodispersée des paramètres physiques des cellules, tels que la rigidité à la flexion et le module de cisaillement.

Notre étude sur le phénomène d'automargination a montré que, sous certaines conditions, les cellules drépanocytaires ont tendance à avoir une distribution hétérogène avec des cellules déformables s'accumulant au centre du canal alors que les cellules rigides s'accumulent à la frontière extérieure du cœur de cellules s'écoulant dans le canal. Cette distribution dépend fortement du patient et du milieu de suspension. D'autres expériences sont nécessaires pour dévoiler les paramètres principaux qui mènent à une distribution particulière. L'agrégation semble inhiber l'automargination en fonction du facteur d'agrégation : le Dextran permet l'automargination chez certains patients et la diminue chez d'autres. Le plasma réduit l'automargination des cellules dans tous les cas. Celui-ci est connu pour contenir des facteurs qui induisent l'adhésion de la membrane des cellules sur les cellules endothéliales. Le changement des propriétés d'adhésion des cellules pourrait jouer un rôle sur différentes solutions de Dextran. De plus, nous avons trouvé que l'épaisseur de la couche sans cellule est plus grande pour le plasma par rapport au Dextran et le taux de cisaillement minimal pour rompre les agrégats dans le plasma est plus grand que dans le Dextran. Les valeurs des taux de cisaillement explorées dans cette étude, sont en général suffisantes pour casser les agrégats formés en présence de Dextran mais insuffisantes pour rompre ceux formés dans du plasma autologue. En outre, nous pouvons supposer que des changements dans la membrane de la cellule (plus ou moins adhésifs) peuvent affecter les collisions entre les cellules quand elles se déplacent dans du plasma, et par conséquent, changer la distribution des cellules se mouvant dans des solutions sans agrégant. L'hétérogénéité de la distribution des cellules est un facteur important à considérer dans les études de dynamique des cellules dans le réseau microvasculaire.

La compréhension du comportement des cellules au niveau des veinules/artérioles et dans les capillaires est critique, dans le cas de la drépanocytose, pour comprendre la dynamique des crises vaso-occlusives. Une comparaison ultérieure avec le comportement des cellules saines est essentielle pour détecter les anomalies et essayer de les corriger au cours des traitements.

## **Generelle Zusammenfassung (deutsch)**

In dieser Arbeit wurden zwei Phänomene des Zellflusses unter mikrozirkulatorischen Bedingungen untersucht: Der Aggregationsprozess und das Phänomen der Selbst-Margination. Hierbei wurden interessante Resultate erzielt: Die Formation von Aggregation gesunder

RBCs in Mikrokapillaren unter physiologischen Bedingungen kann das Resultat einer Kombination aus hydrodynamischen und makromolekül-induzierten Interaktionen sein. Makromolekül-induzierte Interaktionen können innerhalb des Bereichs physiologischer Schubspannungen nicht vollständig überwunden werden und tragen zur Stabilisierung von Aggregaten bei. Aggregate bestehend aus Sichelzellen waren robuster als Aggregate, die von gesunden Zellen geformt wurden. Sauerstoff wird schon vor Kapillaren an Gewebe abgegeben, was ein wichtiger Faktor bei Erwägungen zum Aggregationsprozess bei Sichelzellen ist. In dieser Studie wurde ausschließlich ein sauerstoffreiches Szenario untersucht, was Hinweise auf die Prozessdynamiken sowohl für gesunde als auch für Sichelzellen lieferte. Die ausgeprägte bimodale Verteilung der Zell-Zell-Abstände für hydrodynamische Aggregate ergibt sich wegen der Formänderung der Zellen. Ob die Formänderungen dynamisch aufgrund einer Form-Fluss Kopplung zu erklären sind, oder aufgrund von Unterschieden in den physikalischen Eigenschaften der Zellen, bleibt eine unbeantwortete Frage. Um diese zu beantworten, sind Experimente notwendig, welche die zeitliche Dynamik des Aggregationsprozesses direkt mit dreidimensionalen Simulationen vergleichen. Im Fall von Sichelzellen wäre die Berücksichtigung von Sauerstoffgradienten in den Kanälen ein wichtiger Faktor in zukünftigen Studien, da sich die Form der Zellen deutlich verändert, wenn Sauerstoff freigegeben wird. Aber Formänderungen von Sichelzellen wurden unter statischen Konditionen bereits intensiv studiert, wobei der Polymerisationsprozess von Hämoglobin in der Zelle durch Kräfte, die während des Flusses auf Zellen ausgeübt werden, beeinflusst werden könnten. Darüber hinaus könnte es erstrebenswert sein Experimente mit roten Blutzellen, die mit Hilfe ihrer Dichte separiert wurden, durchzuführen. Dies führt zu einer altersabhängigen Separation und demzufolge einer monodisperseren Verteilung der physikalischen Parameter, wie beispielsweise der Biegesteifigkeit und des Schermoduls.

Unsere Studie über das Selbst-Marginations-Phänomen hat gezeigt, dass Sichelzellen unter bestimmten Bedingungen dazu neigen heterogen verteilt zu sein, wobei deformierbare Zellen eher in der Mitte und steifere Zellen, die durch den Kanal fließen, eher an der Aussenseite zu finden sind. Mehr Experimente sind notwendig, um die wichtigen Parameter, die zu einer bestimmten Verteilung führen, zu identifizieren. Abhängig vom Aggregationsfaktor scheint die Aggregation die Selbst-Margination zu hemmen: Dextran erlaubt Selbst-Margination in einigen Fällen und hemmt sie in anderen. Plasma hemmt die Selbst-Margination von Zellen in allen Fällen. Plasma ist dafür bekannt, dass es Faktoren enthält, welche die Adhäsion der Zellmembranen an Endothelzellen begünstigen können. Die Änderung der Adhäsionseigenschaften der Zellen könnte für verschiedene Dextranlösungen eine Rolle spielen. Darüber hinaus haben wir festgestellt, dass die Dicke der zell-freien Schicht für Plasma größer ist als für Dextran und dass die minimale Scherrate, die notwendig ist um die Aggregate zu brechen, in Plasma höher ist als in Dextran. Die Werte der Scherraten, die in dieser Arbeit erforscht wurden sind allgemein groß genug um Aggregate, die durch Dextran entstanden sind, zu brechen, aber sie sind nicht groß genug um Aggregate, die durch autologes Plasma entstanden sind, zu brechen. Zusätzlich kann spekuliert werden, dass Änderungen der Zellmembran (gegenübergestellt mehr oder weniger adhäsiv) die Kollisionen zwischen Zellen, beim

Fluss im Plasma und als Konsequenz eine Änderung der Zellverteilung verglichen mit der Zellverteilung von Zellen, die in einer Lösung ohne Aggregate fließen, beeinflussen können. Die Heterogenität der Zellverteilung ist ein wichtiger zu bedenkender Faktor bei Studien der Zelldynamiken und Kapillarzweigen.

Das Verständniss des Verhaltens von Zellen auf venoler/arterioler Ebene und in Kapillaren ist notwendig, um die Dynamik von vasco-okklusiven Ereignissen im Fall von Sichelzellenanämie begreifen zu können. Der Vergleich mit dem Verhalten von gesunden Zellen ist wichtig, um Abnormalitäten festzustellen und in möglichen zukünftigen Behandlungen zu korrigieren.



# 7 Chapter 7

---

## List of publications

1. **V. Clavería**, O. Aouane, M. Thiebaud, M. Abkarian, G. Coupier, C. Misbah, T. John, and C. Wagner. Clusters of red blood cells in microcapillary flow: hydrodynamic versus macromolecule induced interaction. *Soft Matter*, 12:8235–8245, 2016.
2. L. Lanotte, J. Mauer, S. Mendez, D. A. Fedosov, J.-M. Fromental, **V. Clavería**, F. Nicoud, G. Gompper, and M. Abkarian. Red cells' dynamic morphologies govern blood shearthinning under microcirculatory flow conditions. *Proceedings of the National Academy of Sciences*, 2016.
3. **V. Clavería**, L. Lanotte, C. Renoux, P. Joly, G. Cannas, A. Gauthier, C. Wagner, P. Connes, and M. Abkarian. Possible Self-margination of sickle red blood cells suspensions in glass capillaries. *In preparation*.
4. **V. Clavería**, P. Connes, C. Renoux, P. Joly, G. Cannas, A. Gauthier, C. Wagner, and M. Abkarian. Clustering of sickle red blood cells under normoxia in microcapillary flow. *In preparation*.



# Bibliography

- [1] D. Flormann. *Physical characterization of red blood cell aggregation*. Saarland University, 2017.
- [2] V. Claveria, O. Aouane, M. Thiebaud, M. Abkarian, G. Coupier, C. Misbah, T. John, and C. Wagner. Clusters of red blood cells in microcapillary flow: hydrodynamic versus macromolecule induced interaction. *Soft Matter*, 12:8235–8245, 2016.
- [3] W. G. Wood. Haemoglobin synthesis during human fetal development. *Br. Med. Bull.*, 32(3):282–287, Sep 1976.
- [4] W. A. Eaton and J. Hofrichter. Sick cell hemoglobin polymerization. *Adv. Protein Chem.*, 40:63–279, 1990.
- [5] E. Evans, N. Mohandas, and A. Leung. Static and dynamic rigidities of normal and sickle erythrocytes. Major influence of cell hemoglobin concentration. *J. Clin. Invest.*, 73(2):477–488, Feb 1984.
- [6] O. Baskurt, B. Neu, and H.J. Meiselman. *Red blood cell aggregation*. CRC Press, 2011.
- [7] M. Abkarian and A. Viallat. Chapter 10 on the importance of the deformability of red blood cells in blood flow. In *Fluid-Structure Interactions in Low-Reynolds-Number Flows*, pages 347–462. The Royal Society of Chemistry, 2016.
- [8] J. Tripette, T. Alexy, M. D. Hardy-Dessources, D. Mougénel, E. Beltan, T. Chalabi, R. Chout, M. Etienne-Julan, O. Hue, H. J. Meiselman, and P. Connes. Red blood cell aggregation, aggregate strength and oxygen transport potential of blood are abnormal in both homozygous sickle cell anemia and sickle-hemoglobin C disease. *Haematologica*, 94(8):1060–1065, Aug 2009.
- [9] D. K. Kaul, E. Finnegan, and G. A. Barabino. Sick cell-red cell-endothelium interactions. *Microcirculation*, 16(1):97–111, Jan 2009.
- [10] J.P. Shelby, J. White, K. Ganesan, P.K. Rathod, and D.T. Chiu. A microfluidic model for single-cell capillary obstruction by plasmodium falciparum-infected erythrocytes. *Proceedings of the National Academy of Sciences*, 100(25):14618–14622, 2003.

- [11] A.S. Popel and P.C. Johnson. Microcirculation and hemorheology. *Annual Review of Fluid Mechanics*, 37(1):43–69, 2005.
- [12] B. Alberts, A. Johnson, J. Lewis, M. Raff, K. Roberts, and P. Walter. *Molecular biology of the cell*. 2002.
- [13] R. Fåhræus. Die strömungsverhältnisse und die verteilung der blutzellen im gefäßsystem. *Journal of Molecular Medicine*, 7(3):100–106, 1928.
- [14] M. Bessis. Erythroblastic island, functional unity of bone marrow. *Revue d'hématologie*, 13(1):8–11, 1957.
- [15] M.C. Bessis and J. Breton-Gorius. Iron metabolism in the bone marrow as seen by electron microscopy: A critical review. *Blood*, 19(6):635–663, 1962.
- [16] X. An and N. Mohandas. Erythroblastic islands, terminal erythroid differentiation and reticulocyte maturation. *International Journal of Hematology*, 93(2):139–143, 2011.
- [17] G. Lim H. W., M. Wortis, and R. Mukhopadhyay. Stomatocyte–discocyte–echinocyte sequence of the human red blood cell: Evidence for the bilayer– couple hypothesis from membrane mechanics. *Proceedings of the National Academy of Sciences*, 99(26):16766–16769, 2002.
- [18] H.W. Lim, M. Wortis, R. Mukhopadhyay, et al. Red blood cell shapes and shape transformations: newtonian mechanics of a composite membrane: sections 2.1–2.4. *Soft Matter, Volume 4: Lipid Bilayers and Red Blood Cells*, pages 83–139, 2009.
- [19] M. Diez-Silva, M. Dao, J. Han, C.-T. Lim, and S. Suresh. Shape and biomechanical characteristics of human red blood cells in health and disease. *MRS Bulletin*, 35(05):382–388, 2010.
- [20] Y.C. Fung. *Biomechanics, mechanical properties of living tissues*. Springer-Verlag New York, 1993.
- [21] E. Evans and Y.-C. Fung. Improved measurements of the erythrocyte geometry. *Microvascular research*, 4(4):335–347, 1972.
- [22] O. Linderkamp and H.J. Meiselman. Geometric, osmotic, and membrane mechanical properties of density- separated human red cells. *Blood*, 59(6):1121–1127, 1982.
- [23] J.M. Werre, F.L. Willekens, F.H. Bosch, L.D. de Haans, S.G. van der Vegt, A.G. van den Bos, and G.J. Bosman. The red cell revisited—matters of life and death. *Cellular and molecular biology (Noisy-le-Grand, France)*, 50(2):139—145, March 2004.

- [24] H.U. Lutz, S.C. Liu, and J. Palek. Release of spectrin-free vesicles from human erythrocytes during atp depletion: 1. characterization of spectrin-free vesicles. *The Journal of Cell Biology*, 73(3):548–560, 1977.
- [25] J.E. Squires. Artificial blood. *Science*, 295(5557):1002–1005, 2002.
- [26] H. Volkmar, R. Ken, M. Narla, and E. Evan. Elastic thickness compressibility of the red cell membrane. *Biophysical Journal*, 81(3):1452 – 1463, 2001.
- [27] R. Dimova, S. Aranda, N. Bezlyepkina, V. Nikolov, K. A Riske, and R. Lipowsky. A practical guide to giant vesicles. probing the membrane nanoregime via optical microscopy. *Journal of Physics: Condensed Matter*, 18(28):S1151, 2006.
- [28] E. Evans and A. Yeung. Hidden dynamics in rapid changes of bilayer shape. *Chemistry and Physics of Lipids*, 73(1):39 – 56, 1994.
- [29] R. Skalak, A. Tozeren, R.P. Zarda, and S. Chien. Strain energy function of red blood cell membranes. *Biophysical Journal*, 13(3):245, 1973.
- [30] E.A. Evans. Structure and deformation properties of red blood cells: concepts and quantitative methods. *Meth. Enzymol.*, 173:3–35, 1989.
- [31] W. Helfrich. Elastic Properties of Lipid Bilayers: Theory and Possible Experiments. *Z. Naturforsch.*, 28c:693–703, 1973.
- [32] H.L. Goldsmith. The microrheology of red blood cell suspensions. *J. Gen. Physiol.*, 52(1):5–28, Jul 1968.
- [33] S. Asakura and F. Oosawa. Interaction between particles suspended in solutions of macromolecules. *Journal of Polymer Science*, 33(126):183–192, 1958.
- [34] B. Neu and H.J. Meiselman. Depletion-mediated red blood cell aggregation in polymer solutions. *Biophysical Journal*, 83(5):2482–2490, 2002.
- [35] K. Buxbaum, E. Evans, and D.E. Brooks. Quantitation of surface affinities of red blood cells in dextran solutions and plasma. *Biochemistry*, 21(13):3235–3239, 1982.
- [36] P. Steffen, C. Verdier, and C. Wagner. Quantification of depletion-induced adhesion of red blood cells. *Physical Review Letters*, 110(1):018102, 2013.
- [37] M. Brust, O. Aouane, M. Thiébaud, D. Flormann, C. Verdier, L. Kaestner, MW Laschke, H. Selmi, A. Benyoussef, T. Podgorski, G. Coupier, C. Misbah, and C. Wagner. The plasma protein fibrinogen stabilizes clusters of red blood cells in microcapillary flows. *Scientific Reports*, 4:4348, 2014.
- [38] S. Chien. Biophysical Behaviour of Suspensions, in the Red Blood Cell. pages 1031–1133. D.M. Surgenor, 1975.

- [39] N. Maeda and T. Shiga. Opposite effect of albumin on the erythrocyte aggregation induced by immunoglobulin g and fibrinogen. *Biochimica et Biophysica Acta (BBA)-Biomembranes*, 855(1):127–135, 1986.
- [40] R. Fantoni, A. Giacometti, and A. Santos. Bridging and depletion mechanisms in colloid-colloid effective interactions: A reentrant phase diagram. *The Journal of chemical physics*, 142(22):224905, 2015.
- [41] H.L Goldsmith and S.G Mason. The flow of suspensions through tubes. i. single spheres, rods, and discs. *Journal of Colloid Science*, 17(5):448 – 476, 1962.
- [42] C. E. Chaffey, H. Brenner, and S. G. Mason. Particle motions in sheared suspensions. *Rheologica Acta*, 4(1):56–63, 1965.
- [43] J. R. Smart and D. T. Leighton Jr. Measurement of the drift of a droplet due to the presence of a plane. *Physics of Fluids A: Fluid Dynamics*, 3(1):21–28, 1991.
- [44] M. Abkarian and A. Viallat. Dynamics of vesicles in a wall-bounded shear flow. *Biophysical journal*, 89(2):1055–1066, 2005.
- [45] M. Abkarian, C. Lartigue, and A. Viallat. Tank treading and unbinding of deformable vesicles in shear flow: Determination of the lift force. *Phys. Rev. Lett.*, 88:068103, Jan 2002.
- [46] N. Callens, C. Minetti, G. Coupier, M.-A. Mader, F. Dubois, C. Misbah, and T. Podgorski. Hydrodynamic lift of vesicles under shear flow in microgravity. *EPL (Europhysics Letters)*, 83(2):24002, 2008.
- [47] R. Skalak, N. Ozkaya, and T. C. Skalak. Biofluid mechanics. *Annual review of fluid mechanics*, 21(1):167–200, 1989.
- [48] R. Fåhræus and T. Lindqvist. The viscosity of the blood in narrow capillary tubes. *American Journal of Physiology – Legacy Content*, 96(3):562–568, 1931.
- [49] E.C. Eckstein, A.W. Tilles, and F.J. Millero. Conditions for the occurrence of large near-wall excesses of small particles during blood flow. *Microvasc. Res.*, 36(1):31–39, Jul 1988.
- [50] D. Leighton and A. Acrivos. The shear-induced migration of particles in concentrated suspensions. *Journal of Fluid Mechanics*, 181:415–439, August 1987.
- [51] Rui L., Takuji I., Yohsuke I., Motohiro T., Shigeo W., and Takami Y. Radial dispersion of red blood cells in blood flowing through glass capillaries: The role of hematocrit and geometry. *Journal of Biomechanics*, 41(10):2188 – 2196, 2008.
- [52] C. Pozrikidis. Boundary integral and singularity methods for linearized viscous flow. 1992. *Cambridge UP, Cambridge*.

- [53] N. Liron and S. Mochon. Stokes flow for a stokeslet between two parallel flat plates. *Journal of Engineering Mathematics*, 10(4):287–303, 1976.
- [54] M. Thiébaud and C. Misbah. Rheology of a vesicle suspension with finite concentration: A numerical study. *Phys. Rev. E*, 88:062707, Dec 2013.
- [55] O. Aouane, M. Thiébaud, A. Benyoussef, C. Wagner, and C. Misbah. Vesicle dynamics in a confined poiseuille flow: From steady state to chaos. *Phys. Rev. E*, 90:033011, Sep 2014.
- [56] M. Thiébaud, Z. Shen, J. Harting, and C. Misbah. Prediction of anomalous blood viscosity in confined shear flow. *Physical Review Letters*, 112(23):238304, 2014.
- [57] Y. Suzuki, N. Tateishi, M. Soutani, and N. Maeda. Flow behavior of erythrocytes in microvessels and glass capillaries: effects of erythrocyte deformation and erythrocyte aggregation. *International Journal of Microcirculation*, 16(4):187–194, 1996.
- [58] S. Chien, S. Usami, R.J. Dellenback, and M.I. Gregersen. Blood viscosity: Influence of erythrocyte deformation. *Science*, 157(3790):827–829, 1967.
- [59] L. Lanotte, J. Mauer, S. Mendez, D.A. Fedosov, V. Fromental, J.-M. and Claveria, F. Nicoud, G. Gompper, and M. Abkarian. Red cells' dynamic morphologies govern blood shear thinning under microcirculatory flow conditions. *Proceedings of the National Academy of Sciences*, 2016.
- [60] H. L. Goldsmith, G. R. Cokelet, P. Gaehtgens, and R. Fahraeus. Robin Fåhræus: evolution of his concepts in cardiovascular physiology. *Am. J. Physiol.*, 257(3 Pt 2):H1005–1015, Sep 1989.
- [61] A. R. Pries, T. W. Secomb, and P. Gaehtgens. Biophysical aspects of blood flow in the microvasculature. *Cardiovasc. Res.*, 32(4):654–667, Oct 1996.
- [62] D. A. Fedosov and G. Gompper. White blood cell margination in microcirculation. *Soft Matter*, 10:2961–2970, 2014.
- [63] G. J. Tangelder, H. C. Teirlinck, D. W. Slaaf, and R. S. Reneman. Distribution of blood platelets flowing in arterioles. *Am. J. Physiol.*, 248(3 Pt 2):H318–323, Mar 1985.
- [64] J. C. Firrell and H. H. Lipowsky. Leukocyte margination and deformation in mesenteric venules of rat. *Am. J. Physiol.*, 256(6 Pt 2):H1667–1674, Jun 1989.
- [65] A. Jain and L. L. Munn. Biomimetic postcapillary expansions for enhancing rare blood cell separation on a microfluidic chip. *Lab Chip*, 11(17):2941–2947, Sep 2011.

- [66] S. S. Shevkoplyas, T. Yoshida, L. L. Munn, and M. W. Bitensky. Biomimetic autoseparation of leukocytes from whole blood in a microfluidic device. *Anal. Chem.*, 77(3):933–937, Feb 2005.
- [67] D.A. Fedosov, J. Fornleitner, and G. Gompper. Margination of white blood cells in microcapillary flow. *Phys. Rev. Lett.*, 108:028104, Jan 2012.
- [68] J. B. Freund. Leukocyte margination in a model microvessel. *Physics of Fluids*, 19(2):023301, 2007.
- [69] A. Jain and L. L. Munn. Determinants of leukocyte margination in rectangular microchannels. *PLOS ONE*, 4(9):1–8, 09 2009.
- [70] H. Zhao, E. S. G. Shaqfeh, and V. Narsimhan. Shear-induced particle migration and margination in a cellular suspension. *Physics of Fluids*, 24(1):011902, 2012.
- [71] L. Crowl and A. L. Folgelson. Analysis of mechanisms for platelet near-wall excess under arterial blood flow conditions. *Journal of Fluid Mechanics*, 676:348–375, 2011.
- [72] H. L. Goldsmith and S. Spain. Margination of leukocytes in blood flow through small tubes. *Microvasc. Res.*, 27(2):204–222, Mar 1984.
- [73] G.B. Nash, T. Watts, C. Thornton, and M. Barigou. Red cell aggregation as a factor influencing margination and adhesion of leukocytes and platelets. *Clinical hemorheology and microcirculation*, 39(1–4):303–310, 2008.
- [74] A. W. Tilles and E. C. Eckstein. The near-wall excess of platelet-sized particles in blood flow: its dependence on hematocrit and wall shear rate. *Microvasc. Res.*, 33(2):211–223, Mar 1987.
- [75] P. A. Aarts, S. A. van den Broek, G. W. Prins, G. D. Kuiken, J. J. Sixma, and R. M. Heethaar. Blood platelets are concentrated near the wall and red blood cells, in the center in flowing blood. *Arteriosclerosis*, 8(6):819–824, 1988.
- [76] H. Zhao and E. S. Shaqfeh. Shear-induced platelet margination in a microchannel. *Phys Rev E Stat Nonlin Soft Matter Phys*, 83(6 Pt 1):061924, Jun 2011.
- [77] D. A. Reasor, M. Mehrabadi, D. N. Ku, and C. K. Aidun. Determination of critical parameters in platelet margination. *Ann Biomed Eng*, 41(2):238–249, Feb 2013.
- [78] Rafael G. Henríquez R., K. Sinha, and M.D. Graham. Margination regimes and drainage transition in confined multicomponent suspensions. *Phys. Rev. Lett.*, 114:188101, May 2015.
- [79] A. Kumar and M.D. Graham. Mechanism of margination in confined flows of blood and other multicomponent suspensions. *Phys. Rev. Lett.*, 109:108102, Sep 2012.

- [80] A. Kumar and M. D. Graham. Segregation by membrane rigidity in flowing binary suspensions of elastic capsules. *Phys. Rev. E*, 84:066316, Dec 2011.
- [81] A. Kumar, R. G. Henríquez Rivera, and M. D. Graham. Flow-induced segregation in confined multicomponent suspensions: effects of particle size and rigidity. *Journal of Fluid Mechanics*, 738:423–462, Jan 2014.
- [82] K. Sinha and M. D. Graham. Shape-mediated margination and demargination in flowing multicomponent suspensions of deformable capsules. *Soft Matter*, 12:1683–1700, 2016.
- [83] K. D. Young. The selective value of bacterial shape. *Microbiol. Mol. Biol. Rev.*, 70(3):660–703, Sep 2006.
- [84] Y. Geng, P. Dalhaimer, S. Cai, R. Tsai, M. Tewari, T. Minko, and D. E. Discher. Shape effects of filaments versus spherical particles in flow and drug delivery. *Nat Nanotechnol*, 2(4):249–255, Apr 2007.
- [85] J.A. Champion and S. Mitragotri. Role of target geometry in phagocytosis. *Proceedings of the National Academy of Sciences of the United States of America*, 103(13):4930–4934, 2006.
- [86] H. W. Hou, A. A. Bhagat, A. G. Chong, P. Mao, K. S. Tan, J. Han, and C. T. Lim. Deformability based cell margination—a simple microfluidic design for malaria-infected erythrocyte separation. *Lab Chip*, 10(19):2605–2613, Oct 2010.
- [87] B. M. Cooke, F. K. Glenister, N. Mohandas, and R. L. Coppel. Assignment of functional roles to parasite proteins in malaria-infected red blood cells by competitive flow-based adhesion assay. *Br. J. Haematol.*, 117(1):203–211, Apr 2002.
- [88] M. M. Guest, T. P. Bond, R. G. Cooper, and J. R. Derrick. Red blood cells: change in shape in capillaries. *Science*, 142(3597):1319–1321, Dec 1963.
- [89] R. Skalak and P.I. Branemark. Deformation of red blood cells in capillaries. *Science*, 164(3880):717–719, 1969.
- [90] P. Gaehtgens, C. Duhrssen, and K. H. Albrecht. Motion, deformation, and interaction of blood cells and plasma during flow through narrow capillary tubes. *Blood Cells*, 6(4):799–817, 1980.
- [91] U. Bagge, P. I. Branemark, R. Karlsson, and R. Skalak. Three-dimensional observations of red blood cell deformation in capillaries. *Blood Cells*, 6(2):231–239, 1980.
- [92] K. Kubota, J. Tamura, T. Shirakura, M. Kimura, K. Yamanaka, T. Isozaki, and I. Nishio. The behaviour of red cells in narrow tubes in vitro as a model of the microcirculation. *Br. J. Haematol.*, 94(2):266–272, Aug 1996.

- [93] M. Abkarian, M. Faivre, and H. A. Stone. High-speed microfluidic differential manometer for cellular-scale hydrodynamics. *Proc. Natl. Acad. Sci. U.S.A.*, 103(3):538–542, Jan 2006.
- [94] G. Tomaiuolo, L. Lanotte, R. D’Apolito, A. Cassinese, and S. Guido. Microconfined flow behavior of red blood cells. *Med Eng Phys*, 38(1):11–16, Jan 2016.
- [95] A. V Kyrylyuk, M. C. Hermant, T. Schilling, B. Klumperman, C. E Koning, and P. Van der Schoot. Controlling electrical percolation in multicomponent carbon nanotube dispersions. *Nature nanotechnology*, 6(6):364–369, 2011.
- [96] M. Radu and T. Schilling. Hydrodynamic interactions of colloidal spheres under shear flow. *arXiv preprint arXiv:1203.3441*, 2012.
- [97] M. Radu and T. Schilling. Solvent hydrodynamics speed up crystal nucleation in suspensions of hard spheres. *EPL (Europhysics Letters)*, 105(2):26001, 2014.
- [98] B. Cui, H. Diamant, B. Lin, and S. A Rice. Anomalous hydrodynamic interaction in a quasi-two-dimensional suspension. *Physical Review Letters*, 92(25):258301, 2004.
- [99] T. Beatus, R. Bar-Ziv, and T. Tlusty. Anomalous microfluidic phonons induced by the interplay of hydrodynamic screening and incompressibility. *Physical Review Letters*, 99(12):124502, 2007.
- [100] J. L. McWhirter, H. Noguchi, and G. Gompper. Deformation and clustering of red blood cells in microcapillary flows. *Soft Matter*, 7(22):10967–10977, 2011.
- [101] S. Guido and G. Tomaiuolo. Microconfined flow behavior of red blood cells in vitro. *Comptes Rendus Physique*, 10(8):751–763, 2009.
- [102] G. Tomaiuolo, L. Lanotte, G. Ghigliotti, C. Misbah, and S. Guido. Red blood cell clustering in poiseuille microcapillary flow. *Physics of Fluids (1994-present)*, 24(5):051903, 2012.
- [103] B. Klitzman and B.R. Duling. Microvascular hematocrit and red cell flow in resting and contracting striated muscle. *American Journal of Physiology-Heart and Circulatory Physiology*, 237(4):H481–H490, 1979.
- [104] P. Gaehtgens, C. Dührssen, and K.H. Albrecht. Motion, deformation, and interaction of blood cells and plasma during flow through narrow capillary tubes. *Blood cells*, 6(4):799–817, 1979.
- [105] G.W. Schmid-Schönbein, S. Usami, R. Skalak, and S. Chien. The interaction of leukocytes and erythrocytes in capillary and postcapillary vessels. *Microvascular research*, 19(1):45–70, 1980.

- [106] J. L. McWhirter, H. Noguchi, and G. Gompper. Flow-induced clustering and alignment of vesicles and red blood cells in microcapillaries. *Proceedings of the National Academy of Sciences*, 106(15):6039–6043, 2009.
- [107] G. Ghigliotti, H. Selmi, L. El Asmi, and C. Misbah. Why and how does collective red blood cells motion occur in the blood microcirculation? *Physics of Fluids (1994-present)*, 24(10):101901, 2012.
- [108] M. Zurita-Gotor, J. Blawdziewicz, and E. Wajnryb. Swapping trajectories: a new wall-induced cross-streamline particle migration mechanism in a dilute suspension of spheres. *Journal of Fluid Mechanics*, 592:447–469, Dec 2007.
- [109] G. Cabrera, M. Cot, F. Migot-Nabias, P. G. Kremsner, P. Deloron, and A. J. Luty. The sickle cell trait is associated with enhanced immunoglobulin G antibody responses to Plasmodium falciparum variant surface antigens. *J. Infect. Dis.*, 191(10):1631–1638, May 2005.
- [110] M. J. Friedman. Erythrocytic mechanism of sickle cell resistance to malaria. *Proc. Natl. Acad. Sci. U.S.A.*, 75(4):1994–1997, Apr 1978.
- [111] D. J. Roberts and T. N. Williams. Haemoglobinopathies and resistance to malaria. *Redox Rep.*, 8(5):304–310, 2003.
- [112] T. G. Smith, K. Ayi, L. Serghides, C. D. Mcallister, and K. C. Kain. Innate immunity to malaria caused by Plasmodium falciparum. *Clin Invest Med*, 25(6):262–272, Dec 2002.
- [113] M. Murayama. Molecular mechanism of red cell "sickling". *Science*, 153(3732):145–149, Jul 1966.
- [114] M. W. Kenny, M. Meakin, D. J. Worthington, and J. Stuart. Erythrocyte deformability in sickle-cell crisis. *British Journal of Haematology*, 49(1):103–109, 1981.
- [115] J. W. Eaton, H. S. Jacob, and J. G. White. Membrane abnormalities of irreversibly sickled cells. *Semin. Hematol.*, 16(1):52–64, Jan 1979.
- [116] S. K. Ballas and E. D. Smith. Red blood cell changes during the evolution of the sickle cell painful crisis. *Blood*, 79(8):2154–2163, Apr 1992.
- [117] M. L. Gulley, D. W. Ross, C. Feo, and E. P. Orringer. The effect of cell hydration on the deformability of normal and sickle erythrocytes. *Am. J. Hematol.*, 13(4):283–291, Dec 1982.
- [118] R. N. MacCallum, E. C. Lynch, J. D. Hellums, and C. P. Alfrey. Fragility of abnormal erythrocytes evaluated by response to shear stress. *J. Lab. Clin. Med.*, 85(1):67–74, Jan 1975.

- [119] W. H. Crosby. The metabolism of hemoglobin and bile pigment in hemolytic disease. *Am. J. Med.*, 18(1):112–122, Jan 1955.
- [120] P.R. McCurdy, L. Mahmood, and A.S. Sherman. Red cell life span in sickle cell-hemoglobin c disease with a note about sickle cell-hemoglobin o arab. *Blood*, 45(2):273–279, 1975.
- [121] S. Chien, S. Usami, and J. F. Bertles. Abnormal rheology of oxygenated blood in sickle cell anemia. *J. Clin. Invest.*, 49(4):623–634, Apr 1970.
- [122] D. K. Kaul, D. Chen, and J. Zhan. Adhesion of sickle cells to vascular endothelium is critically dependent on changes in density and shape of the cells. *Blood*, 83(10):3006–3017, May 1994.
- [123] N. Mohandas and E. Evans. Sickle erythrocyte adherence to vascular endothelium. Morphologic correlates and the requirement for divalent cations and collagen-binding plasma proteins. *J. Clin. Invest.*, 76(4):1605–1612, Oct 1985.
- [124] G. A. Barabino, L. V. McIntire, S. G. Eskin, D. A. Sears, and M. Udden. Endothelial cell interactions with sickle cell, sickle trait, mechanically injured, and normal erythrocytes under controlled flow. *Blood*, 70(1):152–157, Jul 1987.
- [125] Y. Lamarre, M. Romana, X. Waltz, M. L. Lalanne-Mistrih, B. Tressieres, L. Divialle-Doumdo, M. D. Hardy-Dessources, J. Vent-Schmidt, M. Petras, C. Broquere, F. Maillard, V. Tarer, M. Etienne-Julan, and P. Connes. Hemorheological risk factors of acute chest syndrome and painful vaso-occlusive crisis in children with sickle cell disease. *Haematologica*, 97(11):1641–1647, Nov 2012.
- [126] R. P. Hebbel, R. Osarogiagbon, and D. Kaul. The endothelial biology of sickle cell disease: inflammation and a chronic vasculopathy. *Microcirculation*, 11(2):129–151, Mar 2004.
- [127] W. M. Lande, D. L. Andrews, M. R. Clark, N. V. Braham, D. M. Black, S. H. Embury, and W. C. Mentzer. The incidence of painful crisis in homozygous sickle cell disease: correlation with red cell deformability. *Blood*, 72(6):2056–2059, Dec 1988.
- [128] P. Connes, T. Alexy, J. Detterich, M. Romana, M. D. Hardy-Dessources, and S. K. Ballas. The role of blood rheology in sickle cell disease. *Blood Rev.*, 30(2):111–118, Mar 2016.
- [129] R. P. Rother, L. Bell, P. Hillmen, and M. T. Gladwin. The clinical sequelae of intravascular hemolysis and extracellular plasma hemoglobin: a novel mechanism of human disease. *JAMA*, 293(13):1653–1662, Apr 2005.
- [130] A. N. Schechter and M. T. Gladwin. Hemoglobin and the paracrine and endocrine functions of nitric oxide. *N. Engl. J. Med.*, 348(15):1483–1485, Apr 2003.

- [131] C. D. Reiter, X. Wang, J. E. Tanus-Santos, N. Hogg, R. O. Cannon, A. N. Schechter, and M. T. Gladwin. Cell-free hemoglobin limits nitric oxide bioavailability in sickle-cell disease. *Nat. Med.*, 8(12):1383–1389, Dec 2002.
- [132] A. I. Alayash, R. P. Patel, and R. E. Cashon. Redox reactions of hemoglobin and myoglobin: biological and toxicological implications. *Antioxid. Redox Signal.*, 3(2):313–327, Apr 2001.
- [133] V. Jeney, J. Balla, A. Yachie, Z. Varga, G. M. Vercellotti, J. W. Eaton, and G. Balla. Pro-oxidant and cytotoxic effects of circulating heme. *Blood*, 100(3):879–887, Aug 2002.
- [134] D. K. Kaul, M. E. Fabry, and R. L. Nagel. Erythrocytic and vascular factors influencing the microcirculatory behavior of blood in sickle cell anemia. *Ann. N. Y. Acad. Sci.*, 565:316–326, 1989.
- [135] D. K. Kaul, M. E. Fabry, and R. L. Nagel. Microvascular sites and characteristics of sickle cell adhesion to vascular endothelium in shear flow conditions: pathophysiological implications. *Proc. Natl. Acad. Sci. U.S.A.*, 86(9):3356–3360, May 1989.
- [136] D. K. Kaul and R. P. Hebbel. Hypoxia/reoxygenation causes inflammatory response in transgenic sickle mice but not in normal mice. *J. Clin. Invest.*, 106(3):411–420, Aug 2000.
- [137] E. Ponder et al. Hemolysis and related phenomena. 1971.
- [138] P.K. Wallace, J.D. Tario, J.L. Fisher, S.S. Wallace, M.S. Ernstoff, and K.A. Muirhead. Tracking antigen-driven responses by flow cytometry: Monitoring proliferation by dye dilution. *Cytometry Part A*, 73A(11):1019–1034, 2008.
- [139] K.A. Muirhead, J. D. Tario Jr, and P.K. Wallace. Cell tracking with lipophilic membrane dyes: Applications in cancer research.
- [140] J.D. Tario Jr, K. Humphrey, A.D. Bantly, K.A. Muirhead, J.S. Moore, and P.K. Wallace. Optimized staining and proliferation modeling methods for cell division monitoring using cell tracking dyes. *Journal of visualized experiments: JoVE*, (70):e4287–e4287, 2011.
- [141] W. Thielicke and E.J. Stamhuis. PIVlab – Towards User-friendly, Affordable and Accurate Digital Particle Image Velocimetry in MATLAB. *Journal of Open Research Software*, (2), 2014.
- [142] K. Lee, M. Kinnunen, M.D. Khokhlova, E.V. Lyubin, A.V. Priezhev, I. Meglinski, and A.A. Fedyanin. Optical tweezers study of red blood cell aggregation and disaggregation in plasma and protein solutions. *Journal of Biomedical Optics*, 21(3):035001, 2016.

- [143] M. Rampling and John A. Sirs. The interactions of fibrinogen and dextrans with erythrocytes. *The Journal of physiology*, 223(1):199, 1972.
- [144] H. Bruus. *Theoretical Microfluidics*. Oxford Master Series in Physics. OUP Oxford, 2008.
- [145] S. Chien and K.-M. Jan. Red cell aggregation by macromolecules: Roles of surface adsorption and electrostatic repulsion. *Journal of Supramolecular Structure*, 1(4-5):385–409, 1973.
- [146] S. Kim, R. L. Kong, A. S. Popel, M. Intaglietta, and P. C. Johnson. Temporal and spatial variations of cell-free layer width in arterioles. *Am. J. Physiol. Heart Circ. Physiol.*, 293(3):H1526–1535, Sep 2007.
- [147] J. D. Corbett, W. E. Mickols, and M. F. Maestre. Effect of hemoglobin concentration on nucleation and polymer formation in sickle red blood cells. *J. Biol. Chem.*, 270(6):2708–2715, Feb 1995.
- [148] W. Reinke, P. C. Johnson, and P. Gaehtgens. Effect of shear rate variation on apparent viscosity of human blood in tubes of 29 to 94 microns diameter. *Circ. Res.*, 59(2):124–132, Aug 1986.
- [149] N. Maeda, Y. Suzuki, J. Tanaka, and N. Tateishi. Erythrocyte flow and elasticity of microvessels evaluated by marginal cell-free layer and flow resistance. *American Journal of Physiology - Heart and Circulatory Physiology*, 271(6):H2454–H2461, 1996.
- [150] J. C. Liao, T. W. Hein, M. W. Vaughn, K. T. Huang, and L. Kuo. Intravascular flow decreases erythrocyte consumption of nitric oxide. *Proc. Natl. Acad. Sci. U.S.A.*, 96(15):8757–8761, Jul 1999.